Gesellschaft für Anlagen-
und Reaktorsicherheit
(GRS) mbH

Two-Phase-Flow Experiment in the Fractured Rock of the HRL Äspö

GRS - 183

Gesellschaft für Anlagen-
und Reaktorsicherheit
(GRS) mbH

Two-Phase-Flow Experiment in the Fractured Rock of the HRL Äspö

Herbert Kull
Peter Bastian
Rainer Helmig
Hartmut Jakobs
Norbert Jockwer
Klaus-Peter Kröhn
Jörg Mönig
Volker Reichenberger
Ulrich Zimmer

Dezember 2002

GRS - 183
ISBN 3-931995-51-8

Deskriptoren:

Endlagerung, felsformation, Gasbildung, Gasmigration, Geoelektrik, Granit, Langzeitsicherheit, Modellierung, Zweiphasenfluss

Preface

Gas is expected to be generated in repositories for LLW and ILW wastes by anaerobic corrosion of canisters, radiolysis, and microbial degradation of organic substances. For that reason overpressures could be built up in disposal rooms and affect the integrity of geotechnical barriers. To assess the importance of this scenario in repositories in granite formations two-phase-flow models are needed which enable numerical simulation of gas migration through water-saturated fractures.

In 1995, the Swedish Nuclear Fuel and Waste Management Company (SKB) and the German Federal Ministry of Education, Science, Research and Technology (BMBF) therefore signed a co-operation agreement in view of the performance of a German Two-Phase-Flow Experiment the Äspö Hard Rock Laboratory (HRL) in Sweden. The project involved field investigations and theoretical studies in order to provide the needed calibrated models. The project was performed by GRS[1] and BGR[2], while PTE[3] co-ordinated the co-operation with SKB.

This report describes the work performed by GRS and its subcontractor CAB[4] in the years 1997 through 1999.

A summary report of the German Two-Phase-Flow-Experiment including the work of BGR as well as of GRS is in preparation and will be published as SKB report.

[1] Gesellschaft für Anlagen- und Reaktorsicherheit mbH, Köln
[2] Bundesanstalt für Geowissenschaften und Rohstoffe, Hannover
[3] Projektträger des BMWi und BMBF für Entsorgung, Karlsruhe
[4] Institut für Computeranwendungen im Bauwesen, Technical University of Braunschweig

Acknowledgements

The authors would like to thank the Svensk Kärnbränslehantering AB (**SKB**) especially Olle Olsson representing the colleagues of the Äspölaboratoriet for the co-operation and the auxiliary experimental support. All project partners thanks for fruitful scientific discussions, especially thanks to Gia Destouni and Jerker Jarsjö from the Division of Water Resources Engineering (**WRE**), Kungliga Tekniska Högskolan, Stockholm. Werner Bechthold from the Forschungszentrum Karlsruhe, Abteilung Projektträgerschaft Entsorgung (**PTE**) is thanked for co-ordinating the activities of the German Two-Phase-Flow project and for his continuous efforts towards a better communication on the issue of gas migration through fractured rock. The authors are also very grateful to the funding German governmental departments, the 'Bundesministerium für Wirtschaft und Technologie' (**BMWi**) and the Bundesministerium für Bildung und Forschung (**BMBF**).

Table of Contents

1 Introduction

In 1995, the Swedish Nuclear Fuel and Waste Management Company (SKB) and the German Federal Ministry of Education, Science, Research and Technology (BMBF) signed a co-operation agreement which allows German research institutions to perform field experiments at the Äspö Hard Rock Laboratory in Sweden.

Within the framework of this agreement BMBF, BGR and GRS agreed to perform a Two-Phase-Flow Project (TPF-project) consisting of field investigations and theoretical studies in order to develop improved and calibrated models for the assessment of gas and associated radionuclide migration in repositories for radioactive wastes in saturated highly fractured granite formations.

1.1 Rationale Scope and Objectives

Significant amounts of gas may be expected in repositories for radioactive waste. The gases as for instance hydrogen, methane, and carbon dioxide are produced by anaerobic corrosion of canisters and by microbial degradation of organic matters in low- (LLW) and intermediate- (ILW) level radioactive waste. In addition, radiolytic decomposition of fluids can lead to gas generation due to the γ-radiation of high- level waste (HLW). The gas generation may lead to an undesired pressurisation of disposal rooms and thus to the migration of the gas and leached radionuclides from the repository into the biosphere.

In case of water saturated crystalline host rocks two-phase-flow of water and gas might govern the migration processes. Special attention is to be directed towards fractured areas in the rock mass and the EDZ around underground disposal rooms. In order to assess the migration processes in long-term safety analyses, adequate models and computer codes are necessary.

In preceding years, at the GRIMSEL Test Site (GTS), considerable work had been performed to increase the understanding of the potential impact of two-phase-flow processes on the performance of underground waste repositories and to provide a basis for modelling these processes. The work comprised theoretical and laboratory experiments and in-situ investigations /MAR 99/. On the same subject SKB and the

Royal Institute of Technology, Stockholm (KTH) investigated the phenomenon of ‘degassing effects’ of natural gas which is dissolved in the formation water /GEL 95/.

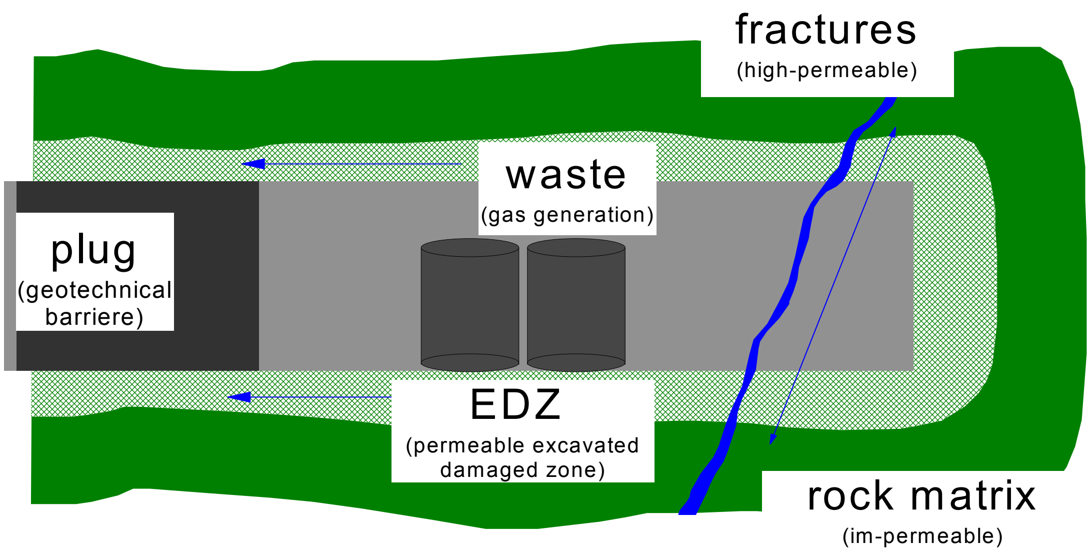

Figure 1.1-1: Sealed disposal room in a fractured rock formation

The main objective of the GRS programme was focussed on the two-phase-flow experiment and the determination of the natural gas concentration and composition in the granitic rock. Beyond this, the applicability of geoelectric monitoring for determining local and regional changes of water saturation in the host rock were tested. Detailed objectives of the two-phase-flow experiment were:

- hydro geological characterisation of the niche 2715 to generate a data base for the set up of a conceptual two-phase-flow model,
- single-phase flow and two-phase-flow modelling to determine initial conditions in the test area in the saturated granite rock.

At the beginning of the project, numerical modelling of non-isothermal, two-phase / two-component processes was feasible only for a two-dimensional representation of a porous medium.

To overcome this restriction, the code MUFTE_UG was to be developed to model three-dimensional fractured and porous media. Hence, a further objective of the project was:

- development of the theoretical basis and the mathematical algorithm of the MUFTE_UG-code including advanced discretisation techniques for modelling two-phase/two-component flow of water and gas in a three-dimensional fractured porous media.

1.2 Project Execution

GRS and BGR were partners for the performance of the TPF-project, while PTE co-ordinated reporting and co-operation with SKB. The principle modelling of GRS was supported by advanced theoretical investigations of CAB. The section Geochemistry and Mineralogy of the Technical University of Clausthal was involved in the petrologic investigations.

The field investigations were performed in the niche 2715 at the 360 m-level which was selected within a pre-investigation programme performed by GRS in 1996 /FLA 97/.

In 1997, the niche 2715 was prepared for measurements of the pressure distribution in the near-field of the niche /JOC 98/. Since 1998, the basic flow parameters were determined by hydro testing. Measurements of two-phase-flow parameters, especially the gas threshold pressure, started in 1999. At the same time, a new technique of gas sampling was applied to determine the natural composition of dissolved gas in the formation water.

In 1999, patterns of packers for a dipole test configuration were installed by BGR in 1999 to perform gas tracer tests. GRS accompanied the BGR measurements with numerical calculations.

The codes ROCKFLOW /KOL 97/ and MUFTE /HEL 94/ were used by GRS to assess initial field conditions by single-phase- and two-phase-flow-simulations and to interpret observed in-situ flow conditions. The results of the site characterisation were used to set up the numerical simulations (see section 2.2).

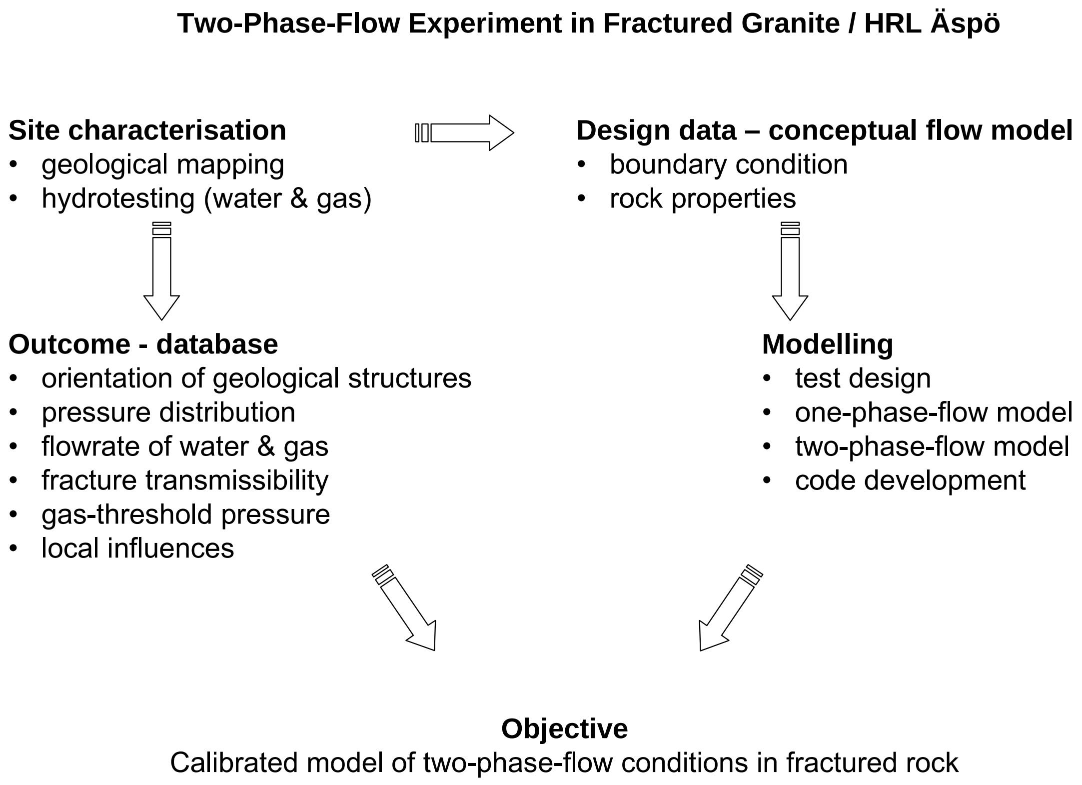

Figure 1.2-1: Overview of the Two-Phase-Flow Project

The single-phase-flow model (ROCKFLOW) was developed to analyse the pressure and flow development in a fracture system on regional scale after opening the niche and to set up the outer boundary conditions for the 3-D-model. This 3-D-model was also used to estimate the hydraulic parameters of the inner boundary of the 2-D two-phase-flow model (MUFTE) to simulate a gas injection test in a fracture on local scale. Similar to the dipole test of the BGR, the development of a gas plume between two borehole intervals was studied with this model.

The methodology of geoelectric in-situ measurements was applied to the pylon in the ZEDEX area to determine the water saturation and water-bearing master faults. The change of the apparent resistivity with time was monitored and set into relation to real resistivity by data re-processing. In 2D-models the long-term development of water distribution was correlated with geological structures. In section 3 the different test sequences and modelling results are described.

2 Two-Phase-Flow Investigations

The two-phase-flow investigations involved field investigations on the hydraulic in-situ conditions in the underground test niche necessary for model calibrations as well as modelling activities to investigate the long-term importance of two-phase-flow in fractured porous media.

2.1 Field Investigations

Herbert Kull

The following experimental steps had to be performed after site preparation:

- Hydro-geological characterisation of the experimental site, including aspects of the lithology,
- determination of the distribution of hydraulic pressure and of effective flow parameter,
- selection of a dipole configuration and measurement of transport parameter values (e.g., effective porosity and tracer velocities) in the dipole flow field (BGR),
- determination of the natural gas composition in the formation water.

2.1.1 Water Conducting Features and Lithology of the Test Site

The niche 2715 at the 360-m-level was suggested as the most suitable and representative one for the granitic host rock at the Äspö HRL /RHE 97a/, /RHE. 98/, /FEI 98/. During test site preparation, the highly damaged front face of the niche was removed by means of smooth blasting.

On macroscopic scale (local scale), water-conducting features being more than 5 m wide and extending several hundred meters intersect the isle of Äspö (e.g. NE2 in Figure 2.1-1).

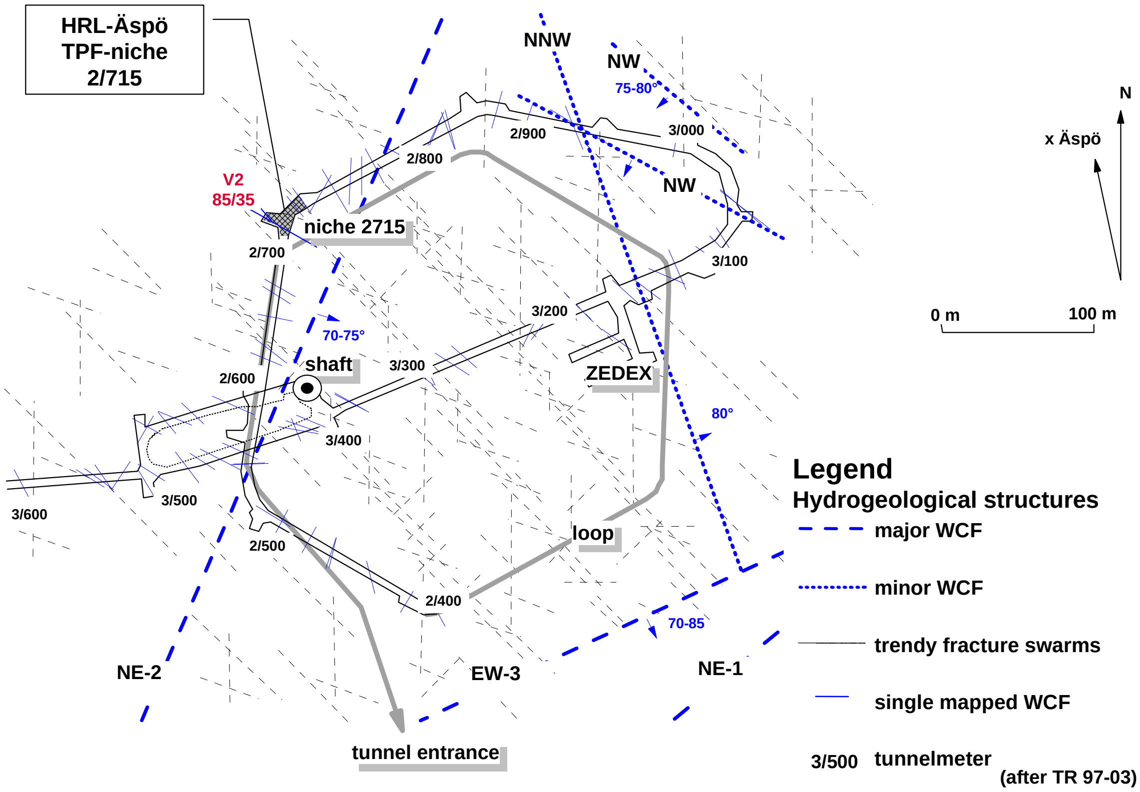

Figure 2.1-1: Local structures at the Äspö Site (after RHE, 1997a)

According to their dominating orientation, these features are named NE or EW and NNW or NW. These major fault zones have subvertical dips and can be followed more than 500 m in depth. Mainly the brittle NE-features are of high transmissivity and low mechanical strength while the reactivated ductile EW-features are of good mechanical strength for construction purposes. None of these major features mapped from the topography and during tunnel excavation are observed to intersect the flow field at tunnel meter 2715 in distances up to 50 m. The NE-2 structure is expected to be the nearest major fault zone east of the niche.

The selected subvertical WNW-ESE orientated fracture system crossing the niche is classified as a water conducting feature of type 2 (Figure 2.1-2) consisting of master faults intersected by steps and slays cracks.

The range of transmissivities (10^{-8} to 10^{-3} m^2 s^{-1}) yielded from borehole tests for the tunnel section 700 to 2875 m shows the high variability of hydraulic conductivity of these major fault zones. There are some indications that the transmissivity decrease with depth.

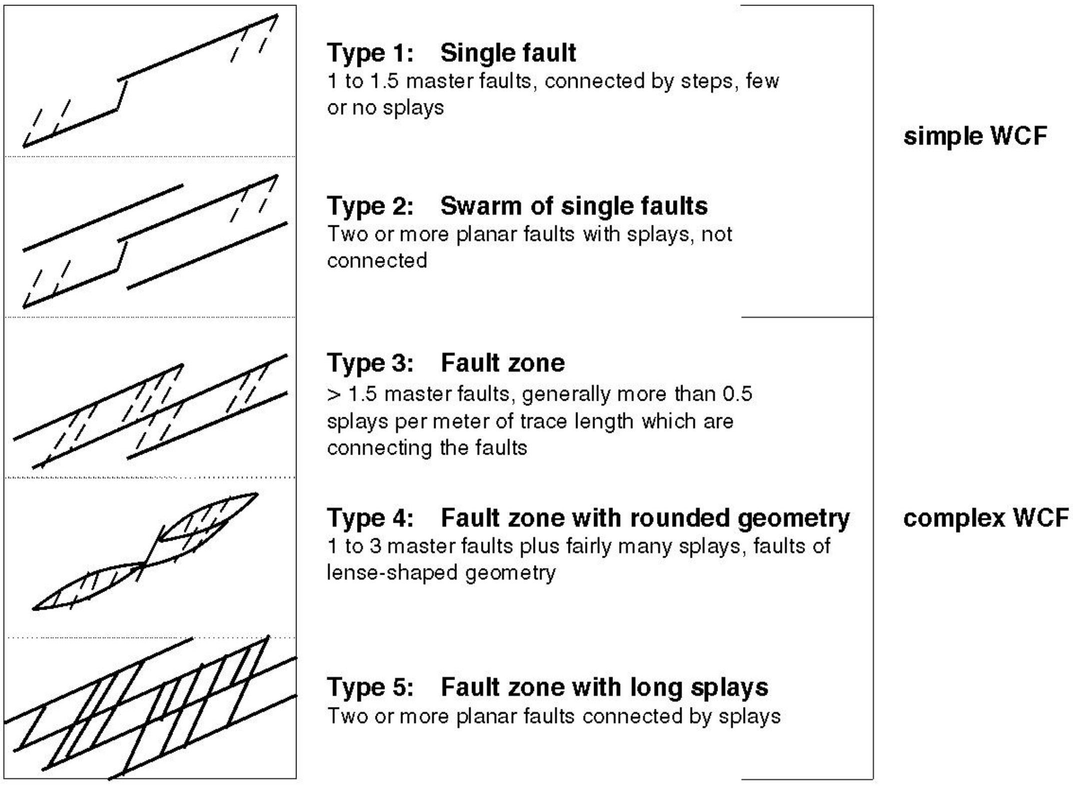

Figure 2.1-2: Classification of water-conducting features (WCF) at Äspö (after BOS, 1998)

Minor fault zones (> 5 m – 0.1 m) and single water-bearing fractures (0.1 m – 0.001 m) have to be distinguished from major faults by short fracture length and spacing, but not in their statistical distribution of orientation. In the vicinity of the test niche 2715, most of the fractures are orientated NW and NNW and frequently discharge into the tunnel.

The geological structures in the niche were mapped in the frame of the site characterisation activities (Figure 2.1-3). Apart from secondary artificial fractures caused by the excavation a subvertical fracture system was mapped as mainly opened structures crossing the niche 2715. This sublocal fracture system in the niche consists of subvertical WNW- ESE water-bearing fractures intersecting horizontal calcite-filled closed fractures. Drill cores were logged with respect to the orientation and connections between significant fractures. Depending on scale, the named V2-fracture system was determined to be the major water-bearing feature influencing the flow-field in that area (Figure 2.1-4).

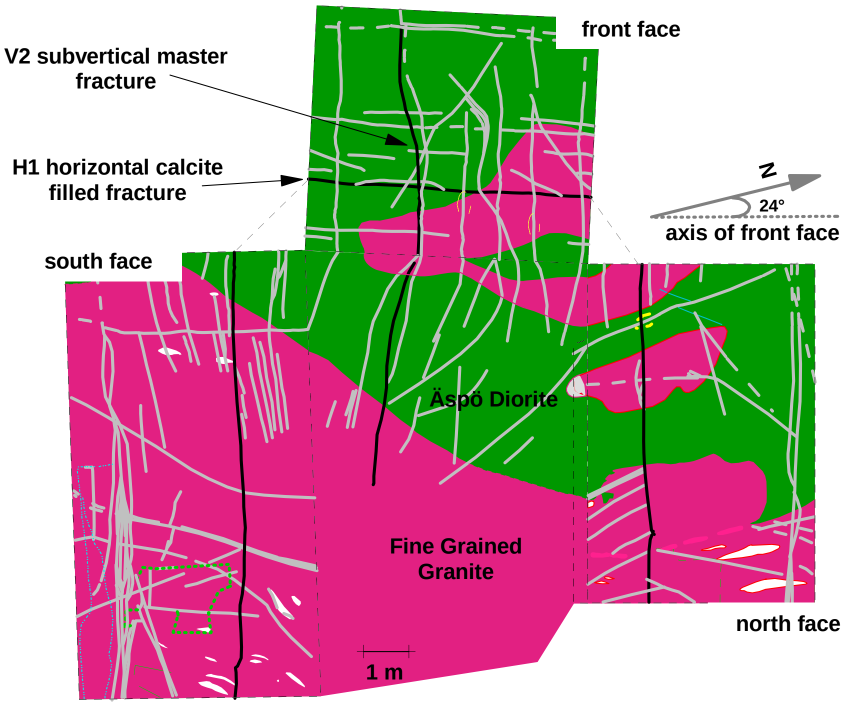

Figure 2.1-3: Geology and major structures on the sublocal scale of the niche 2715

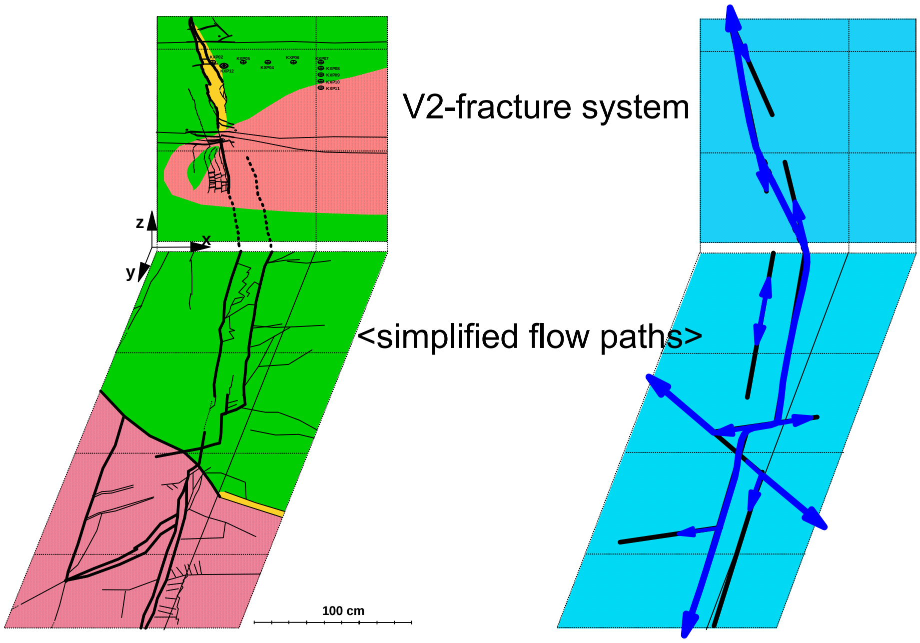

Figure 2.1-4: The subvertical V2-fracture in nature (left) and simplified (right)

The local types of rock consist of Äspö diorite, fine-grained granite, Småland granite and greenstone – as the last two types of rock are not observed in the direct vicinity of the test niche. The lithological composition is almost representative for the local rock mass. From mineralogical investigations of rock material /SEL 00/, the solid phase is consisting of plagioclas, feldspar and quartz as major components and minor components of muscovite, chlorite and calcite.

In detail, the Äspö diorite is a dark-grey to red-grey, medium-grained granodiorite with red potash feldspar inclusions. The potash feldspars have a length of approx. 0.5 – 1.0 cm. However, crystals up to 4 cm have been observed. The diorite has been dated to around 1.803 billion years, and is thus of similar age to the Småland granite. The fine-grained granite is a brittle, red to light red-grey granite with a large proportion of quartz and potash feldspar. Unlike the Småland granite, its composition reflects the habit of a granite. The fine-grained granite mostly occurs in veins in the Äspö diorite or the Småland granite. However, veins also cut the fine-grained granite. It has been dated to 1.794 billion years. The Äspö diorite is graded into the fine-grained granite. The typical chlorite banding of the fine-grained granite is clearly shown.

The Småland granite or Ävrö granite is medium-grained, porphyritic and has a composition varying between granodiorite and quartz monzonite. The potash feldspars are irregularly distributed. The Ävrö granite partially cuts through the Äspö diorite and therefore appears to be of younger age - although from dating this rock type is of almost the same age as the Äspö diorite. The greenstone is fine-grained as well as medium to coarse-grained (diorite or gabbro). They differ from the granitoids by their grey to dark-grey colour. They occur as small intrusions and are often penetrated by aplite granite veins.

2.1.2 Hydraulic Testing

The hydraulic pressure measurements as well as the water and the gas-injection tests were performed up to 5 m in distance to the front face in horizontal boreholes (Figure 2.1-5). Additionally, the formation-water pressure was measured in four vertical boreholes which were used also for gas sampling (see section 2.1.3). From previous data it was not expected that other experiments, performed in the vicinity in the rock laboratory, would influence these hydraulic investigations.

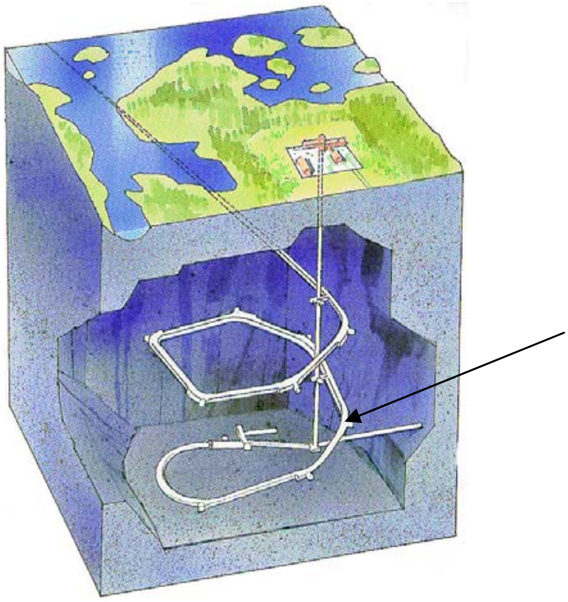

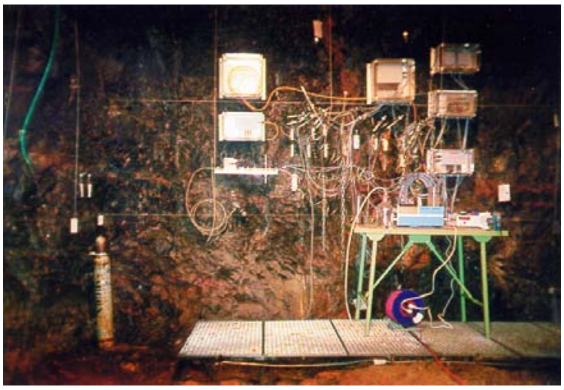

Figure 2.1-5: (left) Location of the test niche at tunnel meter 2715. (right) View on the front face of the niche prepared and instrumented

2.1.2.1 Test Equipment and Configuration

Within the scope of site preparation, a 2-m-deep highly damaged zone was removed by means of smooth blasting. In April 1997, fourteen boreholes, 32 mm in diameter and up to 3.44 m long, with an inclination of 10 to 40° were drilled into the prepared front face (Figure 2.1-6). Four of these boreholes (KXP04, KXP05, KXP06, and KXP07) intersect the main water-bearing V2-fracture system. The boreholes KXP08 and KXP09 were found to be connected just by splays with the V2-fracture. Further drillings (KXP10, KXP11, KXP13, KXP15, KXP16, KXP17, KXP18 and KXP19) stroke no water bearing fissures and represent the homogeneous rock matrix. In September 1997, for down-hole pressure measurements, the bottom of each borehole was equipped with a mechanical stainless-steel packer system.

Four additional boreholes with a diameter of 84 mm, crossing the main fracture plane in 3 and 5 m-distance to the front face (KXP23, KXP24, KXP25, and KXP26), were completed in July 1998 by BGR. These boreholes were used to examine the hydraulic regime to a larger extent and for dipole-tests including gas injection tests.

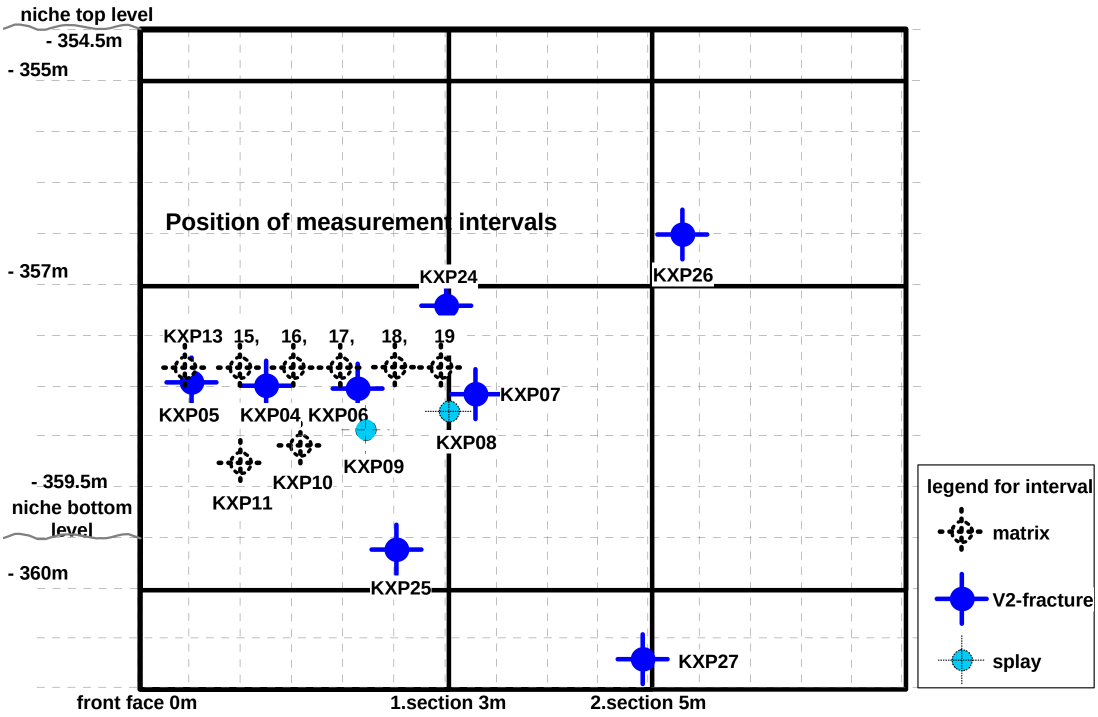

Figure 2.1-6: Position of borehole intervals in a vertical section beyond the front face

The niche itself is at least approximately 8 m wide. At the back, it extends into the rock with an area of about 4.5 by 6 m. The entrance to the niche was closed by a brick wall to minimise disturbances to the pressure experiments from the access tunnel. For security, a wire net was installed at the roof of the niche with steel anchors.

All water pressure data were transmitted to the data acquisition system (GEOMONITOR station). All pressure and hydrotest data measured in niche 2715 were stored as ASCII and BIN files on an underground located PC. After quality control, pressure versus time data were converted into LOTUS 123 or EXCEL files. A modem connection was used to transfer the data directly to GRS in Braunschweig.

The lengths of measurement intervals were between 0.05 – 0.80 m. The pressure in each interval was measured by a pressure transducer outside the borehole (connected by 1/4" stainless-steel tubes and SWAGELOK connections to the packer interval). To avoid uncontrolled flow of water and leakage of the packer system during the long-term measurements, the section between the packer and the front face was filled with synthetic resin SIKADUR 52 (Figure 2.1-7).

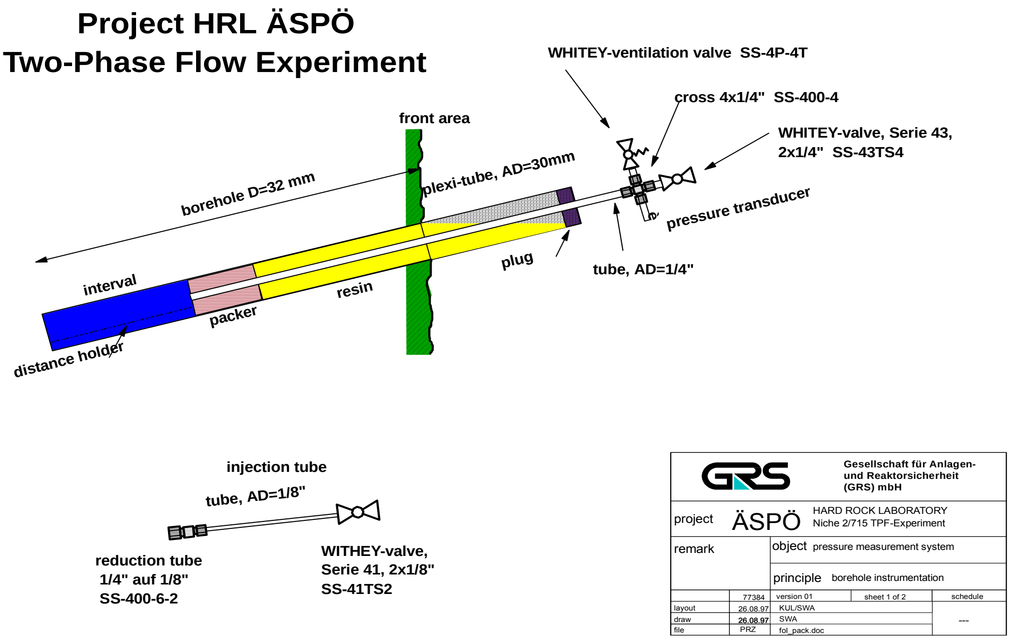

Figure 2.1-7: Typical test equipment in a borehole

2.1.2.2 Hydraulic Pressure Monitoring

The initial pressure distribution is determined from long-term pressure measurements in the fractures and the rock matrix. Considering the overburden and previous SKB pressure measurements, a maximum pressure of 3.5 MPa was expected. The monitoring data over two years, however, indicate a steady state pressure lower than the expected one.

The monitored water pressure in the rock matrix indicates a pressure level below the atmospheric one. In a distance from 0.5 to 3 m the level did not increase, even after re-saturation. In Figure 2.1-8 the pressure curve of the interval KXP10, which is 1.2 m behind the front face, is generally below the measured absolute air pressure of 114 kPa.

The low stagnant pressure in the rock matrix might point out the influence of gas in the tight matrix.

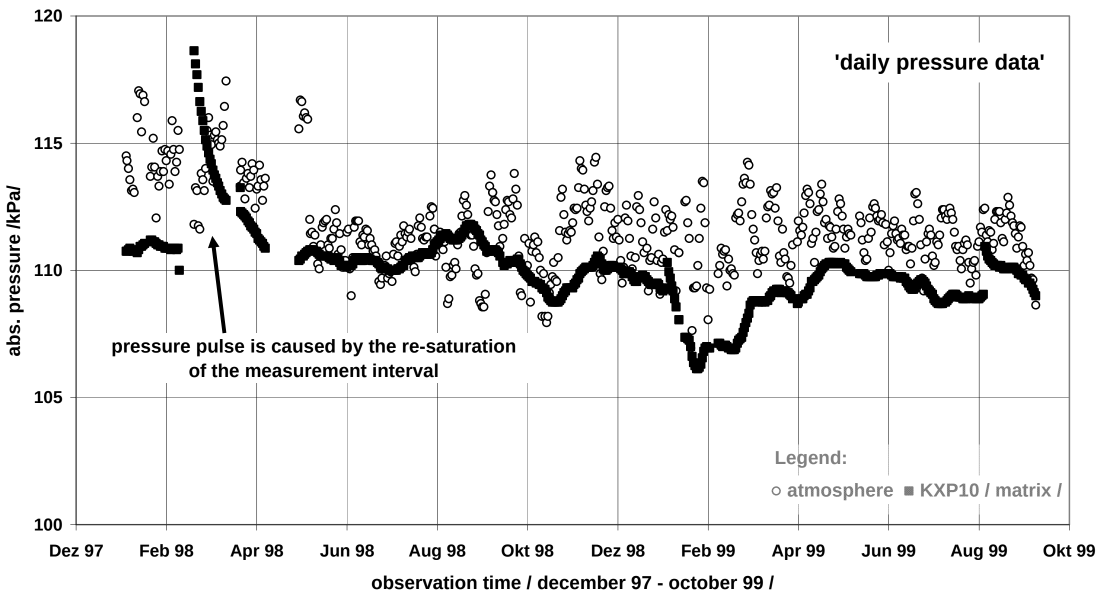

Figure 2.1-8: Test interval KXP10GRS: Example for the development of the water pressure in the rock matrix

The gas phase might have evolved due to the drilling of the boreholes and a subsequent pressure drop around the interval leading to degassing. Because this would lead to a significant decrease of the intrinsic permeability to water the natural re-saturation would take more time than the observation time was.

The presence of a compressible gas phase in the matrix is necessary to explain the difference to the much higher pressure in the nearby fracture and the absence of responses from pressure pulses of 2000 kPa set in the fracture.

These observed effects lead to the assumption of an unsaturated zone which influences the water flow in the rock matrix significantly.

The development of the hydraulic pressure, measured during two years, indicate a steady state flow-field in the V2-fracture. Short-term pressure variations and interim pressure increases were caused by drilling activities (July 1998) and series of hydrotests, gas threshold pressure measurements (GTHP) and gas injection tests (see Figure 2.1-9).

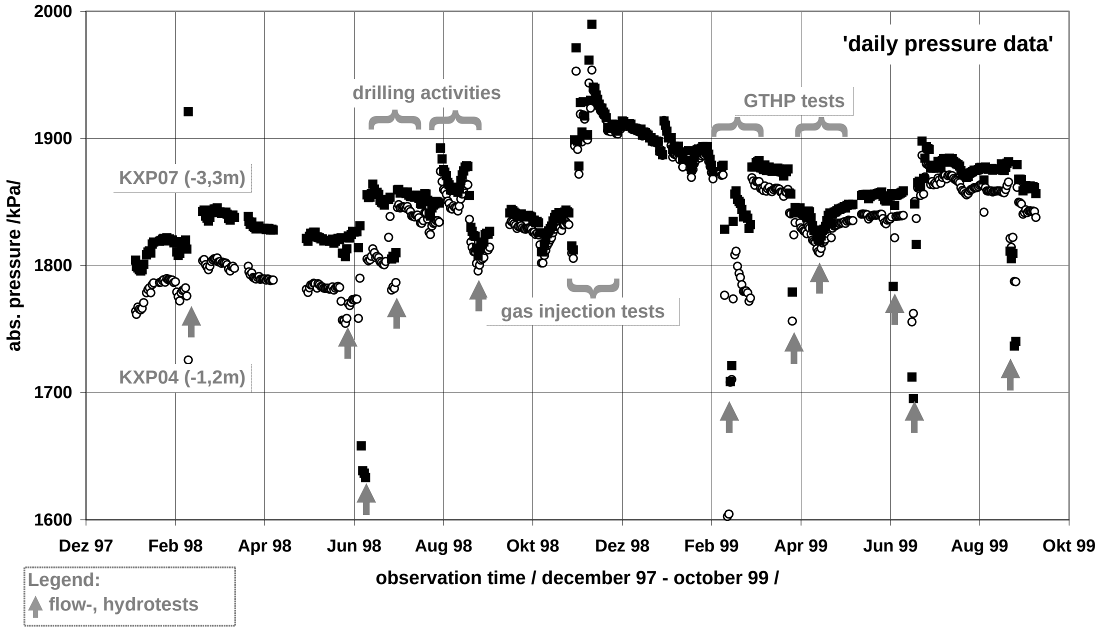

Figure 2.1-9: Test interval KXP04GRS and KXP07GRS: Example for the long-term development of the water pressure in the V2-fracture

The almost unchanged pressure level in the observations intervals gives evidence that the pressure distribution behind the front face had already become stationary before the experiment was started. The observed pressure recovery, after test activities support the conclusion of steady state flow conditions around the niche.

In Figure 2.1-10 the fluid pressure measured after active testing (flow tests and fluid sampling in KXP04 to KXP07) in May 1999 are shown. The pressure recovery in all intervals is of the same type and follows simultaneously each opening of the test interval. This is interpreted as a non restricted communication and a concurrent laminar water flow within the fracture.

Directly behind the front face of the niche (0.6 m) the pressure development showed a different behaviour. The pressure responses did not show the same behaviour as measured in the deeper intervals (see curve of borehole KXP05 EDZ). Also the lowered pressure level of about 0.5 MPa deviates significantly from those measured in the other intervals.

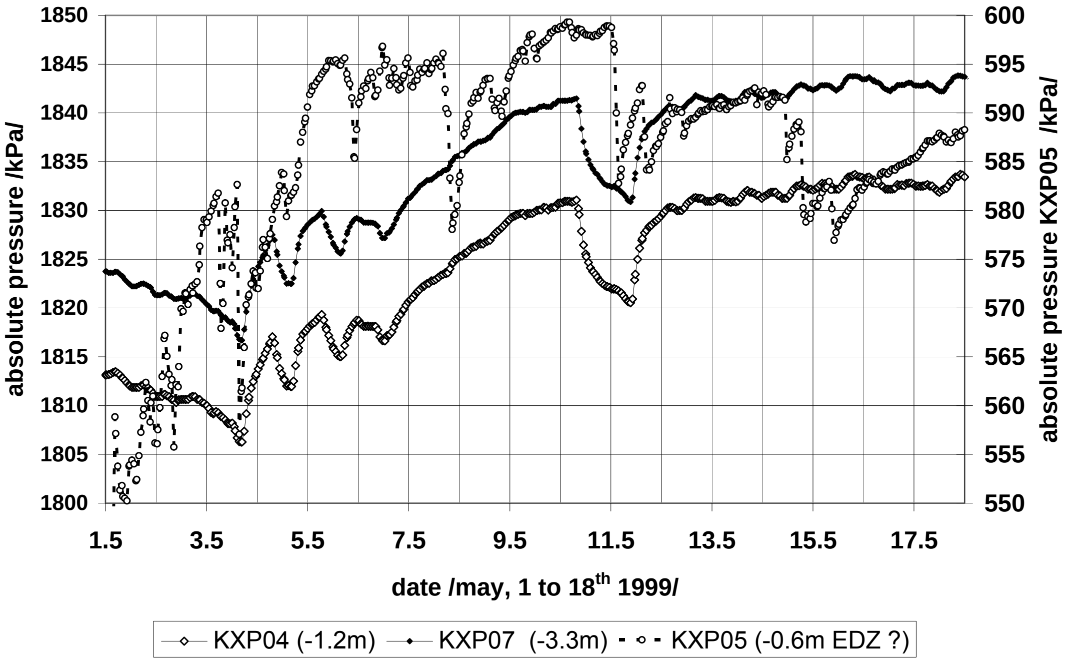

Figure 2.1-10: Pressure development and pressure responses after hydraulic testing of the V2-fracture

The absence of clear pressure responses might be caused either by the interruption of the hydraulic communication system (damaged fracture system) and the separation of this part of the fracture or by the influence of evolved gas (unsaturated disturbed zone). Close to the front face of the niche the pressure is steeply increasing. Beyond the excavation disturbed zone, the pressure is more moderately increasing by 140 kPa per meter (see Figure 2.1-11).

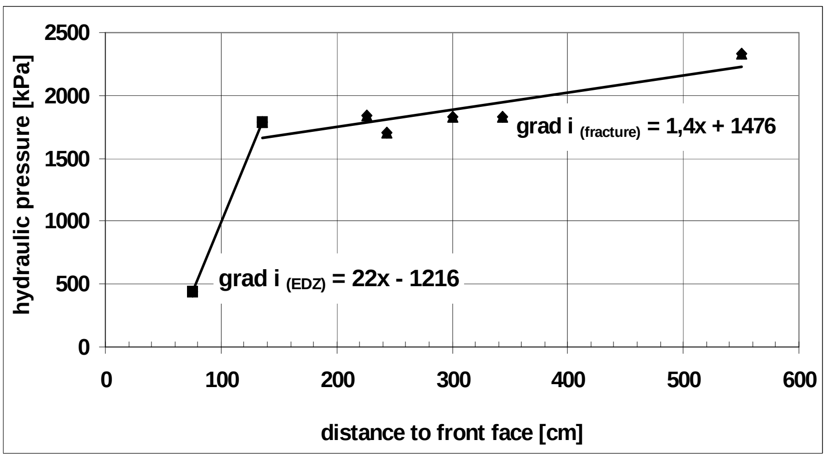

Figure 2.1-11: Initial pressure distribution and hydraulic gradient in the V2-fracture

Within the EDZ, the pressure in the V2-fracture decreases significantly towards the front face. According to later modelling (see section 2.2.3) this behaviour can only be explained by a smaller permeability of the rock located close to the front face.

2.1.2.3 Transmissivity of the V2-Fracture

The transmissivity was estimated from hydraulic tests which were evaluated assuming validity of Darcy's law in this complex network of fissures. For empirical calculations laminar viscous flow conditions within the V2-fracture were assumed and the test area was considered to be homogeneous and isotropic. The rock matrix was expected to act as impermeable boundaries. In the case of an opened interval radial water flow was assumed (see Figure 2.1-12).

Provided that these assumptions are valid and that the fracture acts as a confined aquifer, the transmissivity in the test area was calculated as follows /after THI 06/:

$$T = \frac{q \cdot \rho \cdot g}{2 \cdot \pi} \cdot \ln \frac{R}{r_1} \cdot \frac{1}{p_2 - p_1} \qquad \text{eq. 2.1-1}$$

where

T	=	transmissivity of the permeable zone	$m^2\ s^{-1}$
q	=	flow rate	$m^3\ s^{-1}$
R	=	radius of the opened test interval	m
r_1	=	distance to the observation interval	m
p_1	=	fluid pressure /Pa/ in the test interval	$kg\ s^{-2}\ m^{-1}$
p_2	=	fluid pressure /Pa/ in the observation interval	$kg\ s^{-2}\ m^{-1}$
ρ	=	the density of the fluid	$kg\ m^3$
g	=	gravitational acceleration	$m\ s^{-2}$.

The transmissivities within the V2-fractures were calculated from flow tests performed in all measurement intervals. The distances between the intervals vary from 0.75 to 2.7 m. The test configuration and required geometric parameters for the calculation of the transmissivities are given in Figure 2.1-12.

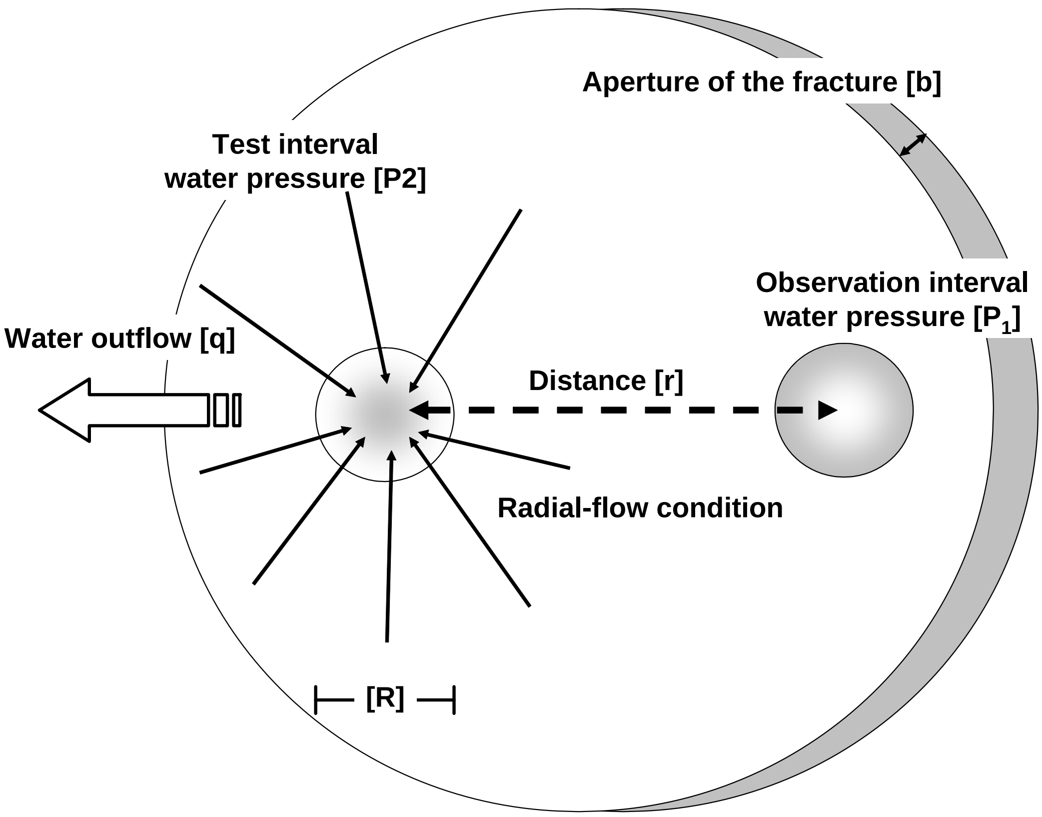

Figure 2.1-12: Scheme of the configuration of flow tests in boreholes which intersect the V2-fracture

In Table 2.1-1 the transmissivities between the test intervals are listed. The values are in the range from 10^{-9} to 10^{-6} $m^2\ s^{-1}$. The lowest values determined for the EDZ interval KXP05 correspond with the transmissivities calculated for the surrounding of KXP06 which is located 2.2 m behind the front face. The transmissivities are varying depending on the flow direction.

Table 2.1-1: Transmissivities within the V2-fracture

	KXP05	KXP04	KXP06	KXP07
Water out flow:	Transmissivity [$m^2\ s^{-1}$]			
KXP04	6,0E-06		3,0E-07	3,5E-07
KXP05		4,5E-09	5,5E-09	6,1E-09
KXP06	2,8E-08	6,6E-09		6,8E-09
KXP07	1,7E-06	2,6E-07	3,0E-07	

The relatively wide range of the values determined for the hydraulic V2-structure leads to the statements that

- the natural variation of transmissivities in the single fault systems vary by orders of magnitudes,
- favoured flow paths are obviously within the fracture,
- anisotropy of the effective aperture of the fracture influences the water flow.

With respect to the apparent aperture of the fracture the variation of transmissivities can also be influenced by heterogeneity within the fracture. In approximation to the "cubic law" /WIT, 06/ taken to describe the transmissivity of the fracture between two plates and the hydraulic conductivity K, the effective aperture can be calculated:

$$T = \frac{\rho \cdot g \cdot b^3}{12 \cdot \mu} \qquad \text{after 'Cubic Law'} \qquad \text{eq. 2.1-2}$$

$$b = \sqrt[3]{\frac{12 \cdot T \cdot \mu}{\rho \cdot g}} \qquad \text{eq. 2.1-3}$$

$$K = \frac{\rho \cdot g \cdot b^2}{12 \cdot \mu} \qquad \text{eq. 2.1-4}$$

K	=	hydraulic conductivity	m s^{-1}
b	=	aperture of the fracture	m
μ	=	viscosity	kg s^{-1} m^{-1}.

From the transmissivity values (Table 2.1-1) apparent apertures b, were derived. They range between 0.00002 m and 0.0005 m and the corresponding hydraulic conductivities K, range between 10^{-4} and 10^{-6} m s^{-1}.

Complementary numerical calculations were performed to estimate the permeability, k of an equivalent porous fracture zone. Following the assumptions of homogeneous and isotropic flow conditions the simulations were applied on the pressure recovery tests using the WELTEST 200 simulator /WEL 97/.

Figure 2.1-13 shows as an example a reasonable fit of measured and calculated data for the flow and pressure recovery period in borehole KXP07. The evaluation of the flow period and the following pressure recovery revealed the permeability of the equivalent V2-fracture to be in the range of 10^{-2}-Darcy corresponding to a permeability of approximately of $k = 10^{-14}$ m². The estimated extension of the fracture was calculated to be larger than 30 m from the test area.

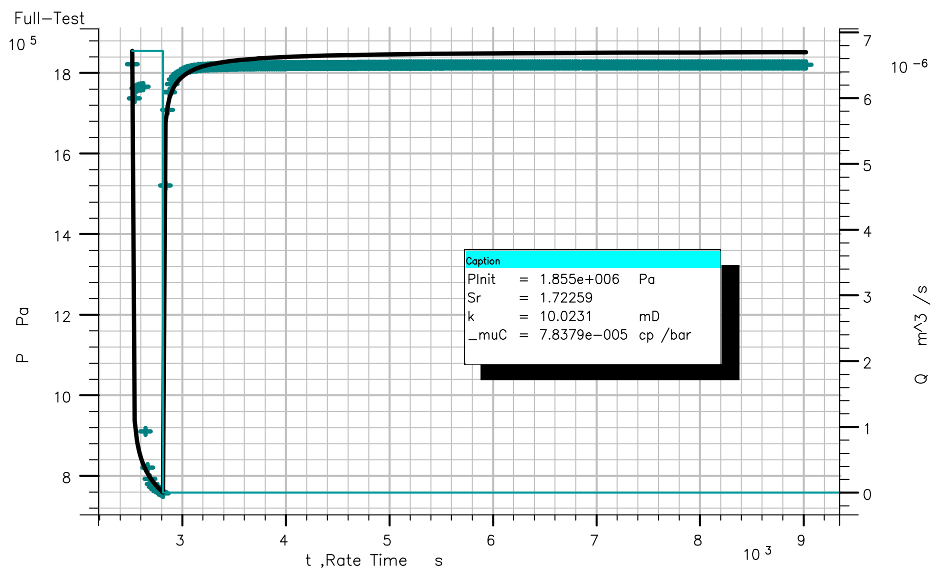

Figure 2.1-13: Simulation of a flow test in borehole KXP07 in the V2-fracture. Calculated pressure data (black line) with a homogenous fracture flow model fit with measured data (grey cross)

2.1.2.4 Gas Threshold Pressure Measurements

The determination of the **G**as **Th**reshold **P**ressure (GTHP or entry pressure) was part of the site characterisation programme of the project in order to determine the entry pressure and to assess gas mobility in fractured and homogeneous tight areas of the rock mass.

The GTHP is expected to be one of the relevant parameters controlling gas and water flow in fractured crystalline rock. By definition the GTHP describes the pressure which is necessary to replace the wetting phase (e. g. water) by the non-wetting phase (e. g. gas) in fully water-saturated pore volumes. Due to the surface tension and the size of pore spaces GTHP can be orders of magnitudes higher than the hydraulic water pressure.

In case of small pores and high capillary forces initiation of gas flow through the non-fractured matrix needs very high gas entry pressures. Fractures with an aperture (width) in the range of millimetres, on the contrary, have a very low GTHP.

Figure 2.1-14 shows the principle steps of a gas injection test. Within the compliance phase, the injection tube-system is filled with gas (nitrogen or argon) and checked for gas leakage while the water filled interval is stabilised to the initial hydraulic pressure. In the following phase (adjustment phase) the gas pressure is adjusted to the initial water pressure.

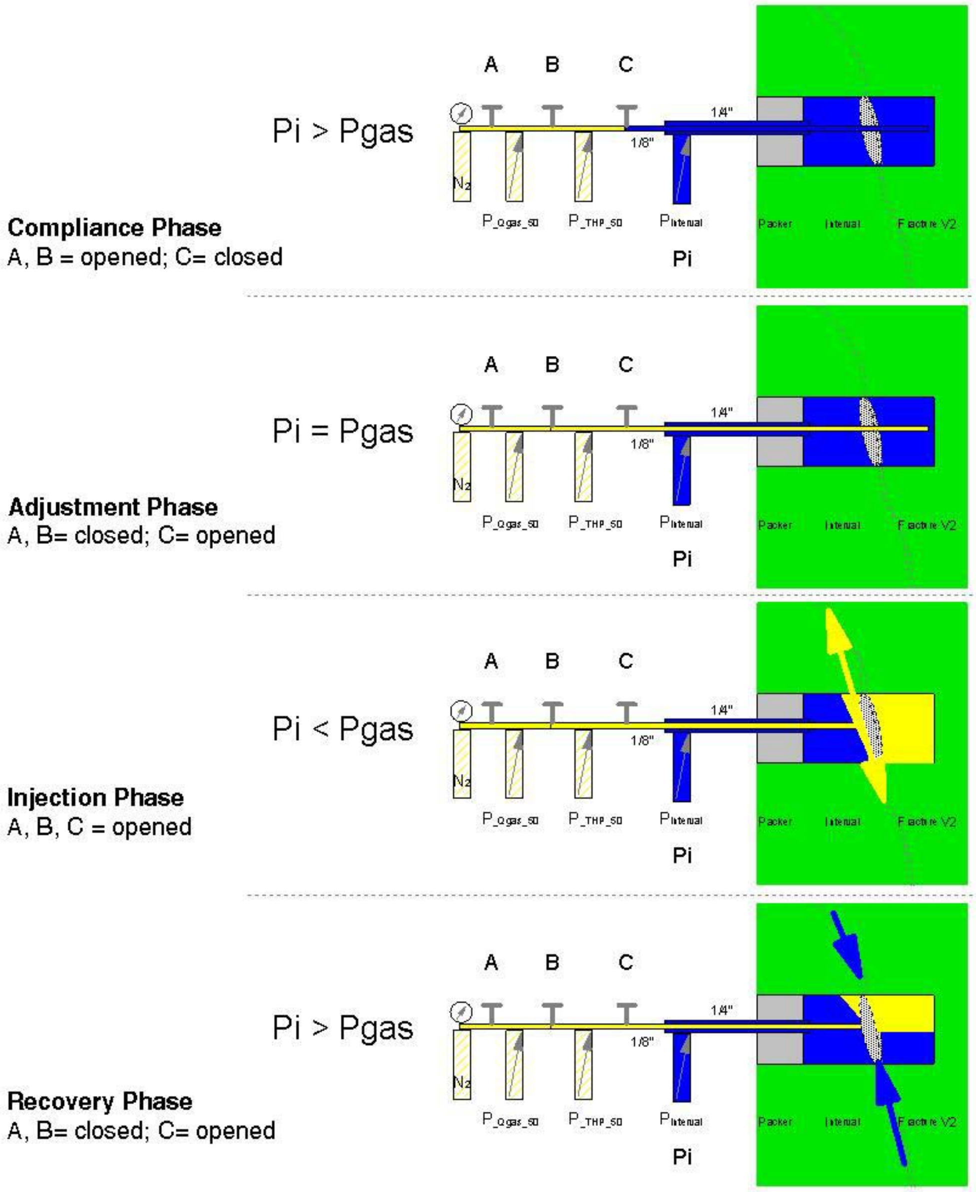

Figure 2.1-14: Scheme of gas threshold pressure tests

When pressure equilibrium is reached, the injection system is connected to the interval and single pulses and/or flow periods of gas follow until the interval is shut-in (injection phase). From the period that follows (recovery phase), the GTHP and the general gas flow condition are derived.

Figure 2.1-15 shows the results of a typical gas threshold pressure measurement in the test interval KXP07 with an initial hydraulic pressure of 1851 kPa. In all the testing steps the applied pressure collapsed more or less instantaneously thereby indicating that there are no restrictions for the gas entry into the water-bearing V2 fracture.

In matrix intervals gas was injected with pressures up to 5.0 MPa which was the upper limit of the test equipment. The very low decrease of pressure after shut-in reveals that the GTHP must be much higher than 5 MPa.

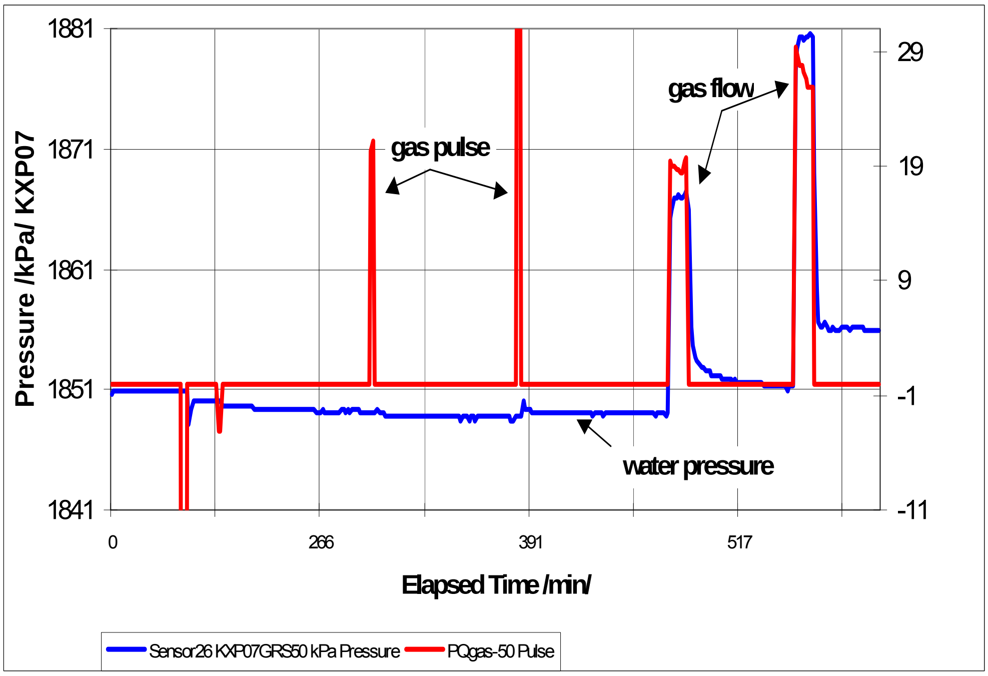

Figure 2.1-15: Results of gas injection in the V2-fracture

2.1.3 Investigation of Natural Gas Release

Norbert Jockwer & Jörg Mönig

The granite of HRL ÄSPÖ and its formation water contain gases that are adsorbed to the crystal boundaries or are dissolved in the aqueous phase. The natural equilibrium is disturbed and gases are released upon mining galleries, drilling boreholes, or heating the host rock as a result of the disposal of high level waste.

For developing a long term safety concept of disposing radioactive waste the gases in the host rock are of importance as they may:

- enforce the corrosion of the container material
- interact with the solidification matrix or the disposed waste
- be the transport medium for released radionuclides

For a qualitative and quantitative determination of the gases adsorbed to the granite or dissolved in the formation water and the extent of gas release, different samples were taken:

- water and gas samples from sealed boreholes
- solid samples from recently mined or drilled granite.

Within this project the gas content of the formation water and its equilibrium with the gas phase were determined at the in-situ conditions of the unheated stage. In the laboratory, first investigations on formation water and granite samples at elevated temperature were performed.

2.1.3.1 Experimental concept

In niche 2715 m near to the wall, four vertical boreholes (KXP 20, KXP 21, KXP 22, and KXP 23) were drilled into the floor with a diameter of 101 mm and depths of 9.56 m, 7.80 m, 5.33 m, and 2.50 m (see Figure 2.1-16).

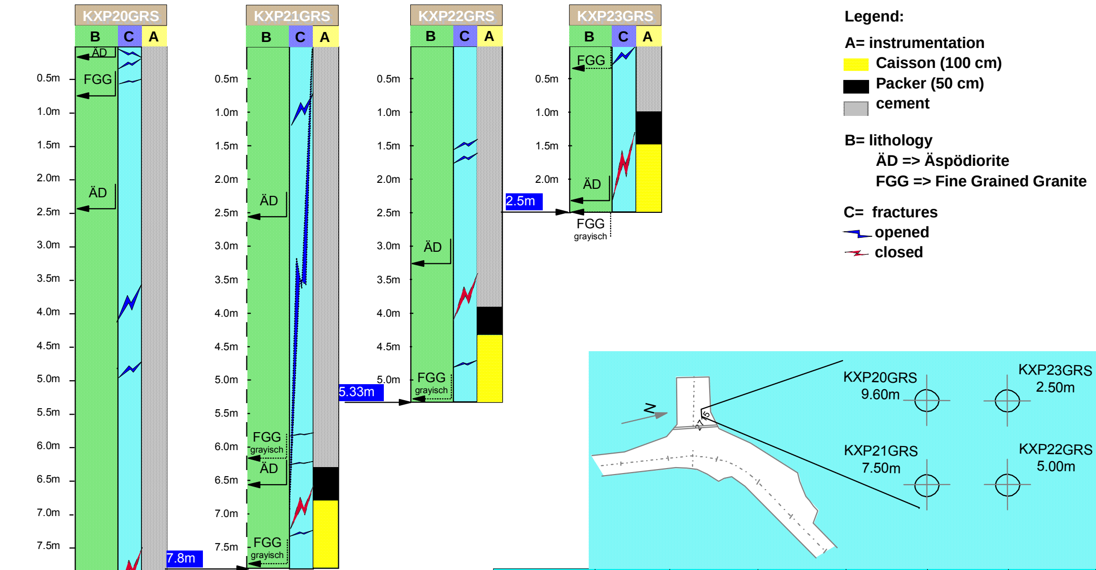

KOD	LENGTH	X	Y	Z	DECLIN /°/	INCLIN / °/
KXP20GRS	0 m	7415.169	2077.765	359.873	360	-89.8
	9.56 m	7415.131	2077.765	-369.433		
KXP21GRS	0 m	7416.096	2078.243	-359.925	265.2	-88.6
	7.8 m	7416.08	2078.056	-367.723		
KXP22GRS	0 m	7415.6556	2079.117	-359.892	349.7	-88.7
	5.33 m	7415.773	2079.095	-365.221		
KXP23GRS	0 m	7414.758	2078.635	-359.923	260.5	-89.3
	2.5 m	7414.753	2078.605	-362.423		

Figure 2.1-16: Location of the gas sampling boreholes KXP20, KXP21, KXP22, and KXP23 with the installed packers and the geological situation

In order to allow water and gas sampling these boreholes were sealed with special packers which consist of a stainless steel body of 95 mm diameter with an inflatable rubber jacket and a stainless steel pipe (caisson pipe) of 85 mm diameter which is welded to the body of the packer. The total length is about 1.30 m.

The packers were installed at the bottom of the boreholes and inflated up to 10 bars with water by a manual pump. In order to ensure that the inflated packers remain at the installed location even if the sealed area of the borehole is pressurised up to 4 MPa (40 bar formation pressure of the water) they were fixed additionally. Right after installation, the water in the residual borehole above the packer was pumped off and the boreholes were backfilled with concrete up to the floor of the gallery. This concrete transfers the load of the packer generated by the pressurised borehole to the host rock via the super surface.

Water and gas was sampled from the sealed area of the borehole via three steel capillaries (sampling tubes), which led from the gallery level through the concrete backfill and the packer into the caisson steel pipe welded to the packer body. These sampling capillaries with an outer diameter of 6 mm and an inner diameter of 4 mm were ending at the top, mid and bottom level of the caissons pipe, respectively. In the gallery, the capillaries were connected to a valve panel that was equipped with pressure gauges, sampling valves and pressure registration units.

Figure 2.1-17 shows the principal drawing of the packer system installed in the boreholes with the capillaries and the valve panel while Figure 2.1-16 shows the location of the boreholes KXP 20, KXP 21, KXP 22, and KXP 23 in the floor of the niche with the installed packers and the geological situation of the host rock.

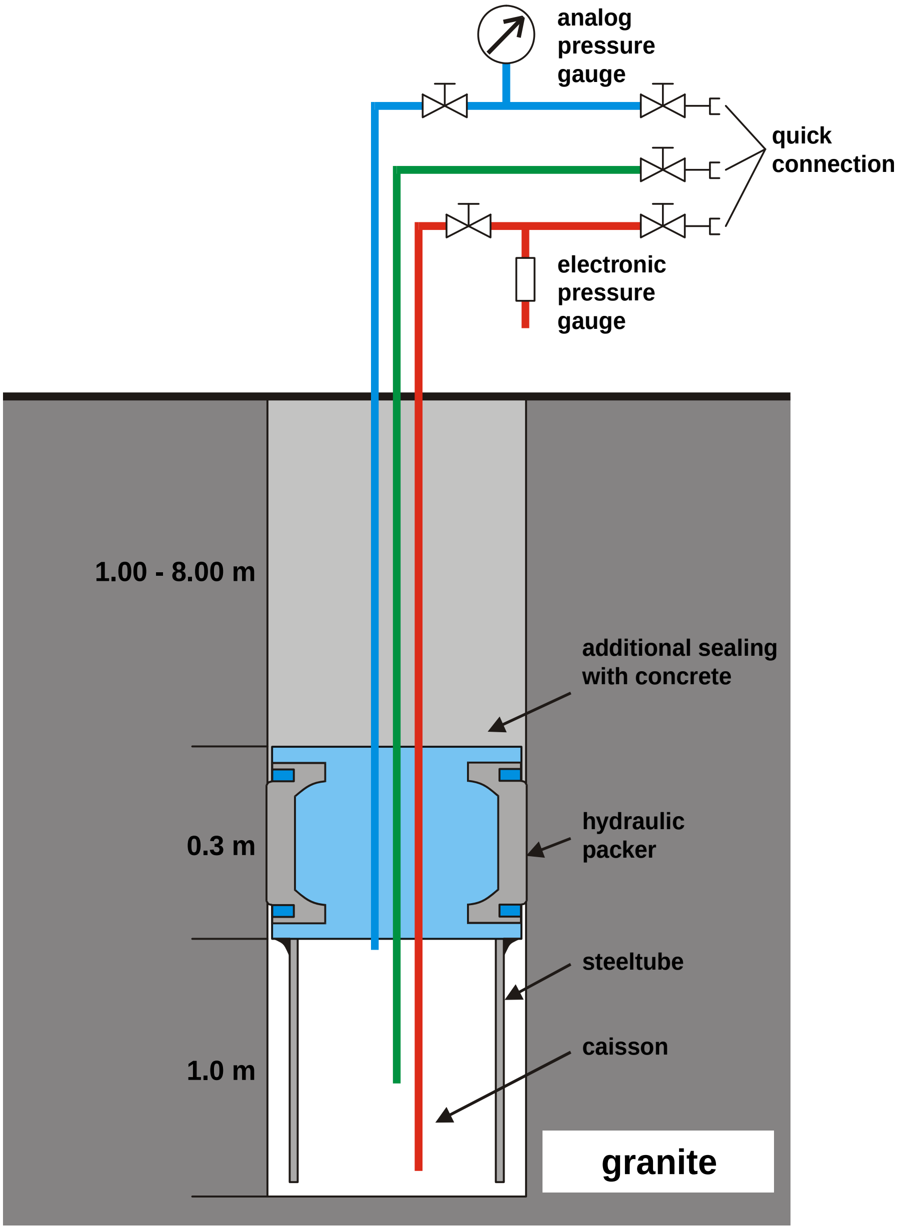

Figure 2.1-17: Principal drawing of the packer system installed in the borehole with the capillaries and the valve panel

The boreholes were drilled April 1997. The packers were installed July 1997. In September 1997 the capillaries were sealed and the boreholes became pressurised by the inflow of formation water. In February 1998, the boreholes were inflated with argon via the top capillary while the mid capillary was opened to reduce the water in the caisson to the mid level. Afterwards all valves were closed. As a result of that gas injection a gas buffer in the caisson was generated. Into this gas buffer gases dissolved in the formation water were released and equilibrium was established between the gas and water phase at the physical-chemical conditions of the surrounding host rock.

Gas samples were taken for analyses via the top capillary and water samples via the bottom capillary.

2.1.3.2 Horizontal Boreholes

The horizontal boreholes at the front face (see Figure 2.1-6) are completely filled with formation water and do not have a free gas phase. The formation water is pressurised in the boreholes and the temperature in the mine is about 14 °C. When the water passed through the gas separator or when they are sampled in a sample container, owing to the pressure decrease some of the dissolved gases escape the solution and form a gas phase which is trapped in the head space of the separator.

The water flow rates through the separator and the gas production rates are very different for the various boreholes. Figure 2.1-18 and Figure 2.1-19 show the data obtained on Jan. 27, 1999, for boreholes KXP 06 and KXP 07, respectively. The initial flow rates drop quickly to a steady state value which corresponds to the unrestricted flow in the pressure gradient. The initial decrease in flow rate is due to the pressure decrease within the borehole after the gas separator has been connected and the valve has been opened.

From the steady state values for water flow rate and gas production rate, in principle, one should be able to estimate the gas content of the formation water. Prerequisite is that the residence time of water in the separator is long enough for the exchange equilibrium between gas phase and solution being attained. Values of 0.030 and 0.040 ml gas per g water are obtained for KXP 06 and KXP 07, respectively. These values are about half the ‘true values’ (see next paragraph), which indicates that the partitioning between water phase and gas phase due to pressure decrease is slow and that the residence time is not sufficient when the water flow rates are high.

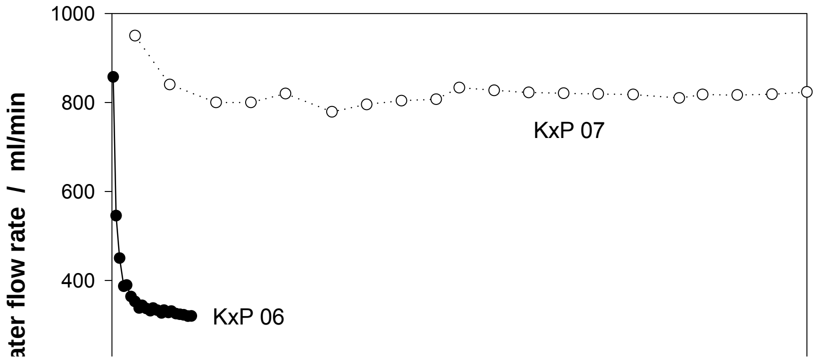

Figure 2.1-18: Gas production rate in the separator for the horizontal boreholes KXP 06 and KXP 07 on Jan. 27, 1999

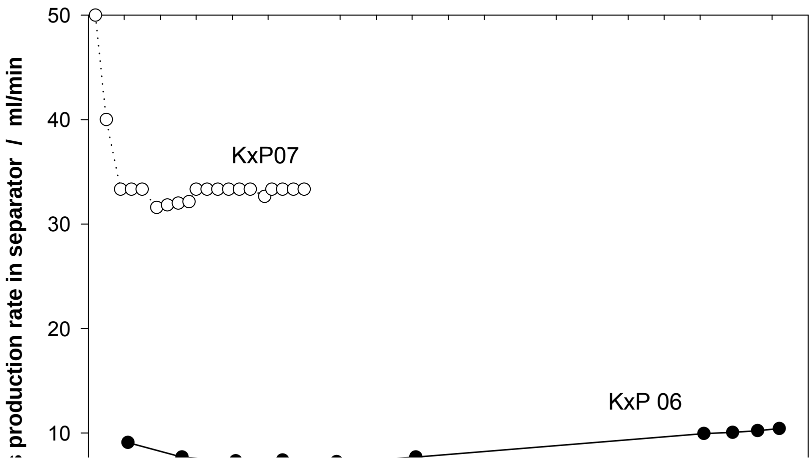

Figure 2.1-19: Gas production rate in the separator for the horizontal boreholes KXP 06 and KXP 07 on Jan. 27, 1999

The ‘true’ value’ for the gas content of the formation water was determined from samples which were directly collected into gas bags and transferred to the laboratory where they were kept at 1 bar and at room temperature for several days in order to allow equilibration. The total amount of water collected was determined by weighing the gas bags before and after filling. Owing to the pressure decrease and temperature change, some gas accumulated in the top of the bags. This gas volume was withdrawn and measured via a gas tight syringe.

The water samples taken from the gas separator were treated accordingly, thus allowing calculating the proportion of the gas release which is due to the temperature increase alone. From the difference of the two values, the proportion of the gas release that is due to the pressure decrease was determined.

Table 2.1-2 summarises the data for the total gas content of the formation water and the proportion of the gas decrease that is due to pressure decrease and temperature increase from about 14 °C to 24 °C, respectively. Data for two independent sets of experiments performed half a year apart are given.

In borehole KXP 05 there was not enough water at the second sampling period to determine the gas content. Slightly higher values have been obtained with higher water masses, presumably because it is easier to separate higher gas volumes. In general, the gas content was found to be about 9 ml gases per g of formation water.

Table 2.1-2: Total gas content of formation water collected from horizontal boreholes

				Released by:	
borehole	water mass [g]	gas volume [ml]	gas ontent [ml g^{-1}]	pressure decrease [%]	temperature increase (25°C) [%]
KXP 04	1010.80 5100	70 400	0.0693 0.0980	97.1	2.9
KXP 05	425.7 *	17 *	0.0399	*	*
KXP 06	562.0 5000	34 385	0.0605 0.0770	94.2	5.8
KXP 07	670.4 4975	46 442.5	0.0686 0.0889	88.3	11.7

* could not be determined owing to limited water mass

The gas concentrations determined in the gas samples from the separator and in the gas above the solution are very similar. Also, the concentrations in the four horizontal boreholes are comparable.

The major components are N_2, He, CH_4 and CO_2 (see Table 2.1-3), other components being only present in traces. The concentrations of the four major gas components remain fairly constant with time. In the beginning of 1999, however, especially in borehole KXP 04 the He and CH_4 concentrations dropped to a tenth of the normal steady state values and recovered slowly afterwards.

Table 2.1-3: Concentrations of major gas components dissolved in water from the horizontal boreholes

borehole	N2 [vol-%]	He [vol-%]	CH4 [vpm]	CO2 [vpm]
KXP 04	71,9	21,9	480	27
KXP 05				
KXP 06	74,2	23,0	535	28
KXP 07	75,7	21,1	494	24

Heating of the water to 100 °C under a nitrogen atmosphere releases some more gases into the head space of the sample container, mainly He and CO_2. Small hydrocarbon gases were indicated as minute traces in the chromatogram but could not reliably be determined. Upon repeated heating, only more CO_2 is released from solution.

Traces of oxygen have also been detected in all samples, in general less than 0.5 %. This oxygen is attributed to small ambient air volumes which are invariably introduced into the sample during gas sampling from the heated glass containers, most likely via the syringe needle. Therefore, the oxygen content was not further considered.

Since the formation water is neutral to slightly basic, most of the carbon dioxide in solution is hydrolysed as carbonate ions (see Table 2.1-4; some water samples were to small for complete analysis). Only a small proportion is dissolved as free carbon dioxide, which can be released into the head space via heating. The additional He released upon heating corresponds to less than 1 per cent of the other gas release due to pressure decrease and temperature increase to 25 °C.

Table 2.1-4: Chemical and physical parameters of formation water

parameter	KXP 04	KXP 06	KXP 07	KXP 22	KXP 23
sampling date	23.07.98	26.01.99	24.07.98 (27.01.99)	29.01.99	29.01.99
Cl^- [mg l^{-1}]	13190	13640	13150 (13642)	13308	13776
SO_4^{2-} [mg l^{-1}]	691,5	787	672 (682,8)	674,6	693,7
CO_3^{2-} [mg l^{-1}]		23	18		24
Na^+ [mg l^{-1}]	3498	3257	3421 (3325)	3236	3306
K^+ [mg l^{-1}]	10.63	12.57	10.41 (10.83)	73,38	11.35
Mg^{2+} [mg l^{-1}]	30.29	33.12	29.6 (32.15)	8.54	31.54
Ca^{2+} [mg l^{-1}]	4570	5190	4455 (5180)	4944	5165
pH at 25°C	7.47	6.86	7.29 (6,76)	7.84	6.71
conductivity [mS cm^{-1}]	32.7	35.6	32.2 (35.6)	34.9	35.9

2.1.3.3 Vertical Boreholes

These boreholes are equipped with a special caisson with three tubes thus allowing obtaining formation water samples from the bottom of the borehole as well as gas samples from the head space of the borehole.

After sealing the borehole in March 1998, gas samples were regularly withdrawn from the boreholes and analysed. Apart from Ar which was used to pressurise the borehole to the formation pressure, the following components were identified: He, H_2 (very rarely), O_2, N_2, CO, CH_4 and CO_2. Higher hydrocarbons and sulphur containing gases like H_2S and SO_2 were not detected. The data for He, CH_4, CO_2 and N_2 in the upper plenum of the boreholes are shown in Figure 2.1-20. The logarithmic concentration scales are different for each component but identical for a given component for all four boreholes to allow direct comparison.

Some general conclusions can be drawn from these data, even though the evolution of the gas concentrations seems to be disturbed occasionally. It is evident, that the three boreholes KXP 21, KXP 22, and KXP 23 show a similar behaviour with respect to the time course and the absolute gas concentrations, while KXP 20 is distinctly different.

This could suggest that KXP 21, KXP 22, and KXP 23 are connected through a fracture system, while KXP 20 is separated.

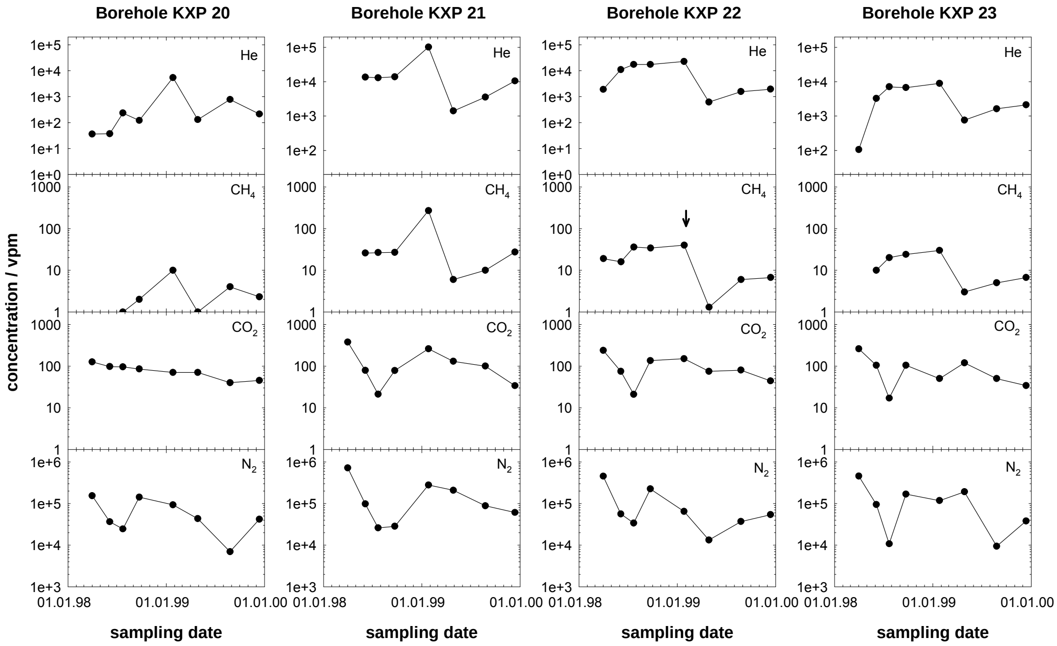

Figure 2.1-20: Gas concentrations in the head space of the four vertical boreholes

Helium and methane concentrations increase initially and strive for an equilibrium concentration, which in the case of He is around 1 % while for methane this concentration is between 10 and 30 vpm.

Carbon dioxide and nitrogen concentrations, on the other hand seem to decrease slowly with time, at last the values being about 45 vpm CO_2 and 5% N_2. This behaviour can be explained as follows. During the drilling of the boreholes ambient air has diffused into the rock matrix. Now this air equilibrates slowly with the borehole atmosphere. A prediction of the ‘true’ equilibrium concentrations is difficult on the basis of the present data. The situation is aggravated by air which may be introduced through leakages during the sampling process either into the gas samples or into the borehole. Such problems may be responsible for some of the scatter observable in the N_2 data.

Upon sampling the borehole pressure decreased but usually steady state pressures were quickly re-established. Beginning 1999, it became occasionally necessary to introduce Argon into the borehole in order to re-pressurise it. This observation points to a lowering in the flow rates of the formation water. The introduction of Ar led to a dilution of the borehole atmosphere. This is clearly evident in Figure 2.1-20 especially in the He and CH_4 concentrations. After the sampling period at the end of January all boreholes were re-pressurised with Ar, which led to a dilution by a factor of up to 10. In the present study for each sampling a volume of about 2 l had to be withdrawn in order to rinse the tubing and for gas chromatographic analyses. For future in-situ experiments we conclude that it is necessary to restrict the amount withdrawn from the system to the absolute minimum.

The formation water which has been withdrawn through the pipe ending at the bottom of the vertical boreholes have also been analysed for their gas content. While the amount of gas which was released due to pressure decrease and temperature increase to 25 °C was too little for performing gas chromatographic analyses, upon heating to 100 °C carbon dioxide and sometimes minute amounts of hydrogen and helium were detected in the gas phase. The total gas that is dissolved in formation water in the presence of a gas phase above the water is very low and corresponds to about $1\text{-}2\cdot10^{-3}$ ml g^{-1} water.

2.1.3.4 Total Gas Content of the Rock Matrix

The total gas content of the rock was determined by heating core samples at 100 °C in stainless steel containers under a nitrogen atmosphere. Three borehole cores with a weight of about 2 kg were obtained at different depths from drillings KXP 26 and KXP 27, respectively. Each day a gas sample was withdrawn from the head space of these sample containers and analysed. After the gas sample was taken, the gas phase was completely exchanged by flushing the sample container with N_2 for a short time.

The following gas components were identified in each case: He, H_2, O_2, N_2, CO, CO_2, CH_4, C_2H_6, C_2H_4, C_3H_8 and C_4H_{10}. The accumulated gas concentrations in these samples amounted always to more than 97 %. The remaining portion is attributed to water vapour. The results for rock core KXP 26 BGR 7.17 - 7.45 m are shown in Figure 2.1-21. Clearly, the major portion of the gas release occurs in the first day. For most components, the gas release drops in three days by about two orders of magnitude, so the experiments were stopped after seven days.

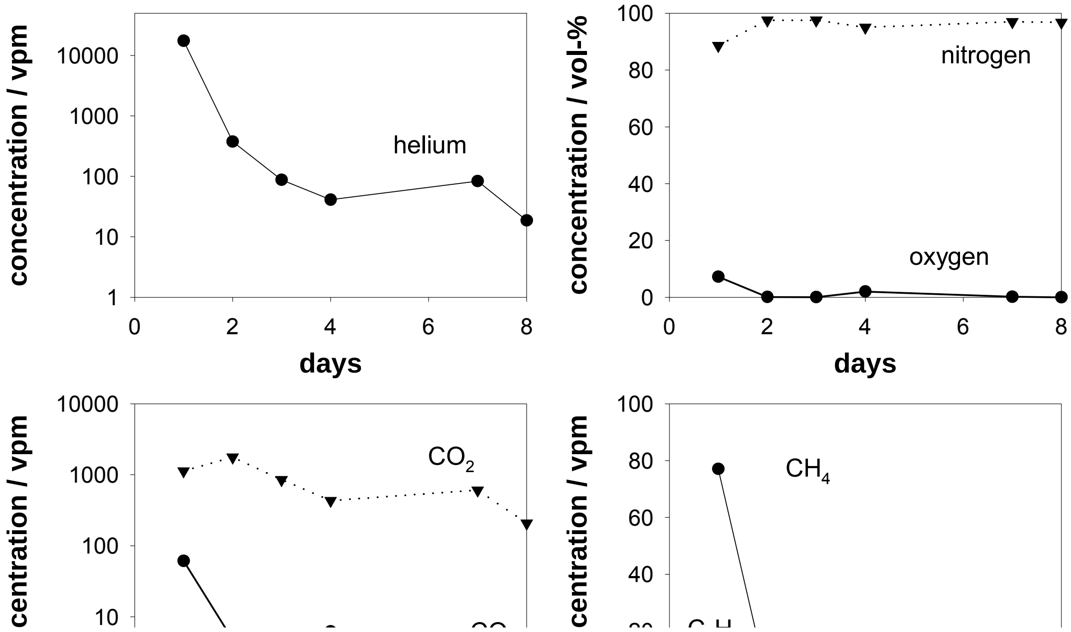

Figure 2.1-21: Thermally induced gas release from rock core KXP 26, BGR 7.17 - 7.45 m

Some C2 to C4 hydrocarbons were released from the core samples that have not been identified in the gas samples which were obtained from the borehole atmosphere directly or by degassing the water samples. These hydrocarbons are either formed via thermal cracking of some higher hydrocarbons or they are released from the rock surface due to the enhanced temperatures.

The oxygen which was released predominantly in the first day derives very likely from exposure to mine air during the drilling process and the handling of the cores before they were sealed under nitrogen in the sample container. Some oxygen may also derive from introducing minute air bubbles during handling the samples, therefore, the oxygen release is not further considered.

Interestingly, hydrogen is released from the rock samples in much higher amounts than helium, while in the gas samples obtained from the boreholes helium is abundant and hydrogen was hardly detected at all. The origin of the hydrogen is presently unknown. It could result from thermally enhanced corrosion processes occurring at the surfaces of the sample containers. However, heating experiments without rock cores but with formation water did not indicate any hydrogen formation. Another possibility is the cracking of higher hydrocarbons or catalytic processes at metal atoms within the rock core. Such processes would benefit from the enhanced temperatures during the experiment.

The helium which was found at high concentrations in the borehole gas samples or water samples is notably absent in the core samples. Helium has probably escaped during the drilling process due to its high diffusion capacity. Therefore, a direct comparison of the data obtained from in situ gas sampling and the thermally induced gas release should be done prudently.

The total gas content of the rock matrix was determined by summing up the measured gas concentrations and by relating them to the initial rock mass. The data are shown in Table 2.1-5. The distribution and the total amount of the various components is very similar in the three rock cores investigated. Apart from hydrogen, carbon dioxide is the most prominent component that is released upon heating.

Table 2.1-5: Thermally induced total gas release from rock cores. The data are given in dm^3 gas under normal conditions per 1000 kg rock

	KXP 26, BGR 7,17 - 7,45m [dm^3 1000 kg^{-1}]	KXP 26, BGR 7,45 - 7,67m [dm^3 1000 kg^{-1}]	KXP 27, BGR 6,74 - 6,94m [dm^3 1000 kg^{-1}]
He	1.288E-02	1.662E-02	7.114E-03
H2	8.315E+00	9.004E+00	2.953E+00
CO	3.668E-02	6.317E-02	5.505E-02
CO2	2.295E+00	2.910E+00	2.727E+00
CH4	3.786E-02	4.006E-02	1.540E-02
C2H6	2.623E-03	1.709E-03	8.822E-04
C3H8	5.496E-03	5.115E-03	2.165E-03
C4H10	7.634E-03	1.125E-02	7.457E-03

2.1.4 Summary and Conclusions from the Field Experiment

On macroscopic scale the flow fields in the Äspö underground research laboratory are - except for faults of extreme extension like the NE-2 – generally influenced by structures of equal orientation and with high spatial spacing as the investigated V2-fracture at the niche 2715. The fracture system V2, which is a system of main faults intersected by steps and splays, dominates the flow field in the vicinity of the niche 2715.

These structures are not real planar fractures but complex fault systems of limited extension consisting of major faults, splays and steps. From a geological point of view, for simulation purposes, it is to advice the modellers to take the natural fluctuation of the geometry and with that the hydraulic properties into account as mean statistically data with a high degree of freedom.

In this regard, statements concerning the time depending development of water and hydraulic pressure, the starting position of field data collecting seems to be of high importance. The observed pressure distribution within the fracture requires the consideration of heterogeneous permeabilities for the fracture in models.

For example, although the observed water pressure and in the same line the measured water flow rates in the V2-fracture show evidence that the flow field around the niche has become stationary, the absolute values of these parameters did not match the expected value from the overburden. A possible explanation might be found in excavation effects and the development of a disturbed zone and in some cases two-phase-flow phenomena.

Not yet fully understood is the role of the tight rock matrix with respect to the water flow. Obviously, capillary surface and tension effects rule the water exchange between matrix and fractures in a de-saturated rock area. Most probably, a gas phase which has been evolved due to a pressure drop stick in the matrix pore spaces and reduce the effective water permeability to approximately zero. It is still open to what extent this artificially effect (excavation effect) is relevant for long-term considerations.

The natural gas content of the formation water is in the range of 0.06 to 0.09 ml gas per gram water or about 60 to 90 litre gas per m^3 water. Major components are nitrogen (74%), helium (22%) - minor components are methane and carbon dioxide.

In the fracture the degassing of the formation water can affect the water permeability. This taken for granted, the heterogeneity within a fracture system alone leads to a variation of the water permeability of several orders of magnitude. One has to realise that point measurements of the permeability can be afflicted with high natural inaccuracies when using them for macroscopic considerations or further numerical calculations.

Although no restrictions for gas flow in the high permeable fracture were observed the simulation of a hypothetical dipole test (see section 2.2.3) indicate that only a characteristic saturation ratio allows the simultaneous flow of both phases (gas / water) in naturally determined pressure conditions.

The gas entry pressure in the matrix was determined to be out of detection limits (5 MPa). This entails the conclusion that gas will not migrate as a phase but rather as a solved component in the water phase through the matrix. From the experimental results and for technical reasons it can therefore be expected that with regard to the estimation of gas flow in such a fractured rock two-phase-flow phenomena are of less importance. A supporting argument is the very low gas entry pressure in fractures which is almost zero. For long-term considerations the gas phase will rather be solved as a component in the formation water than migrate as a phase through the fracture.

2.2 Numerical Simulations of One- and Two-Phase flow

Klaus-Peter Kröhn

Primary goal of the numerical simulations was to develop a two-phase-flow model of the dipole test in the V2-fracture. Since injection and extraction point were planned to be separated by several meters only, the model could be restricted to a local scale. This approach requires that the model is large enough to encompass the local pressure changes induced by the test. Additionally, the initial pressure distribution in the undisturbed flow field must be known in order to derive boundary conditions for the local scale model.

Before commencing two-phase flow modelling it was therefore necessary to establish a model for the undisturbed flow into the test niche. This model had to be of regional scale in order to make use of simple fixed boundary conditions. Under undisturbed conditions only water flow was observed. The investigations started considering single-phase flow only. The following problems were addressed during this step: characterisation of the flow domain and - at a later stage - explanation of additional data of pressure measurements.

In a second step the local scale model was constructed by extracting pressure boundary conditions from the single-phase flow model. Due to time restrictions only the injection of pure gas was simulated by means of the two-phase-flow model.

2.2.1 Homogeneous Single-Phase Flow Models

It was not clear from the beginning of the project which geological features of the flow domain would be relevant for the regional scale model. But it was known that in the niche area only one series of almost vertical and parallel orientated fractures conducted a significant amount of water, one of these fractures being the V2 structure which crosses the niche. The distance between the fractures averages about 5 metres, the integral aperture amounts to 2.5 cm.

Very little hydraulic information existed at that stage. Measurements indicated an integral outflow of three litres of water per minute out of the V2-fracture. Matrix permeability was determined in the laboratory which gave a value of about 10^{-20} m^2.

Based on these informations a simplified three-dimensional model was constructed in order to address the following problems:

- estimation of the fracture permeability
- estimation of matrix contribution to the flow
- estimation of appropriate model extension and errors at the closed boundaries
- estimation of the influence of transient effects on the regional flow field
- estimation of the influence of fracture storage capacity

Advantage was taken of several symmetries. This lead to a model with a vertical fracture and adjacent a rock matrix block (see Figure 2.2-1). Normal to the fracture plane only half of the fracture and the matrix block were considered due to symmetry reasons. Both fracture and matrix were assumed to be homogeneous with different hydraulic properties.

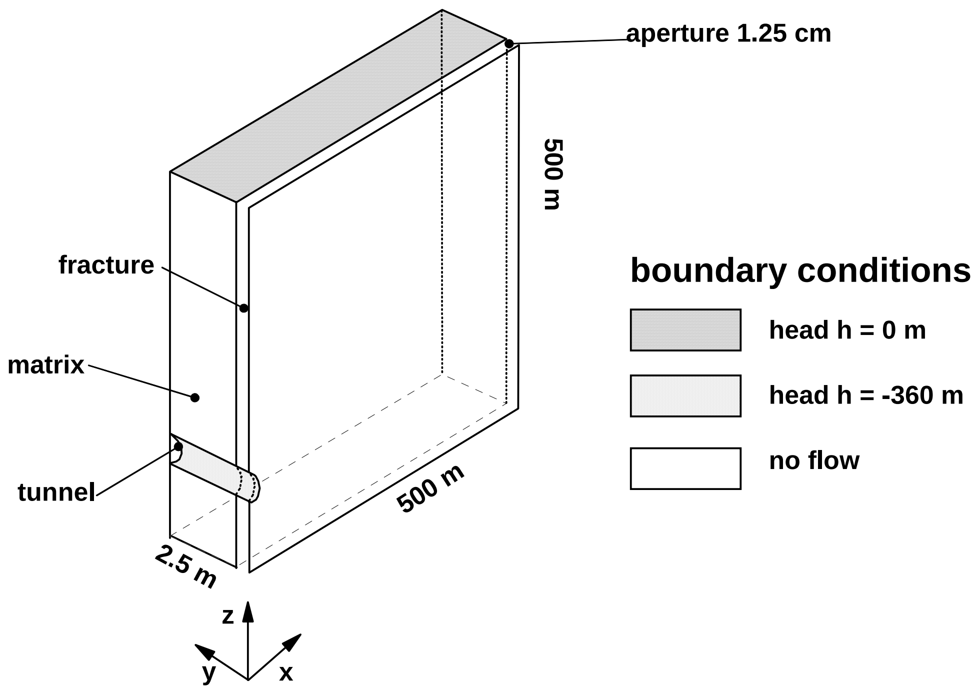

Figure 2.2-1: Geometry and boundary conditions of the 3D-Model including rock matrix and fracture

The domain size was chosen to be 500 m by 500 m with the test niche located at one of the narrow vertical sides. The niche was taken into account by a recess in the model and atmospheric pressure was assigned to this recess. The remaining vertical boundaries and the lower boundary of the system were no-flow boundaries either due to symmetric considerations or due to the assumption that inflow over these boundaries would be negligible. The top of the model was assumed to represent the bottom of the Baltic Sea, again with fixed atmospheric pressure.

For this purpose the finite element code ROCKFLOW_SM2 (version 2.22.03) (ROCKFLOW 1988-1994) was used. ROCKFLOW_SM2 calculates piezometric heads using the continuity equation for incompressible fluids in combination with Darcy's law. It allows modelling combined structures of continuous regions and discrete fractures and was therefore ideally suited to solve the problems at hand. Since hydraulic heads are easily converted into pressure data this is sometimes done in the following without saying.

The only unknown in the steady-state model was the fracture permeability. This quantity is therefore easily determined by calibrating the integral outflow. The concerning calculations yield a permeability of 10^{-12} m^2 and provided a steady-state outflow rate of 1.59 litres per minute out of the fracture. The flow rate has to be doubled because only one half of the fracture was considered in the model. An outflow of 1.59 10^{-6} litres per minute was provided by the rock matrix meaning that flow from the matrix is negligible compared to the fracture flow. Figure 2.2-2 shows the calculated hydraulic heads and Figure 2.2-3 the related pressure field. This model was taken as a base case for the following calculations.

The main contribution to the inflow on top of the model occurs naturally at minimum distance from the niche which coincides with the centre of the x-y-plane. With increasing distance from this centre the inflow rate decreases asymptotically. In order to check the assumption that most of the inflow is captured by the 500 m by 2.5 m by 500 m vertical block an enlarged domain of 2500 m by 2.5 m by 2500 m was modelled. The outflow rate is less than doubled if the inflow area is increased by a factor of 5. The pressure field in the upper left hand corner of the model compares quite well with the base case (see Figure 2.2-4). The size of the base case model is therefore large enough to avoid significant influence of the boundaries on the flow field in the vicinity of the niche.

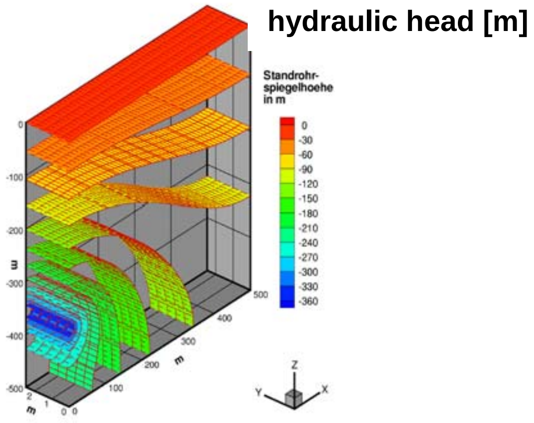

Figure 2.2-2: Base case: isoplanes of the hydraulic head at steady-state

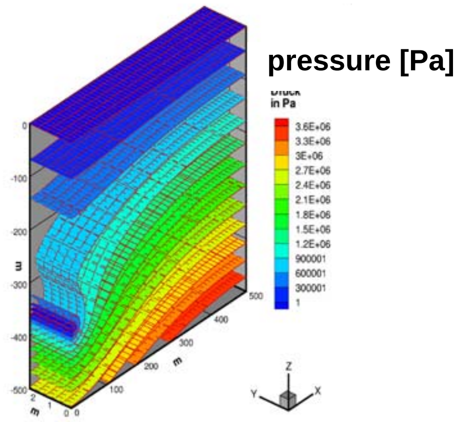

Figure 2.2-3: Base case: isoplanes of the pressure at steady-state

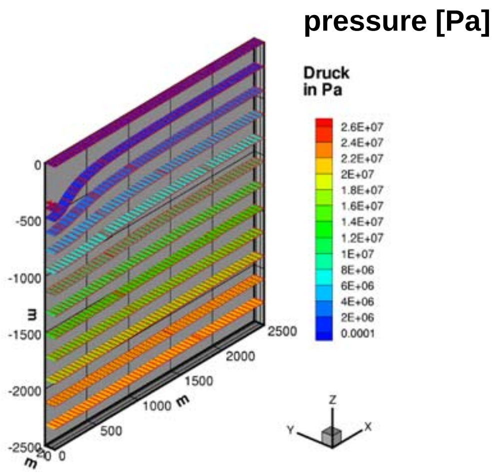

Figure 2.2-4: Enlarged model: isoplanes of the pressure at steady-state

The ratio of transmissivity values of fracture and matrix coincides with the ratio of the respective flow rates. The same applies to a variation of the base case where the fracture permeability is reduced by a factor of ten. The variant provides the same matrix outflow as in the base case but only one tenth of the fracture outflow which suggests that the contribution of the matrix to the steady-state flow is negligible. It is therefore sufficient to model steady-state flow in the fracture only. It is preferable as well, because the computational effort can be reduced considerably by restricting to a vertical 2D-fracture model.

Immediately after excavation the flow field was in a transient state due to the rock storage capacity. The rapid pressure reduction around tunnel and niche caused the matrix to release water and to contribute it mainly to the fracture. At this stage the pressure field deviates considerably from its final form. Before switching to a 2D-fracture model it must be ensured that steady-state conditions are already reached in the Äspö flow domain.

Storage effects can have different reasons like the elasticity of the rock, compressibility of the fluid, encapsulated air bubbles etc. All these effects were condensed in the specific storage coefficient. This coefficient was estimated to lie at 10-7 m^{-1} in the matrix and 10-6 m^{-1} in the fracture based on data from SKB /RHE 97b/.

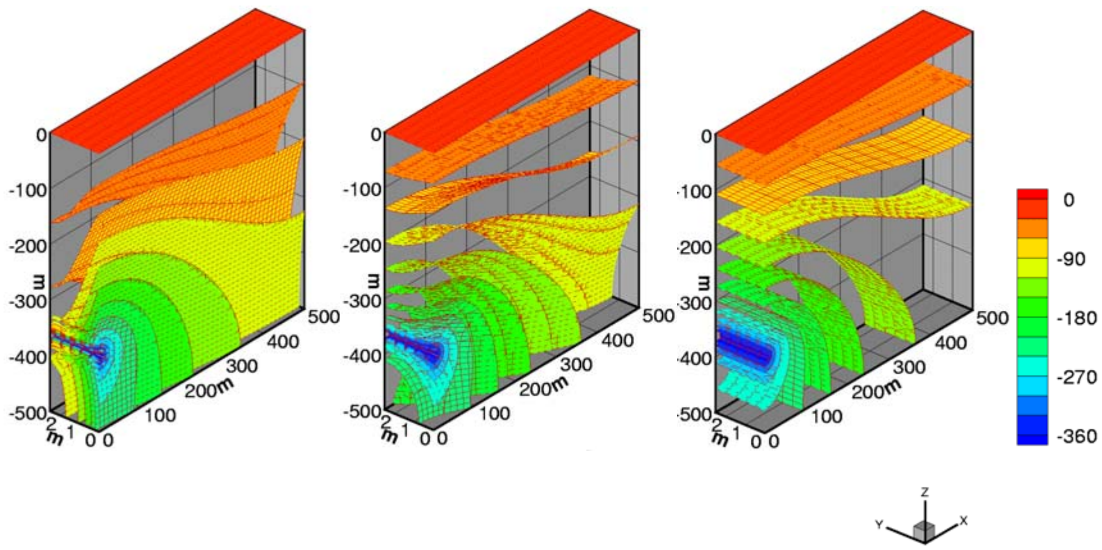

Figure 2.2-5: Transient model: isoplanes of the hydraulic head at 1, 3 and 10 months

Instantaneous excavation was assumed in the numerical model. Therefore the simulation started with a hydrostatic pressure field (or a constant hydraulic head of zero metres) depicting the hydraulic condition immediately before excavation but with the atmospheric pressure boundary condition assigned to the niche. The calculations were continued until the outflow was nearly the same as in the steady-state model. Figure 2.2-5 shows the hydraulic heads at one, three and ten months. As in the Figure 2.2-1 the fracture lies in the vertical plane which faces the reader.

Despite the higher storage capacity in the fracture it is apparently almost at steady-state in less than a month. At that time mass flux out of the fracture lays only 1% above the steady-state value yet, meaning that the matrix contributes very little to the fracture flow during transient conditions. After ten months the whole system reaches stationary state. The excavation for the Äspö Hard Rock Laboratory was started in 1990. From the numerical models it can therefore be concluded that the groundwater flow system at the Äspö-site is presently at steady-state.

Variation of the storage coefficient in the fracture shows that the transient phase of the flow field after excavation is mainly controlled by the matrix storage capacity. This is due to the fact that the matrix volume is a hundred times higher than the volume of the fracture. But in the transient state the matrix still has no noticeable effect on fracture flow. Fracture storage capacity on the other hand is not large enough to exert a long-term influence on the flow field. This was confirmed by transient flow tests at a later stage (see next paragraph). These clues justify abandoning the three-dimensional models in favour of a vertical two-dimensional plane model of the V2-fracture.

During the numerical exercise described above new data about the V2-fracture had been obtained. Several boreholes crossing the V2-fracture in the vicinity of the niche had been drilled (see Figure 2.2-6) and provided with a packer system. Some flow tests were performed in which several of the test boreholes were opened one at the time while the pressure response at the other locations was monitored. Water-flow rates from the opened holes were measured as well. When steady-state conditions were reached the opened borehole was closed again. The next hole was not opened until the pressure was back up to the initial values at all locations.

The time dependent behaviour of the flow is controlled by storage coefficient only. The time, necessary to reach steady-state conditions in the experiments, can therefore be used to check the storage capacity value in the numerical model. One has simply to assign atmospheric pressure to one of the test boreholes in the model and to observe the change of pressure at the other locations over time. This check was performed for the V2-fracture.

The measured values for the pressure in the undisturbed flow field lay between 1.8 MPa and 1.83 MPa with two exceptions. KXP05GRS and KXP26BGR showed 0.53 MPa and 1.91 MPa, respectively. It was therefore decided to check the storage capacity in a simplified model for the fracture area where the almost uniform high pressure was found. The niche as well as the undisturbed flow is not considered in this model. Hence, the results can be interpreted qualitatively only.

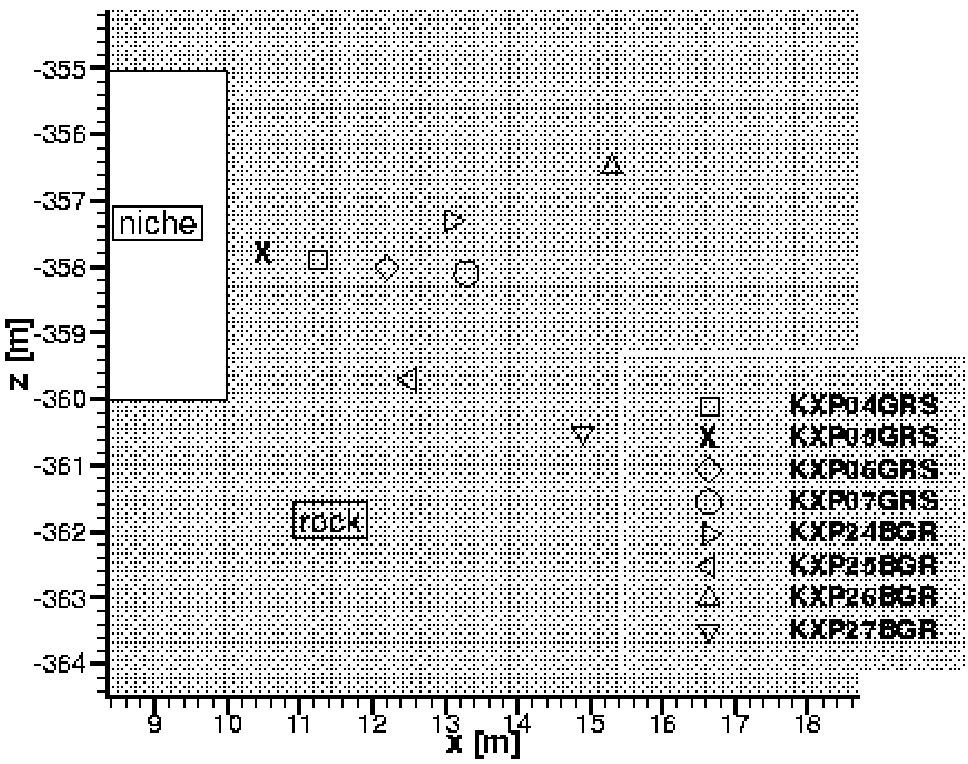

Figure 2.2-6: Position of measuring points in the fracture relative to the niche

Figure 2.2-7 and Figure 2.2-8 show the measured and simulated pressure at the test locations over time for a flow test at KXP24BGR and KXP25BGR, respectively. The simulated dynamics of the pressure drop in the fracture are in good agreement with the measurements even if the pressure at steady-state conditions does not coincide well.

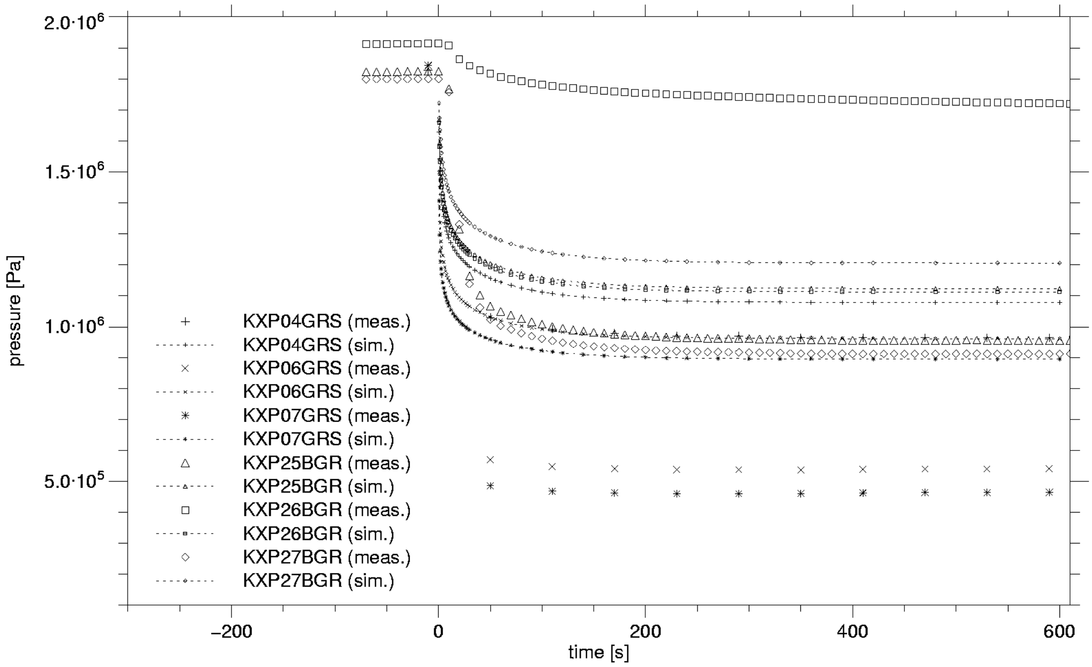

Figure 2.2-7: Measured and simulated pressure after opening KXP24BGR

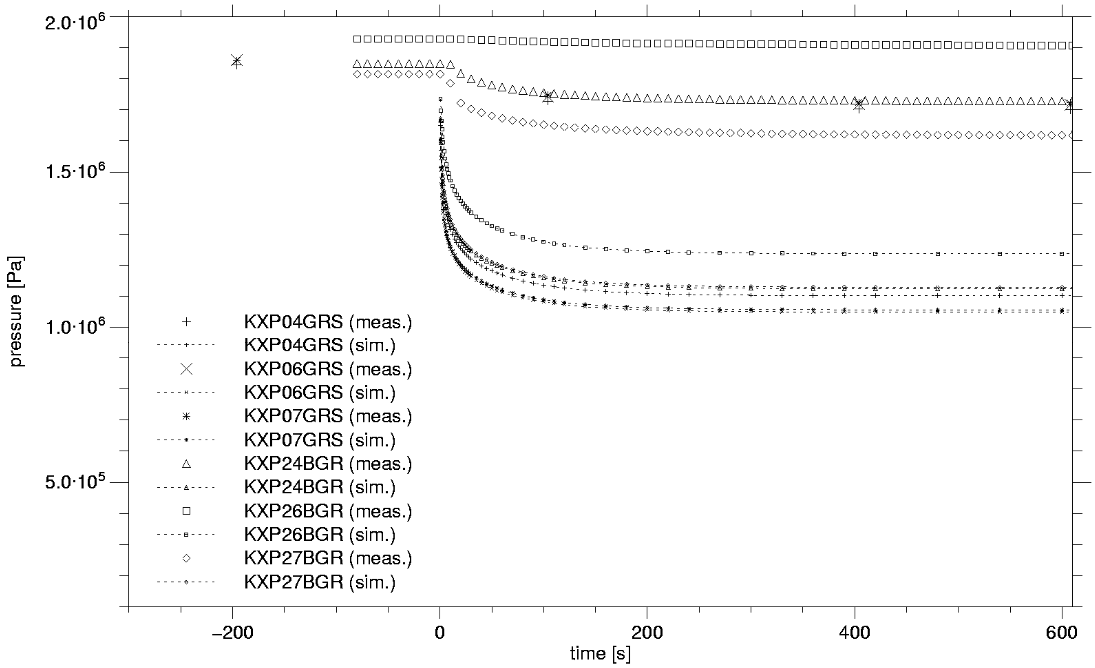

Figure 2.2-8: Measured and simulated pressure after opening KXP25BGR

This confirms the estimation for the storage capacity in the numerical model and thereby the assumption about stationary state of the flow field in the fracture. It indicates further that the description of the model domain as a homogeneous medium is not appropriate.

2.2.2 Inhomogeneous Single-Phase Flow Models

The measurements of water pressure in the undisturbed flow field of the fracture were obviously in contradiction with the models considered so far. In the calculations the water pressure increased more or less linearly with distance from the niche wall (see Figure 2.2-9) [1] while the measured pressure distribution was characterised by two unexpected features. Firstly, a sharp pressure increase in the immediate vicinity of the niche wall and secondly, a high degree of uniformity at a surprisingly high level in the remaining area.

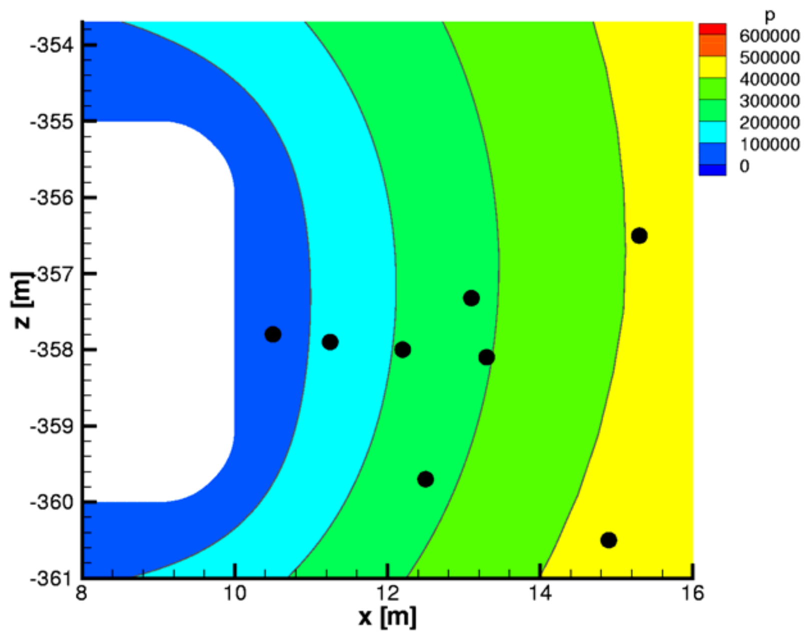

Figure 2.2-9: Pressure distribution in the measurement area of the homogeneous model

[1] Note, that in Figure 2.2-9 the corners of the niche are rounded in order to avoid numerical difficulties.

Even at the test borehole KXP26BGR which was located furthest apart from the wall the calculated pressure amounted to about 0.5 MPa compared to the measured pressure of 1.9 MPa. Therefore the assumption of a homogeneous permeability distribution was no longer tenable.

The most simplest explanation consistent with the new data was the assumption of a narrow zone - probably less than one metre in thickness - surrounding the niche. This zone would have to be hydraulically much tighter than the neighbouring area in which the pressure measurements were performed. Such a constellation would account for the sharp pressure gradient. But in order to get the almost constant, high level pressure field as well, a third zone with an intermediate permeability was required beyond the measurement area. In the third and outer zone the pressure had to drop from the approximately 1.8 MPa in the middle zone down to atmospheric pressure at the top of the model.

In this three-zone model the permeability of each zone was varied under several constraints:

- achieve a minimum pressure gradient in the middle zone
- get a pressure level of about 1.8 MPa in the middle zone
- maintain an outflow rate of about 3 $l\ min^{-1}$

The dimensions of the zones had to be determined as well. Considering the pressure distribution along the GRS boreholes (see Figure 2.2-10) a thickness of one metre for the inner zone was chosen. There was no clue though for determination of the size of the middle zone. A thickness of 40 m for the middle zone was therefore assumed without further reasoning.

The model geometry and boundary conditions are given in Figure 2.2-11 as well as the permeability values resulting from the parameter variations. Under these conditions an outflow of 2.2 $l\ min^{-1}$ is calculated in the three-zone model and the pressure gradient in the range of the test boreholes is considerably reduced (see Figure 2.2-12).

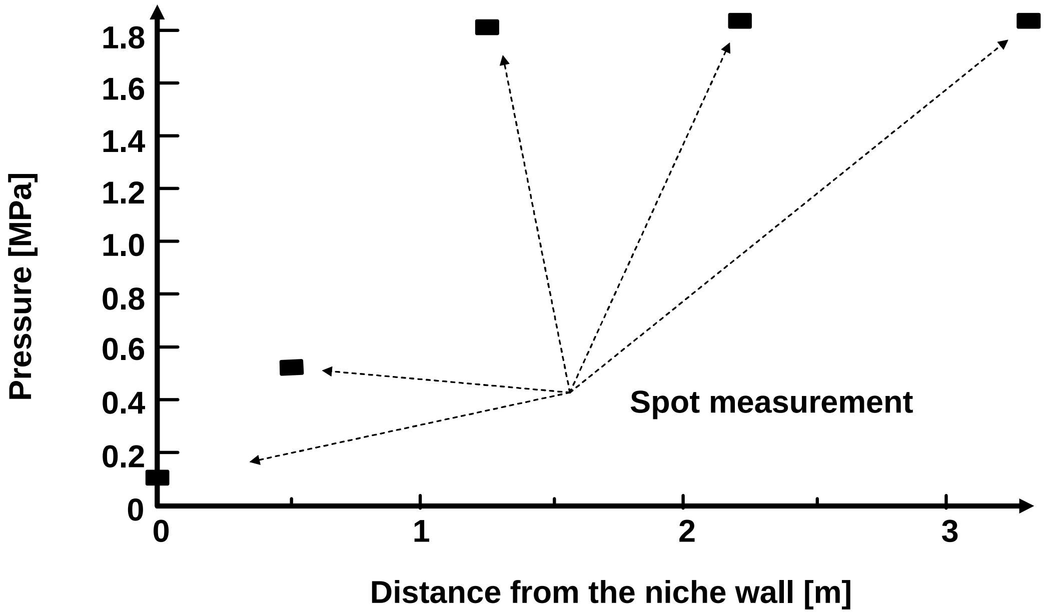

Figure 2.2-10: Pressure distribution along the GRS boreholes

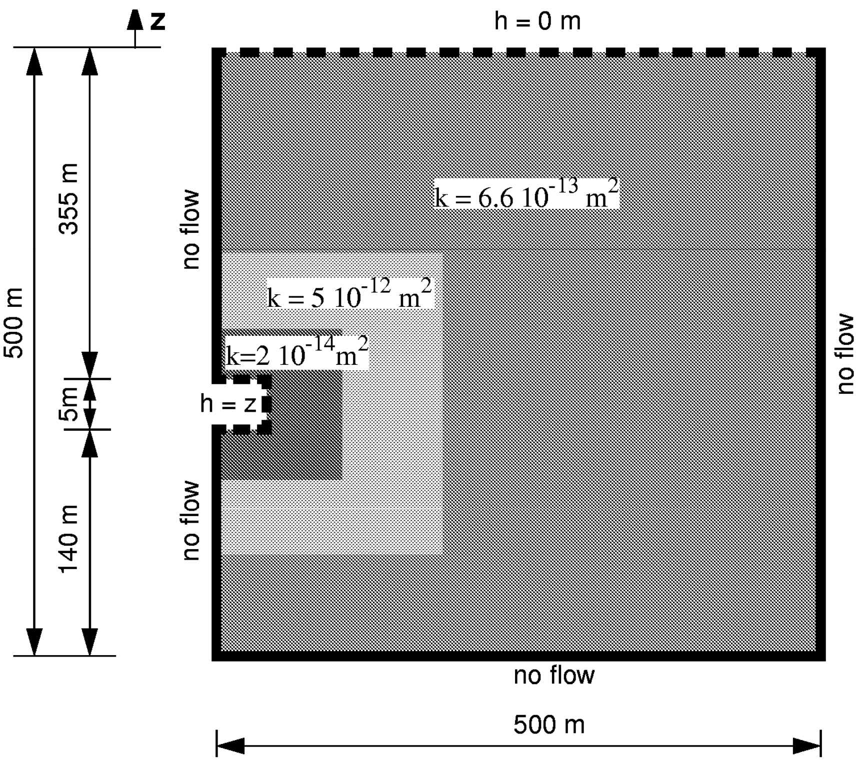

Figure 2.2-11: Geometry and boundary conditions of the 2D-fracture model with variable permeability (three-zone model)

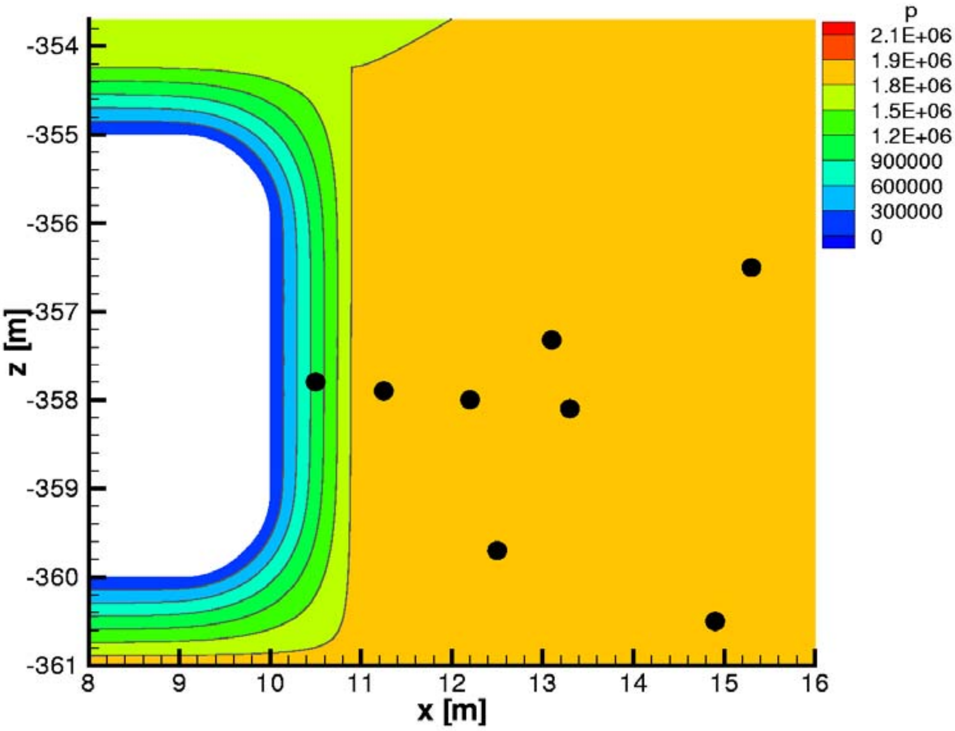

Figure 2.2-12: Pressure distribution in the measurement area of the three-zone model

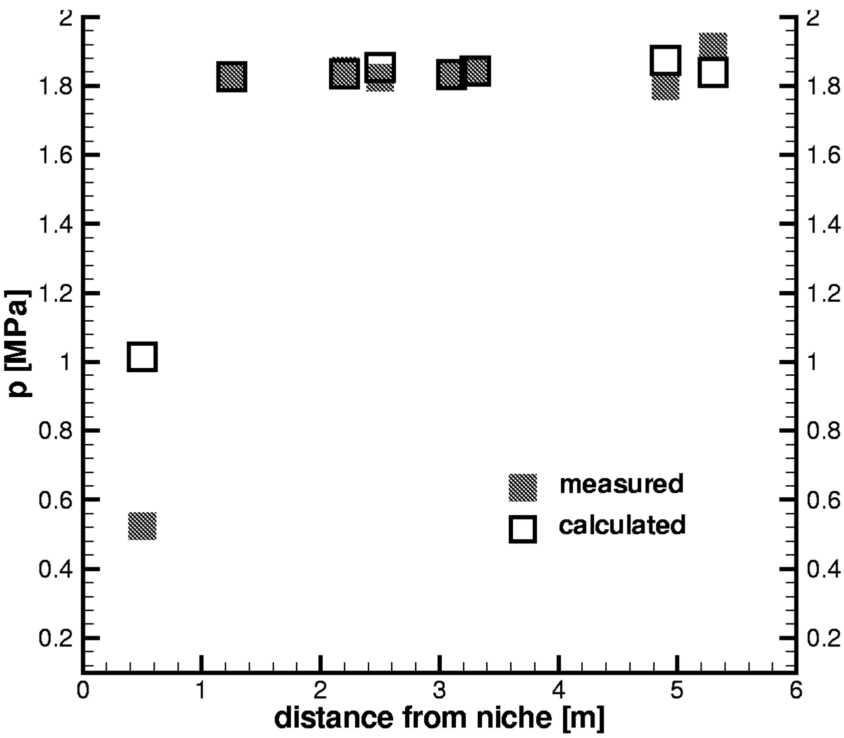

Figure 2.2-13: Comparison of pressure values from measurements and from the simulation with the three-zone model

Measured and calculated pressure match fairly well at most test location (see Figure 2.2-13). The comparatively low pressure value at KXP05GRS is not well met but this is of secondary importance. It is to be expected that the permeability in the inner zone depends strongly on the distance from the niche wall. Furthermore, the size of this zone is not well known so that the calculated pressure value could quite easily be adjusted, given additional data.

An interesting property of the three-zone model is that the influence of the excavation on the pressure field is not as far reaching as in the homogeneous model. Figure 2.2-14 shows a comparison of both model results. The black isolines representing the pressure from the three-zone model are less bend than the white isolines from the homogeneous model. The pressure of the three-zone model increases faster with depth and deviates thereby less from the hydrostatic conditions. This is more consistent with the general understanding of the hydro-geological situation.

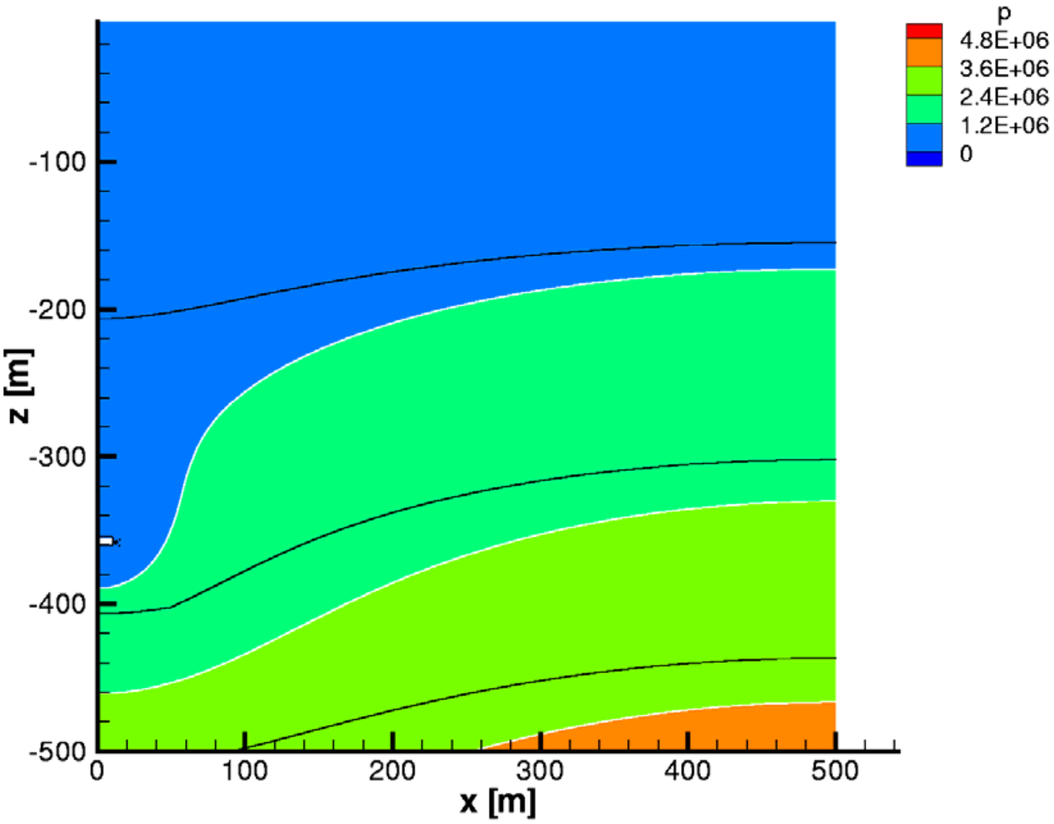

Figure 2.2-14: Large-scale comparison of the pressure fields: homogeneous model: coloured area plus white isolines; three-zone model: black isolines

It should be mentioned, though, that the comparatively high pressure value at KXP26BGR cannot be explained even by the three-zone model. A probable reason for this phenomenon could be the neglected inhomogeneity of the flow domain. The same reasoning applies for the fact that the required uniformity of pressure field in the range of the test boreholes could not be obtained completely because the influence of the hydraulic pressure gradient could not be cancelled out. It must therefore be concluded that maybe not all important hydraulic features are included in the three-zone model. But it produces a much better approximation of the flow system than the homogeneous model.

2.2.3 Two-Phase Flow in Local-Scale Models

The large-scale single-phase flow model described in the previous chapter was used as a starting point for the local-scale two-phase flow simulations. It provided initial and boundary conditions for the pressure. These data had to be transferred to the two-phase-flow model which required some additional effort because the grid had to be changed due to new demands:

- The appropriate size of the new model could not be determined beforehand because the dipole experiment changed the flow field to an unknown extent. It had to be ensured that only minimal changes reach the new boundaries.

- Dipole-like flow implies strongly curved streamlines which had to be captured by the element grid. In order to avoid unnecessary computational effort the elements around source and sink had nevertheless to be as large as possible.

The domain size complying with these demands was about thirty by thirty metres (see Figure 2.2-15). It had Dirichlet-type boundary conditions for pressure as well as saturation all along the boundary. The pressure values were interpolated from the single-phase flow model, the gas saturation at the boundary as well as the initial value over the whole domain was chosen to be 0.1%.

The local model domain encompassed two of the three regions of the three-zone model. The permeability values of $2 \cdot 10^{-14}$ m^2 for the inner zone at the niche wall and $5 \cdot 10^{-12}$ m^2 for the adjacent zone were used in the two-phase-flow model. Fracture porosity was assumed to be 20% in the whole model.

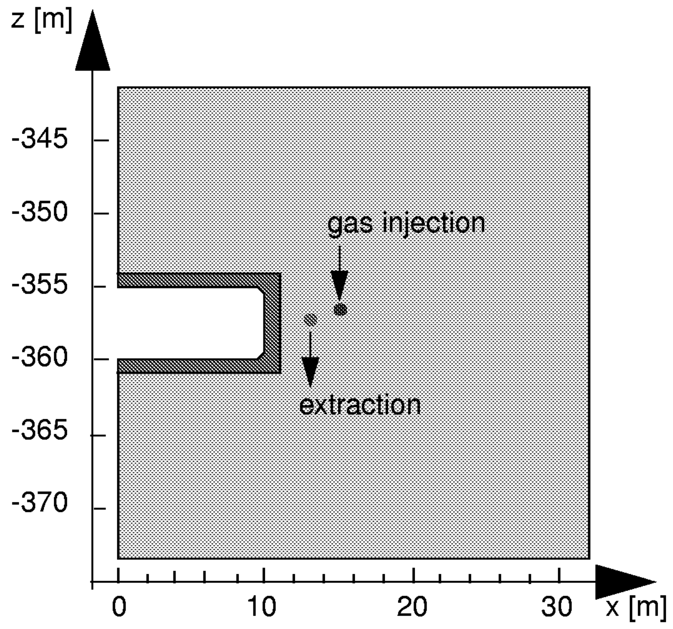

Figure 2.2-15: Geometry of the two-phase-flow model

A mass flux equivalent to two litres of nitrogen per minute was assigned to the location of the injection borehole. But at the extraction point the boundary needed some more attention. The outflow rate was not known and the saturation was an unknown function of time. So neither a Dirichlet nor a Neumann boundary condition could be applied. In order to circumvent this problem a string of one-dimensional elements was connected to the extraction point in the model. The elements had a very high permeability to avoid an artificial flow resistance and the additional volume was large enough to prevent the injected gas from leaving the model domain. In other words, the simulated front of gas saturation could leave the fracture but not reach the model boundary. This measure allowed the use of fixed pressure and saturation values at the end of the 1D-element string. Since the string is not real and just to provide appropriate boundary conditions it will not be discussed in the following.

One of the project goals was to derive the saturation dependent relative permeability and capillary pressure from inverse modelling of the dipole tests. This was not possible because the experiments were started too late to provide the necessary data in time. Instead, Brooks-Corey functions were used as a first approximation (see Figure 2.2-16). From other experiments it was known that the entry pressure p_e was very low. After experience, from conventional soils the parameter, α was chosen. The values α=2 and p_e=100 Pa were used in the model.

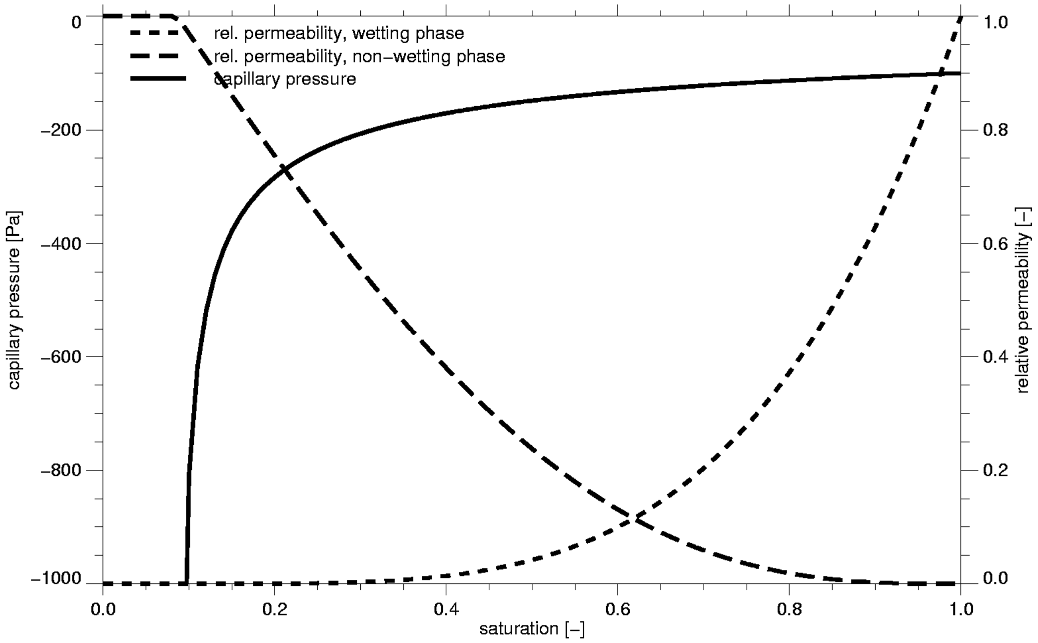

Figure 2.2-16: Saturation dependent functions for the first two-phase-flow model

The calculations were performed with the two-phase-flow code MUFTE-Thermo version 4 /HEL 94/. It simulates the simultaneous flow of gas and water taking the phase changes evaporation, condensation, solution and dissolution into account. Like the ROCKFLOW code it allows the simultaneous use of elements with different dimensionality. This simplifies the special treatment of the outflow boundary at the extraction borehole described above.

At the beginning of the simulation the gas mobility is low so that the injected gas accumulates and increases the pressure. An almost radial displacement of water can be observed in the very first injection phase (Figure 2.2-17).

With increasing gas saturation the mobility increases as well. Less pressure is necessary to move the gas in the direction of the extraction borehole. The pressure gradient in the upstream direction changes the sign and the gas on the upstream side of the injection borehole is driven back (Figure 2.2-18).

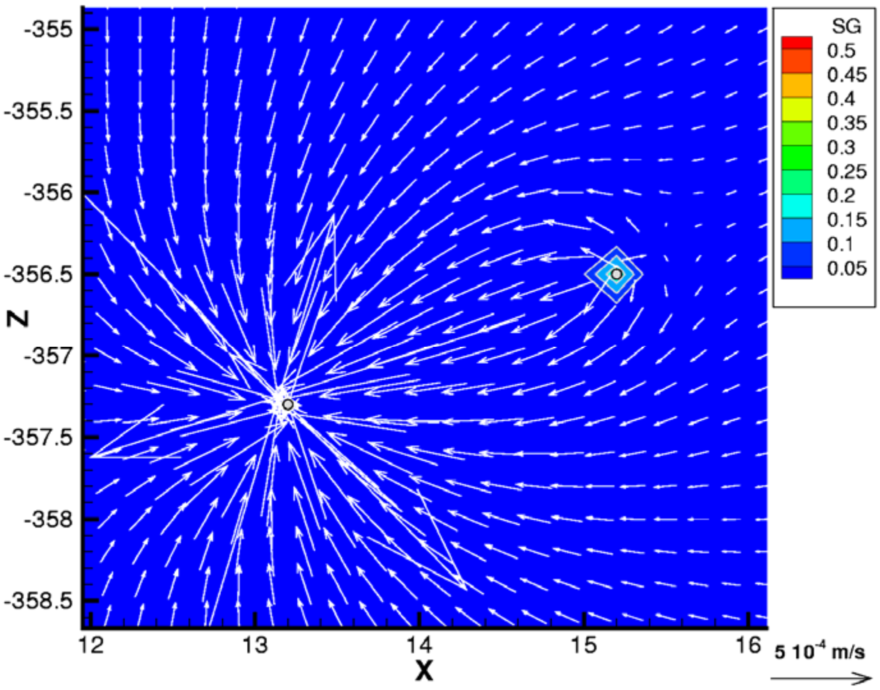

Figure 2.2-17: Gas saturation and water velocity after 10 s in the two-phase-flow model

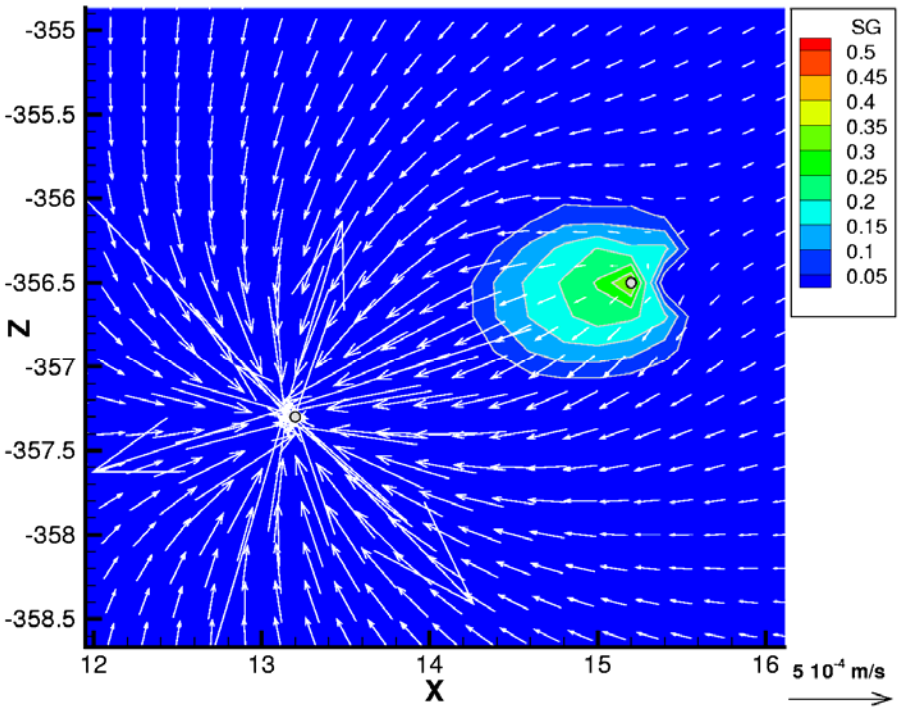

Figure 2.2-18: Gas saturation and water velocity after 120 s in the two-phase-flow model

From that time on the gas flow is mainly influenced by the water pressure because the variance of the capillary pressure is negligible compared to the hydraulic pressure gradient between injection and extraction borehole. On the way to the extraction point the gas plume is relatively narrow. A certain spreading is due to the radial flow pattern at the injection borehole. Additionally, the effect of buoyancy can be observed and it makes sure that the plume disperses more in the upward direction than downwards (Figure 2.2-19).

The saturation peak close to the extraction point has no physical reason but is caused by numerical difficulties at the extraction borehole. Physically, the gas saturation at the point sink must be the average of the arriving gas saturation weighed by the flow rate. A smooth solution for the saturation in this patch can therefore be obtained only, if the saturation is constant around the sink. Otherwise there is a jump in the solution exactly and exclusively located at the point which represents the sink. This kind of mathematical function cannot be approximated by means of the finite element method and hence introduces a certain error in the solution.

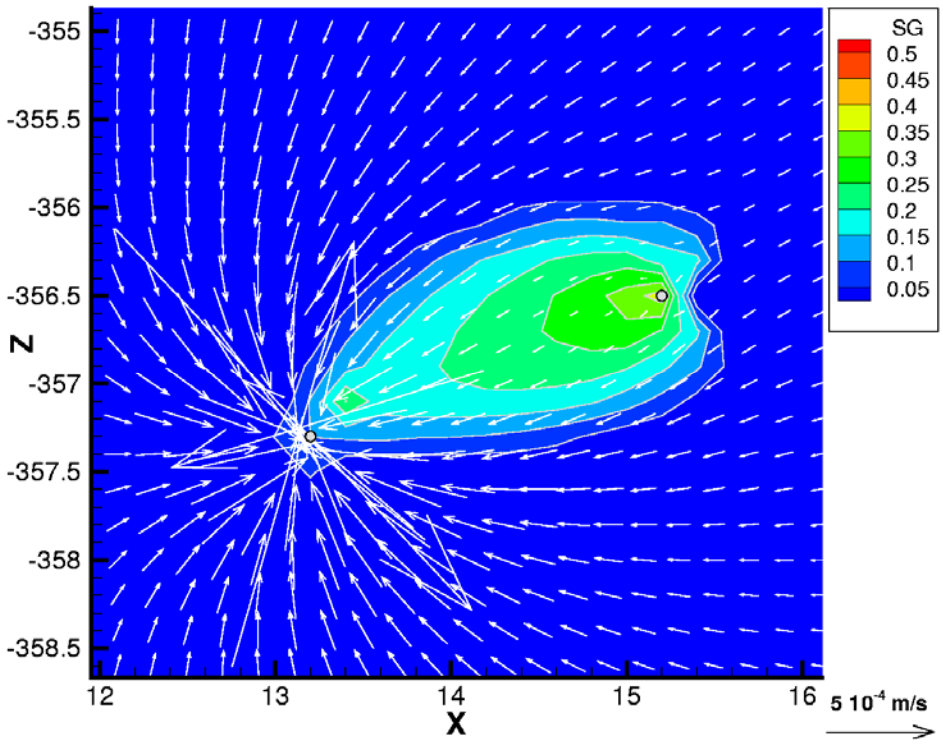

Figure 2.2-19: Gas saturation and water velocity after 300 s in the two-phase-flow model

Some of the input parameters which were not well known like the initial gas saturation were varied in order to minimise these errors. The results presented above were calculated with the most suitable parameter set.

The extension of the gas plume changes little after the gas has reached the extraction borehole. Steady-state conditions are reached approximately after 900 s. The narrowness of the area with high saturation values becomes even a little more pronounced (Figure 2.2-20).

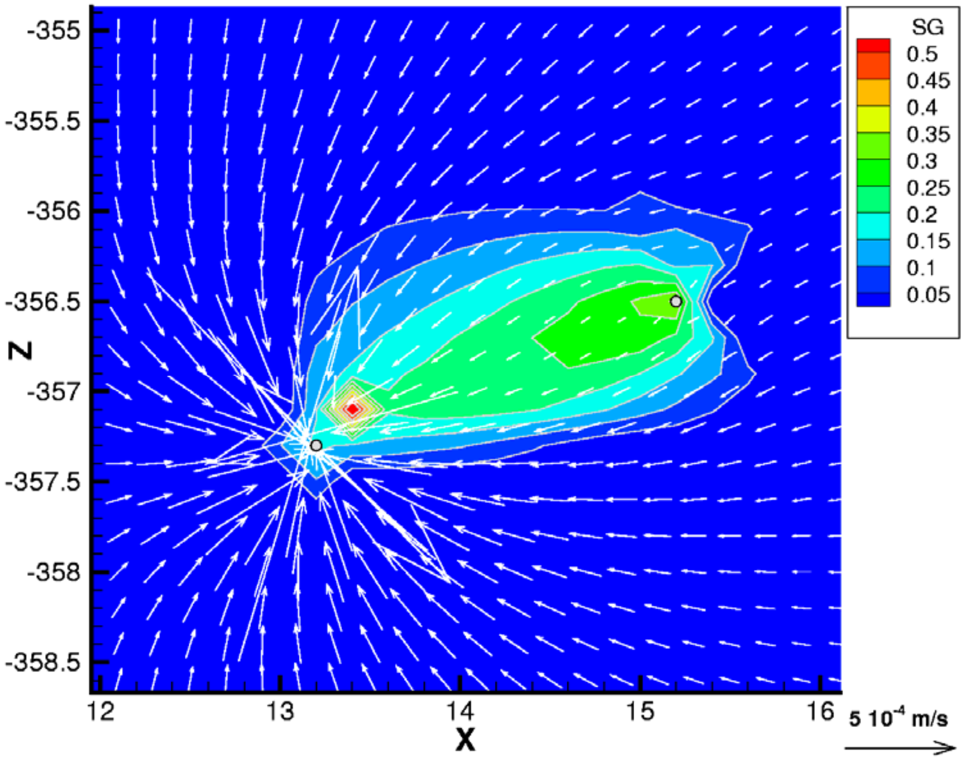

Figure 2.2-20: Gas saturation and water velocity after 1200 s in the two-phase-flow model

2.2.4 Summary and Conclusions from Numerical Simulations

Even if a comparison with the actual test data was not possible due to the late beginning of the dipole tests, some observations taken from the two-phase-flow model should be noted. Firstly, flow out of the niche wall is not significantly influenced by the dipole test. This means that under the circumstances assumed for the model a full recovery of the injected gas can be expected. Secondly, breakthrough occurs after 250 s in the model, steady-state for all practical purposes is reached after about 600 s. As a result of this model the dipole tests should take time on the order of a quarter of an hour. Deviations from these predictions should provide valuable information about the V2-fracture and possibly allow for substantial changes of the investigated model.

Comparative calculations with varied input parameters confirmed that even an increase of the capillary pressure by a factor of 15 has no impact on the simulations. The same applies to some extend to the mathematical form of the relative-permeability-saturation relationship. Model results with a linear function show essentially the same saturation distribution as the results obtained with the Brooks-Corey function. A dipole test performed with gas only would therefore provide not enough information to identify the saturation dependent conclusively. It has to be mentioned though, that no indications for an appropriate value for the parameter α in the Brooks-Corey function was available. A sensitivity analysis with respect to the α–parameter was not possible due to time restrictions.

2.3 MUFTE_UG - Code Development and Model Concepts

Peter Bastian, Rainer Helmig, Hartmut Jakobs, Volker Reichenberger

The urgent need for disposal sites for biological, chemical, and radioactive waste has directed interest towards the possible use of rock dumping sites, because they are considered to be virtually impermeable in many cases. However, natural barriers formed by rock material are usually interlaced with fractures and shear zones which are generally interconnected over long distances. In view of the latter, flow processes may indeed occur, even if they are slow.

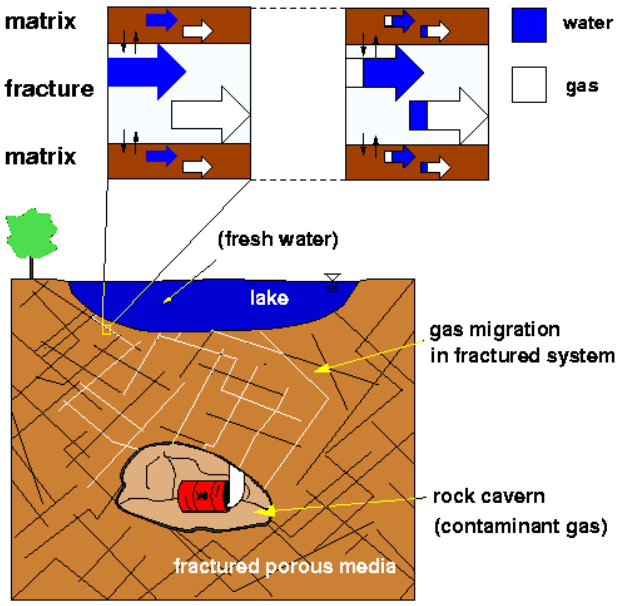

Figure 2.3-1 Two phase flow and two phase two component flow and transport in a fractured rock system in a deep repository

The following section is a shortened version of a detailed report given in /HEL 00/. It focuses on model concepts, examples and upscaling.

The escape of polluting materials from disposal dumps (e.g. oils, halogenated hydrocarbons) or rock caverns (e.g. contaminated gas, Figure 2.3-1) leads to instances of pollution, which must be taken into consideration, particularly in view of the desirable long-term safety of the disposal sites. Measurements carried out in existing rock caverns as well as below disposal dumps confirm such cases of pollution. It is therefore essential to carry out investigations concerned with the migration behaviour of contaminants.

From the physical point of view, the escape of polluting materials often involves fluids which are immiscible with water or only slightly soluble. As they are thus present as separate phases in rock, flow investigations must be described in terms of multiphase multicomponent flow and transport processes.

For simulating flow and transport processes in fractured rock, a major prerequisite is the possibility of coupling discrete fracture systems and a rock matrix model (see Figure 2.3-3). The model described in this report employs the concept of a porous medium for the matrix in conjunction with a discrete approximation for the fractures, particularly in view of the desirable long-term safety of the disposal sites concerned, (/HEL 93/ and /BAS 00/). A numerical model based on the finite volume method is presented for simulating two phase two component flow and transport processes under the special conditions pertaining to a fractured porous medium.

The physical description and the discretisation techniques for these processes within porous media are provided by the simulation software **MUFTE_UG** (**MU**ltiphase **F**low, **T**ransport, and **E**nergy) /HEL 94/.

Fractured media lead to complex domains which demand the use of unstructured grids. The numerical simulation toolbox UG offers sophisticated numerical tools such as multi-grid methods and adaptive refinements for unstructured grids on workstations and parallel computers /BAS 97b/.

Both tools have successfully been combined to MUFTE_UG - a very efficient toolbox for the simulation of multiphase multi-component processes within porous media /BAS 96/, /BAS 97a/, /HEL 98/.

2.3.1 Two-Phase Flow in Fractured Porous Media

2.3.1.1 Simulated Processes

Two kinds of systems are regarded for two-phase-flow processes: the two phase system assuming that the phases are not soluble in each other and the two phase two component system, where phase transition processes are considered. However, even the approach regarding two components assumes that thermodynamic equilibrium is reached instantaneously after change of pressure or temperatures, i.e., the phase transition processes are much faster than the simulated effects.

Regarding both systems advection and convection may be caused by pressure gradients (as a result of boundary conditions or source and sink terms), capillary forces or by the difference in density between the two phases. The two components within each phase may be also transported because of diffusion due to concentration gradients of the components within each phase.

The phase transfer processes (Figure 2.3-2) which are taken into account are degassing, dissolution, evaporation, and condensation. These processes are computed via Raoult's Law, Henry's Law, Dalton's Law and the Ideal Gas Law.

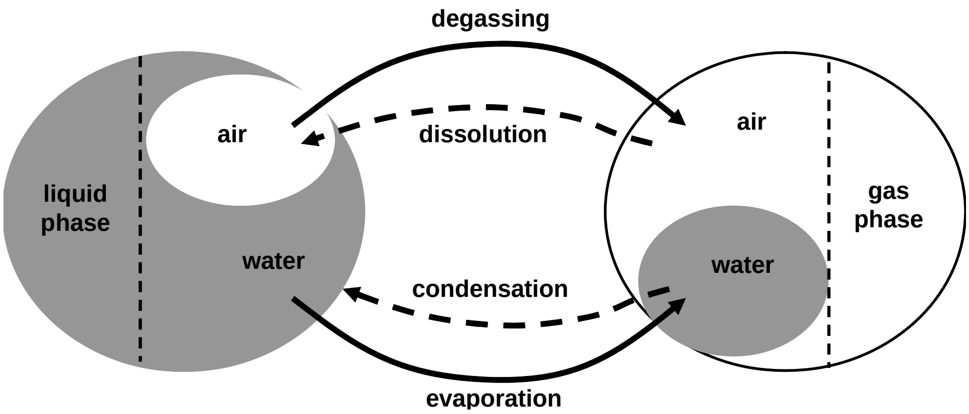

Figure 2.3-2: Phase Transfer Processes. Transfer of the components air and water from the liquid phase (left ellipse) to the gas phase (right ellipse) and vice versa

2.3.1.2 Discretisation with Fractures

The difficulties in describing a fractured porous medium arise as the diameter of a fracture is very small compared to the length of the system and the differences of property values between the fractured system and the matrix system are very large. So the flow velocities are much higher in the fractures while the storage capacity of the matrix is much greater compared to the fractured system (Figure 2.3-3).

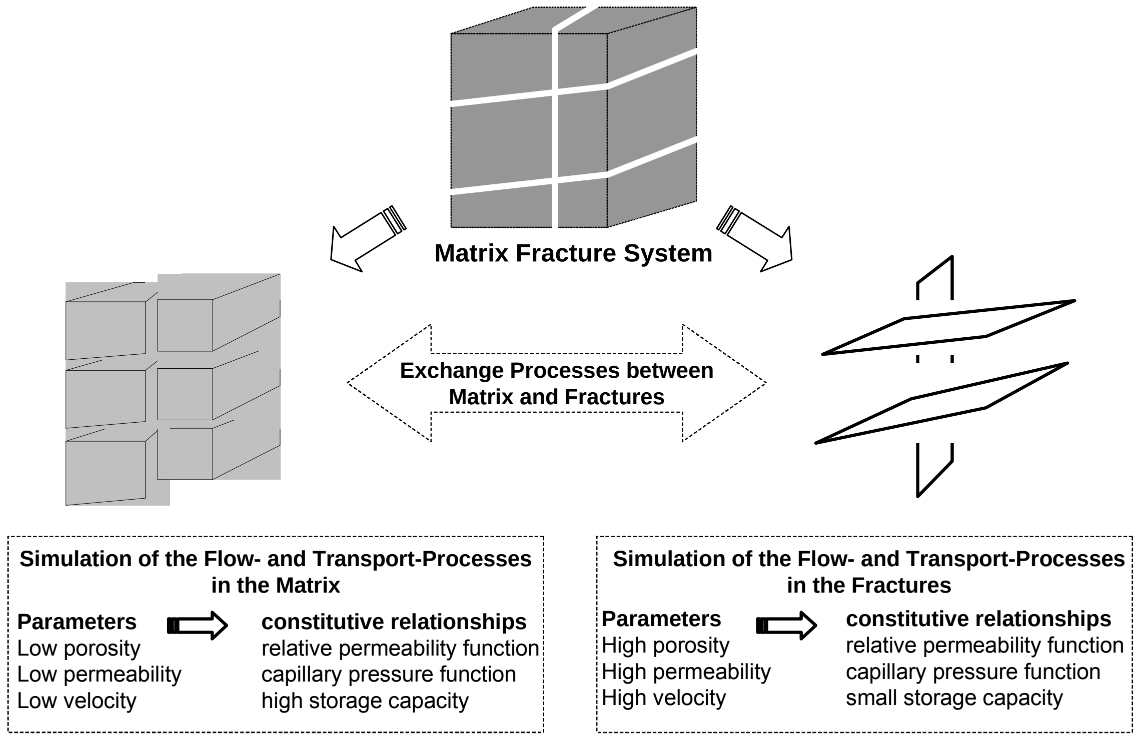

Figure 2.3-3: Describing a fracture matrix system

Due to the small diameter of the fractures there are many advantages in describing them as elements of lesser dimension. In Figure 2.3-4 the treatment of fractures can be seen.

The fracture elements are described as edges of the 2D elements. Similarly the fracture elements are described as 2D planes of the 3D elements.

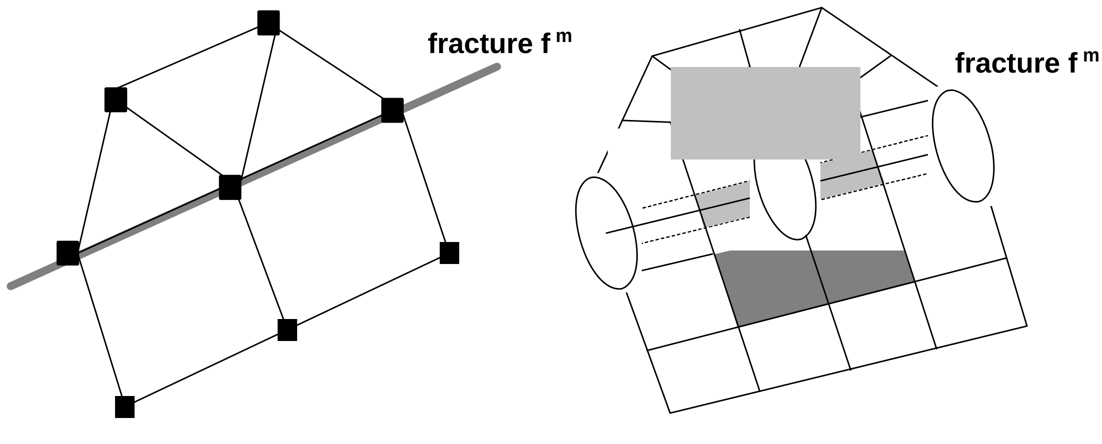

Figure 2.3-4: Fracture in a 2D-grid and Finite Volumes (3D) for fractures

2.3.1.3 Exchange Processes between Fracture and Matrix

Regarding the problem of gas migration within initially fully saturated fractured porous media it had to be made sure that numerical dispersion of gas from the fracture system into the matrix system had to be prevented. As the fracture elements are of lesser dimensions it is impossible to reach a suitable refinement of the grid to achieve this. Even for the most refined grid there is still an error due to the linear interpolation between the nodes. One solution for this problem is to use the so called Phase Pressure Saturation Interface Condition where one node can have different virtual saturation values.

This is achieved computing the saturation with the inverse capillary pressure function for those domains where the capillary pressure is not minimal (see Figure 2.3-5). Using this interface condition the entering of a gas phase into the matrix is governed by the entry pressure of the matrix using the Brooks-Corey capillary pressure saturation relationship.

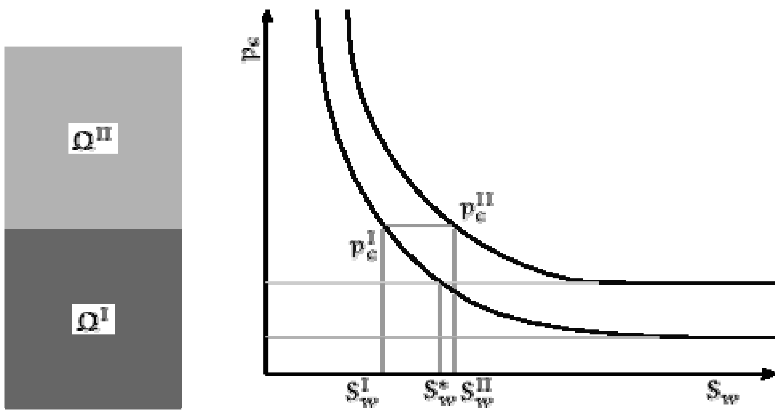

Figure 2.3-5: Capillary pressure for discontinuous media

2.3.1.4 Fracture-System Generation

From the very moment that the discretisation for fractured porous media is finished and debugged with simple domains, the necessity for more complicated domains arises, along with the realisation that the generation of these domains is a difficult and complicated process. Not only is the input of the domain description tedious, but it also requires profound geological knowledge to create realistic fractured domains. Annette

Hemminger from the CAB, University of Braunschweig, developed a fracture generator, that can generate domains based on prescribed geological properties /HEM 99/.

Based on the stochastic approach, a fracture generator has been developed which creates fracture networks in 3D, where the fracture elements are represented by 2D rectangle elements and as 1D element in a 2D clipping plane. A 3D realisation and a 2D clipping plane can be seen in Figure 2.3-6. The figure shows that in order to avoid generating errors at the outer domain boundaries, a sub domain is cut out of the 3D and 2D domain. The generating algorithm creates fracture planes in space according to the given fracture density, spatial orientation, and trace length distribution. The information of the trace distance is not yet included.

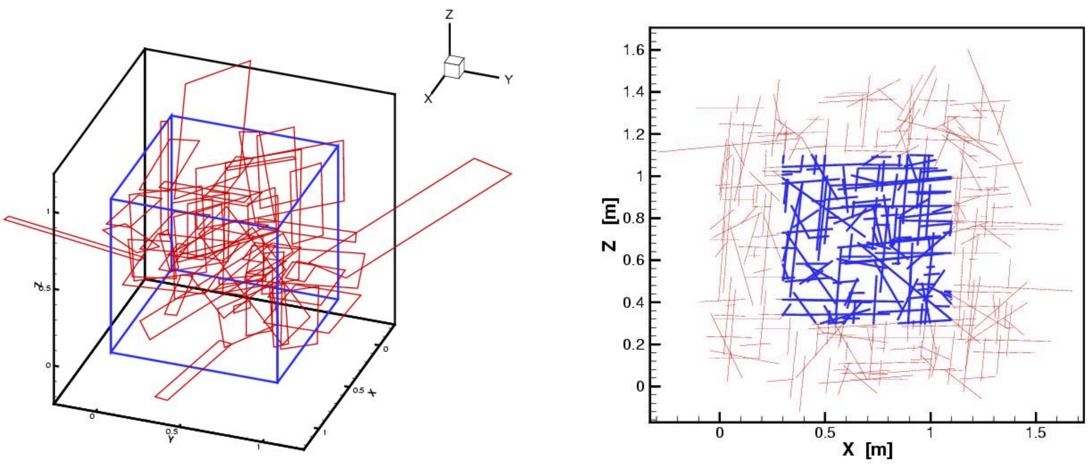

Figure 2.3-6: Different fracture systems: (left) 3D fracture network (fractures as 2D rectangle elements in space). (right) 2D fracture network (fractures as 1D elements)

2.3.1.5 Interface to MUFTE_UG

MUFTE_UG can directly handle the information from the fracture generator and create a boundary value problem description from it. In order for this to work, the user has to provide functions for fluid and media properties and boundary condition functions. They are connected to the boundaries by the property number generated by FRAC3D. The grid generator also uses the property information and retains this information in the grid description file.

The format of the grid description file is similar to the domain description. Vertices, edges (with an index number describing on which boundary it lies) and faces are the building blocks of the grid in two dimensions. MUFTE_UG can also directly read these grid files to define the finite element mesh.

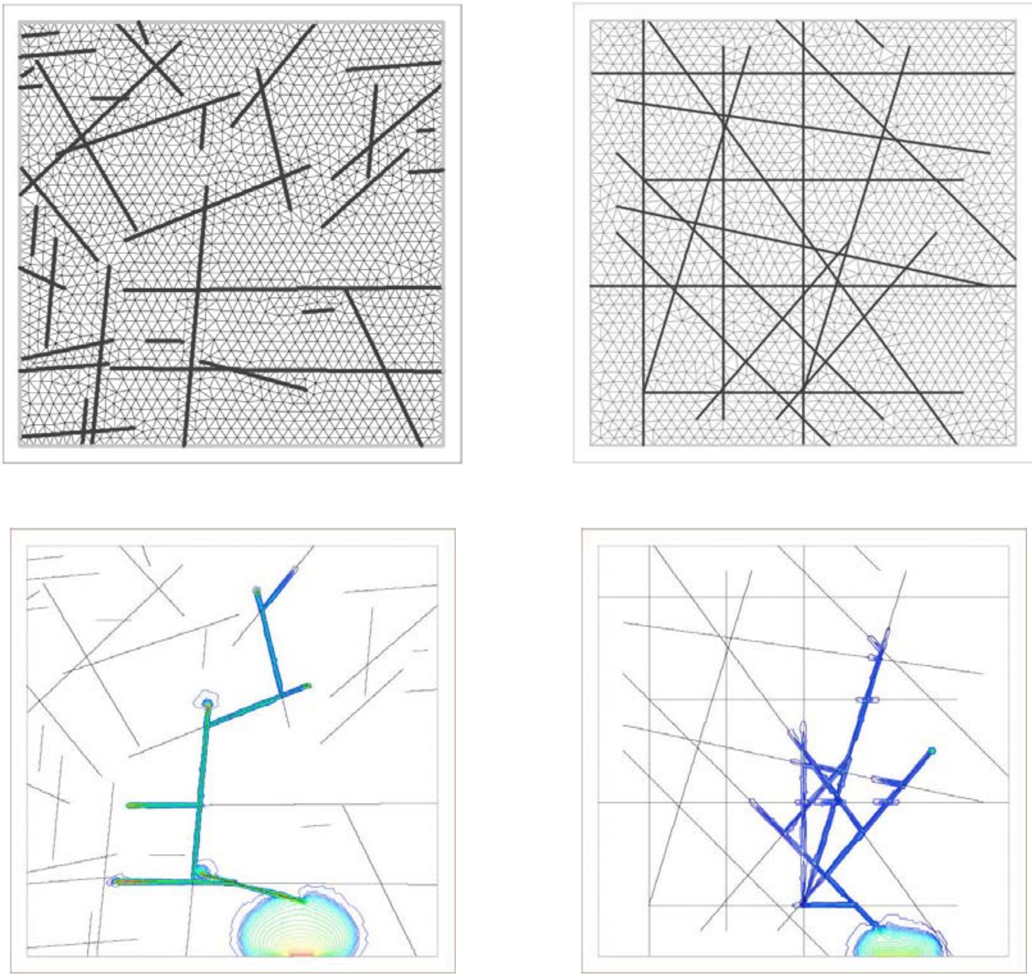

Figure 2.3-7: Two domains created by the fracture generator FRAC3D and saturation plots from a gas water simulation

Figure 2.3-7 shows two domains that were generated by the fracture generator and meshed with the grid generator. The coarse grid on the left consists of 3468 elements and 1817 vertices. The grid on the right has 3093 elements and 1625 vertices.

To show the ability to use these grids for multiphase flow simulation two saturation isolines plots are included. The domain size is 8 m by 8 m in both cases. The configurations of the problem consist of a fully water-saturated domain which is infiltrated with gas from the bottom boundary.

The UG multi-grid method was used for the solution of the linearised systems, with an exact solver for the coarse grid. We used two levels of refinement, with adaptive refinement around the fractured regions in the last step. Up to coarse grid sizes with less than 5000 nodes the exact solution of the coarse grid problem is feasible, but for coarse grids greater than this the solution time gets large. For problems of that complexity, the algebraic multi-grid solver of UG can be used as a coarse grid solver. This has already been done successfully for coarse grids with more than 7000 vertices and 12000 elements.

2.3.2 Examples

2.3.2.1 Gas-Water Flow and Transport in Fractured Medium (2D)

The domain for this example can be seen in Figure 2.3-8. The domain size is 8 m by 10 m.

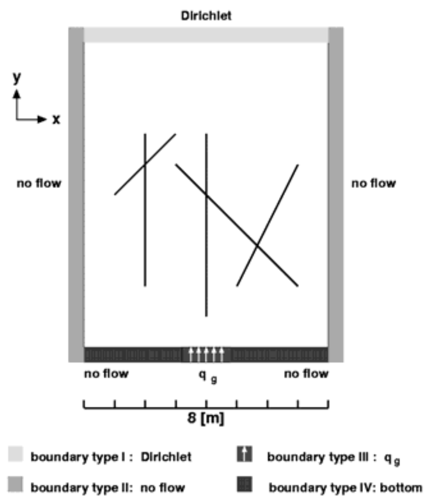

Figure 2.3-8: Schematic diagram for geometry and boundary condition for intrusion of gas into heterogeneous medium

- Boundary conditions

	water	gas	heat
No flow	$q_{wa} = 0.0$	$q_{ai} = 0.0$	$q_{he} = 0.0$
q_g	$q_{wa} = 0.0$	$q_{ai} = -0.01$; [kg m^{-2} s^{-1}]	$q_{he} = 0.0$
bottom	$q_{wa} = 0.0$	$q_{ai} = 0.0$	$T = (280 + T)$; [K]
Dirichlet	$S_w = 0.95$	$q_{ai} = 0.0$	$T = (280)$; [K]

- Initial values

hydrostatic pressure	$p_g\,(x,y) = (10200 + 10.0 - y) * 9810$ [Pa]
gas saturation	$S_g\,(x,y) = 0.95$
temperature	$T\,(x,y) = 280.0 + (10 - y) * (\Delta T / 10)$ [K]

- Material properties and constitutive relations parameters (Brooks-Corey)

	ϕ	k	S_w	S_{gr}	λ	p_d
Matrix	0.1	10^{-13}	0.2	0.0	2	2500
Fracture	0.3	10^{-8}	0.2	0.0	2	1000

The fracture width is 0.1 m; ΔT- the difference of temperature between the top boundary and the bottom boundary - was chosen as 0 [K], 10 [K], 100 [K].

The fluid properties are like the density function, the viscosity function and the functions describing the phase transfer are dependent on the primary variables pressure and heat. They are described in /HEL 00/.

The initial value for the water saturation is S_w = 0.95. This was necessary because the state of the 'water phase' is not yet defined and the lower capillary pressure in the fracture compared to the matrix leads to a water saturation of S_w = 1.0, if the initial water saturation is too high.

The gas infiltrates into the water-saturated domain and moves very fast inside the fractures as in However, the infiltration of gas into the matrix is also dependent on the temperature within the system. While the gas saturation Figure 2.3-9 is nearly identical for (top) and (middle), the gas migrates further into the matrix in Figure 2.3-9 (bottom).

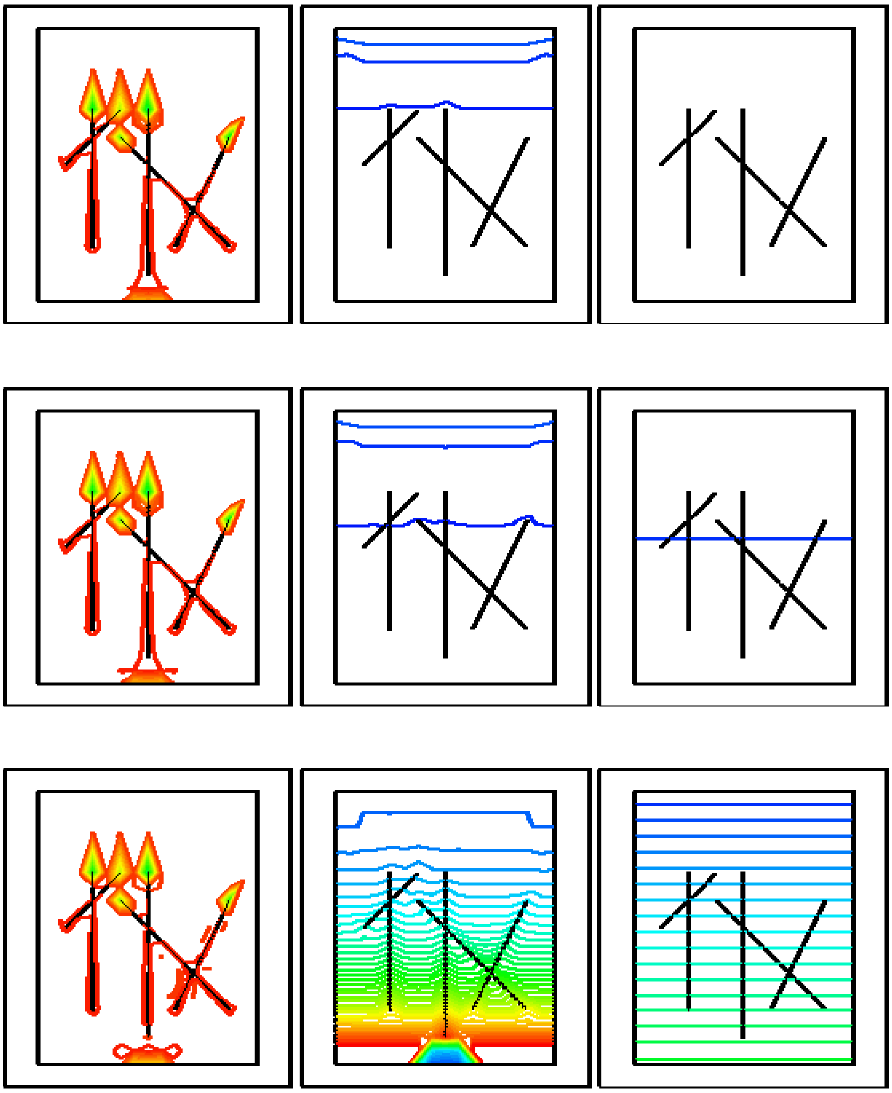

Figure 2.3-9: t = 40 s, S_w (left), T (middle), X_g^w (right), T = 280 [K] (top), T = 280 [K] (middle), T = 280 [K] (bottom) at the southern boundary

The main differences because of altered temperatures are the different mole fractions of water dissolved into the gas phase X_g^w. In Figure 2.3-9 it can be seen that significant parts of water are transported through the fractures as vapour within in gas phase.

2.3.2.2 Gas-Water Flow in Fractured Medium (3D)

This section presents results of a three dimensional simulation of gas-water flow in a fractured porous media. The matrix is a cube of 10 m by 10 m and contains one fracture which is diagonal to the $y-z$ plane. Figure 2.3-10 shows a sketch of the domain.

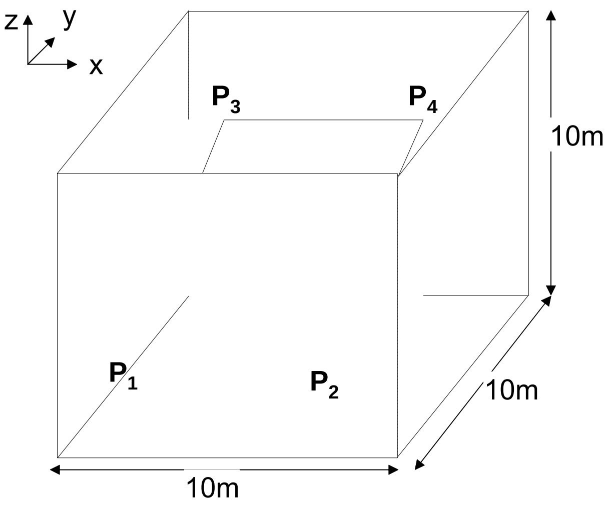

$$P_1 = (2.5[m], 2.5[m], 2.5[m])$$

$$P_2 = (7.5[m], 2.5[m], 2.5[m])$$

$$P_3 = (2.5[m], 7.5[m], 7.5[m])$$

$$P_4 = (7.5[m], 7.5[m], 7.5[m])$$

Figure 2.3-10: The domain for the 3D simulation.

The coarse grid consists of 18 elements and 16 vertices. A part of the coarse grid is shown in Figure 2.3-11, where the domain is cut in half along the plane in which the fracture lies. Each element is shrunk while its barycentre is kept fixed. The two triangular element sides that coincide with the fracture are coloured.

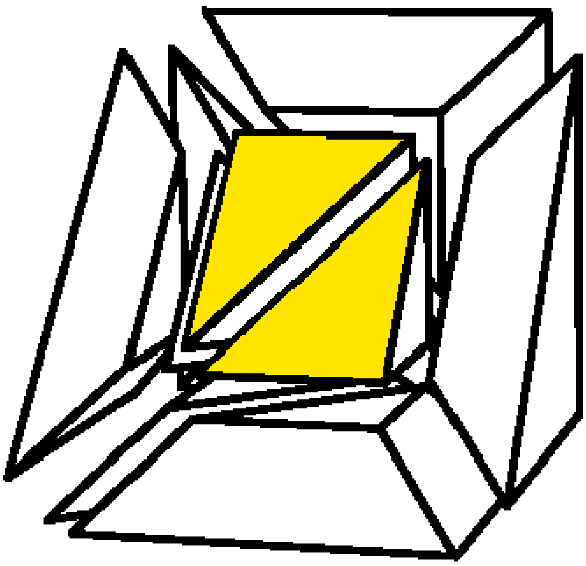

Figure 2.3-11: Some elements of the coarse grid. For visualisation each elements size has been reduced while keeping its barycentre fixed

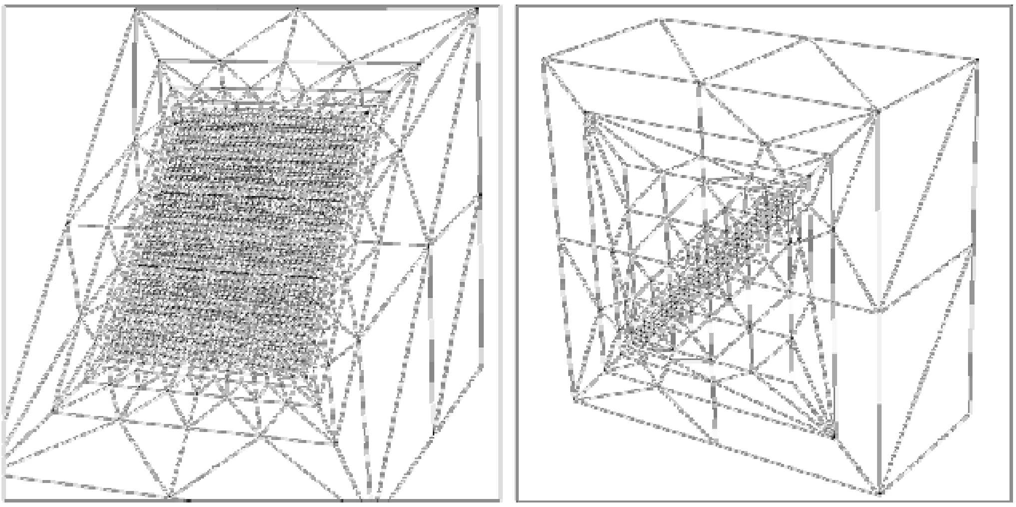

Figure 2.3-12: Grid for the three dimensional simulation. The grid is adaptively refined around the fracture

Figure 2.3-12 shows a grid that has been generated from the coarse grid by refining five times around the fractures. The rectangular fracture is clearly visible in this figure. For the simulation, one more refinement step is made: the final mesh then consists of 6 levels, 32845 nodes, and 180813 elements.

The simulation is done using the (p_w, S_n) -formulation which will be called (p_w, S_g) formulation here, since this is a water-gas example. The following parameters are used for describing hydrostatic boundary conditions and an initial saturation of $S_g = 0.4$ in a small part that covers fracture and matrix:

- Boundary conditions

North boundary	$q_w = q_g = 0.0$	
South boundary	$q_w = q_g = 0.0$	
Side boundaries	$p_w = (10 - z) * 9810$	[Pa]
	$q_g = 0.0$	

- Fluid properties

Fluid properties	Water;	Gas	
	$\rho_w = 1000;$	$\rho_w = \rho_g / 84149.6$	[kg m^{-3}]
	$\mu_w = 10^{-3}$;	$\mu_g = 1,65 * 10^{-5}$	[Pa s]

- Initial values

hydraulic pressure $p_w (x,y,z) = (10 - z) * 9810 ;$ [Pa]

$$S_g(x,y,z) = \begin{cases} 0.4 & 4 \le x \le 6; 2.5 \le \mathrm{y} \le 3.5; |(10 - \mathrm{y}) + z| \le 0.1 \\ 0.02 & \text{else} \end{cases}$$

- Material properties and constitutive relations parameters (Brooks-Corey)

	ϕ	k	S_w	S_{gr}	λ_d
Matrix	*0.2*	10^{-8}	*0.4*	*0.1*	*2 10000*
Fracture	*0.3*	10^{-6}	*0.1*	*0.05*	*2 1000.*

In the simulation an implicit EULER time-stepping scheme was used, a Newton method with numerical differentiation and line search for the solution of the non linear systems and Bi-CGStab with multi grid preconditioning for the solution of the linear systems. The prescribed reduction rate was 10^{-5} for the non linear and 10^{-4} for the linear solver, the maximal number of line searches in the Newton method was 6. The nodes on all grid hierarchies are ordered lexicographically. Full upwinding of mobility was employed. The smoother in the multi-grid method was ILU, with a damping parameter of 0.9.

Damping of the ILU smoother is used because the computation is done on a parallel computer the parallel multi-grid of UG generates a block Jacobi smoother like behaviour that makes damping desirable. For the computation, eight nodes of a cluster of workstations at the IWR Heidelberg are used, each equipped with a Pentium III Processor and 512MB RAM. Because the requirements of parallel computing have been taken into account during the whole development of the fracture model, it is possible to use parallel computing, as soon as the discretisation is finished, without further changes.

Saturation plots from the simulation with two cuts through the domain are shown in Figure 2.3-13. The scale for the saturation plot is $0 \le S_g \le 0.3$. It is clearly visible how the gas moves only inside the fracture, leaving a distinct trace behind it, due to the S_{gr} value. The cuts through the domain on the right show how the gas moves almost only in the fracture, even though a small amount of gas has been let into the matrix by the initial conditions.

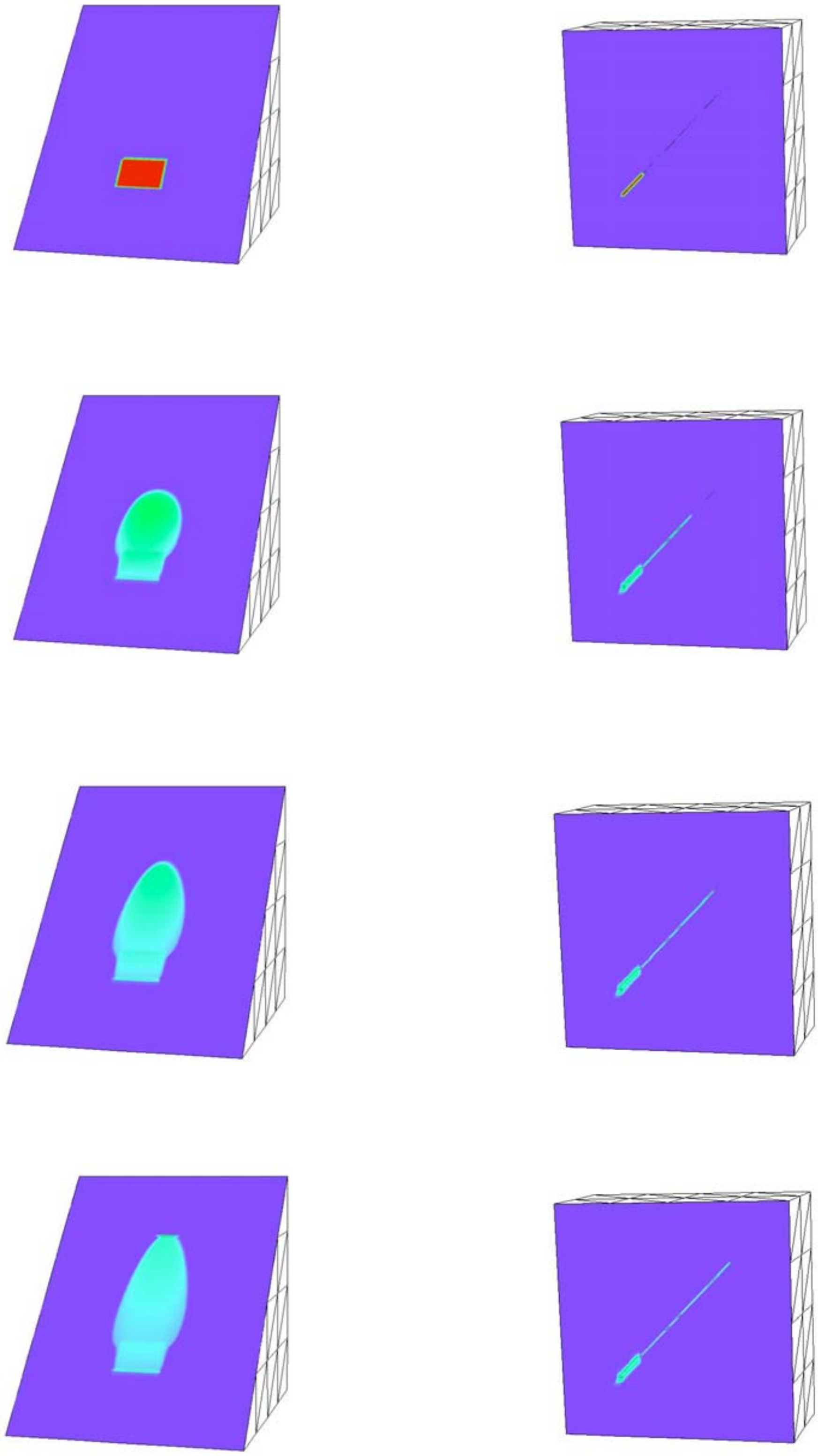

Figure 2.3-13: Saturation plots from 3D simulations

2.3.3 A Contribution to Upscaling of Gas-Water Flow in Single Fractures[1]

The strong influence of the rough surfaces of fractures on the permeability, and thus on the multiphase flow behaviour, has only been realised in the last years. The first experiments on the relative permeability-saturation relation in fractures were made by /ROM 66/. The results, which are based on the evaluation of two-phase flow (water-kerosene) in artificial fractures constructed of planar parallel plates, represent a linear correlation between relative permeability and saturation $k_{rw} = S_w$ and $k_{rg} = S_g$ for $0 \leq k_{r\alpha} \geq 1$ so that $k_{rw} + k_{rg} = 1$. The approach by /ROM 66/ is applied for a large number of models for the numerical simulation of fractured oil reservoirs /GIL 83/.

More recent studies of **naturally fractured rock** /PRU 90 and PER 91/ show that, the description of the relative permeability must also account for the roughness of the fracture walls, the fracture aperture, and the contact areas. The geo statistical model of /PRU 90/ assumes that both phases can only flow simultaneously, if the fracture apertures are correlated anisotropically. A survey of other approaches for the description of relative permeability-saturation relations in fractures can be found in /HEL 93/.

In /PRU 90/, the rough fractures are discretised as a field of parallel plates with different averaged apertures a_{ij} (Figure 2.3-14). So the permeability of each parallel fracture is given by $k = a^2 / 12$ as described in /MAR 86/.

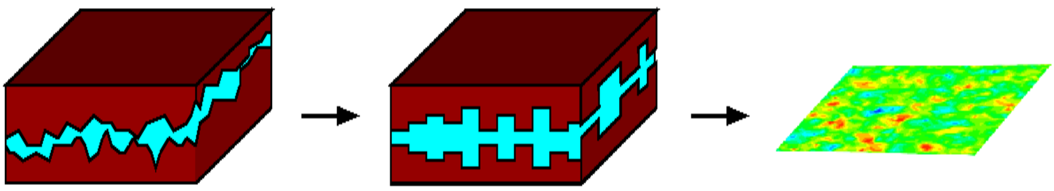

Figure 2.3-14: Approximation of rough fractures by parallel plates

As the fracture domain is normalised to a unit thickness the permeability of each averaged aperture is $k = a^2 / 12$.

[1]Acknowledgement: Basic ideas and data regarding the simulation of gas flow in single fractures were given by Jerker Jarsjö from the KTH Stockholm

The cut-off-aperture is defined by the capillary pressure given by the capillary pressure

$$p_c = \frac{2\sigma * cos(\alpha)}{a_c} \qquad \text{eq. 2.3-1}$$

with the surface tension σ The contact angle α is assumed to be zero.

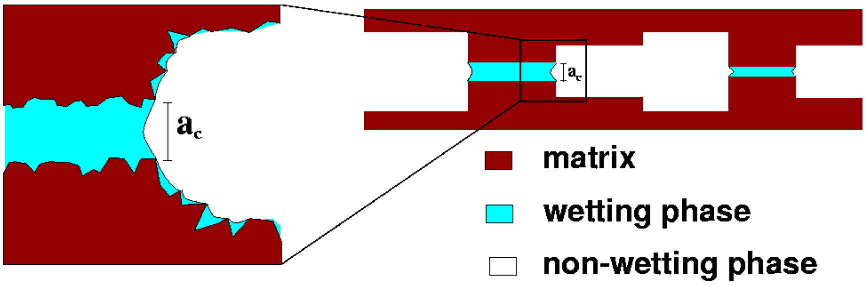

Figure 2.3-15: Definition of cut-off-aperture

In /PRU 90/, the water phase is assumed to cover all plates, the aperture of which is lower than the cut-off-aperture. The gas phase is assumed to cover all plates, the aperture of which is bigger than in /JAR 96/. This approach is referred to as the separation assumption (Figure 2.3-16).

To compute the constitutive relationships the saturation for a given cut-off-aperture must be computed. Therefore, we need the aperture distribution of a fracture. The aperture distribution used in this case was computed based on measured data given in /JAR 98/

$$f_{\ln}(a;\mu,\sigma) = \frac{1}{a\sigma\sqrt{2\pi}} exp\left[-\frac{1}{2\sigma_\alpha^2}(ln(a)-\mu_\alpha)^2\right] \qquad \text{eq. 2.3-2}$$

with the parameters μ_α = -3; σ_α = 0.8; a = 0.05 [mm]. The capillary pressure for a cut-off-aperture is given in /BAS 00/. The relative permeability for the wetting phase was computed via the relative transmissivity

$$Ts(a_c) = \frac{\int_0^{ac} a^3 \cdot f\ln(a)da}{\int_0^{\infty} a^3 \cdot f\ln(a)da \cdot} \qquad \text{eq. 2.3-3}$$

The relative permeability for the gas phase was computed via using the separation assumption

$$phase_s = \left\{ \frac{a < a_c \rightarrow w}{a \geq a_c \rightarrow g} \right\} \qquad \text{eq. 2.3-4}$$

The saturation is computed by

$$S_w = \frac{\int_0^{ac} a^3 \cdot f \ln(a) da}{\int_0^{\infty} a^3 \cdot f \ln(a) da} \qquad \text{eq. 2.3-5}$$

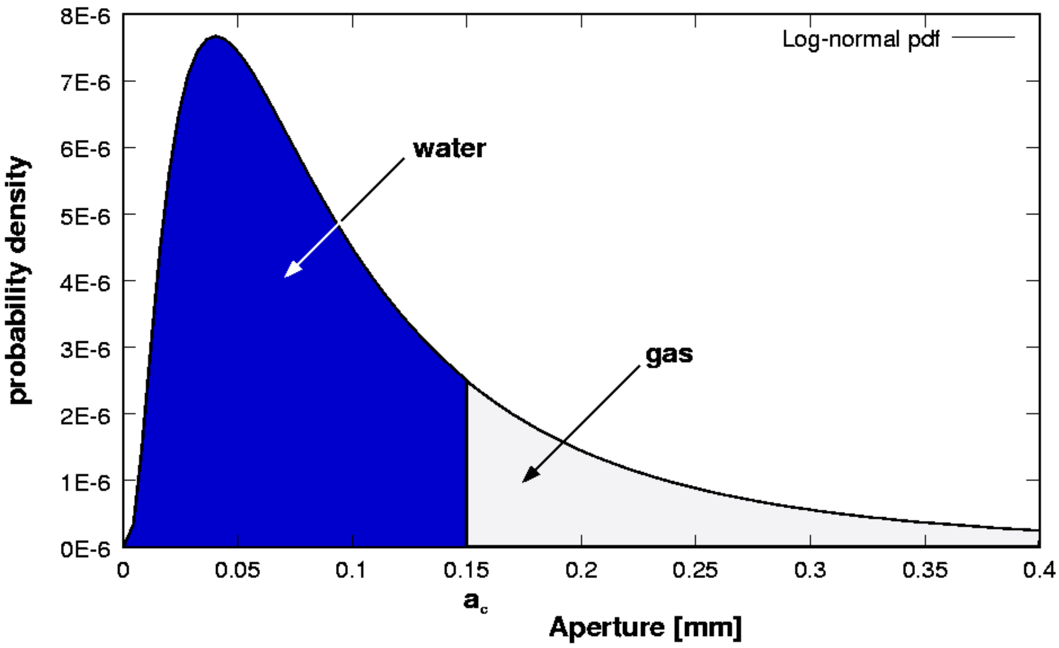

Figure 2.3-16: Computation of saturation with separation assumption

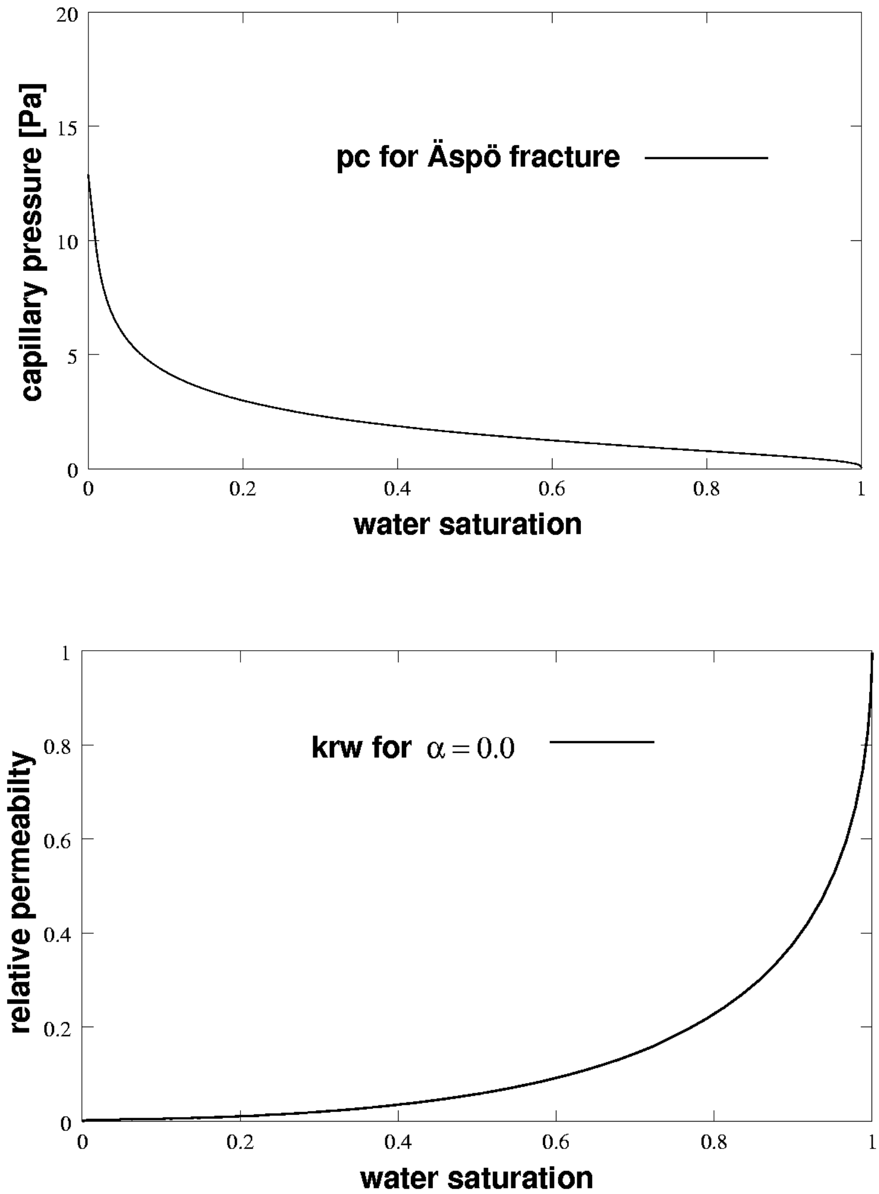

Figure 2.3-17: Capillary pressure saturation function (upper) and relative permeability saturation function (lower) using the separation assumption

Thus the functions for the constitutive relationships follow as given in Figure 2.3-17. Observe the very steep gradient of the relative permeability - saturation function at $S_w \approx 1$. At this point, even little changes in saturation do have a big influence on hydraulic conditions within the fractures.

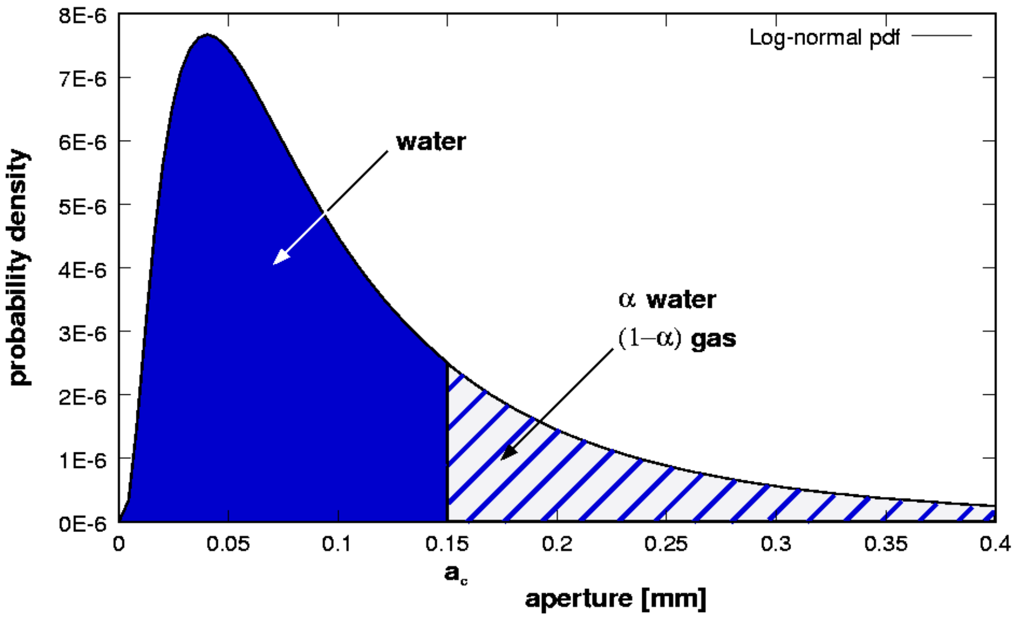

Figure 2.3-18: Computation of saturation with mixed assumption

In /JAR 98/ there is a new aperture distribution based model formulated. This model assumed that a fraction of the plates with $S_w \approx 1$ is still covered with the water phase. This fraction is given by the factor α. They refer to this assumption as mix assumption. Using the mix assumption, /JAR 96/ achieved better results for the relative transmissibility and the gas saturations, when they compared the results of laboratory observations of a degassing experiment published in /JAR 96/ with the predictions based on the different assumptions.

Using the mix assumption

$$phase_s = \left\{ \frac{a < a_c \rightarrow w}{a \geq a_c \rightarrow \alpha w + (1-\alpha)g} \right\} \qquad \text{eq. 2.3-6}$$

the saturation for a given cut-off-aperture is computed by

$$S_w = \frac{\int_0^{ac} a \cdot f \ln(a) da + \alpha \int_{ac}^{\infty} a \cdot f \ln(a) da}{\int_0^{\infty} a \cdot f \ln(a) da} . \qquad \text{eq. 2.3-7}$$

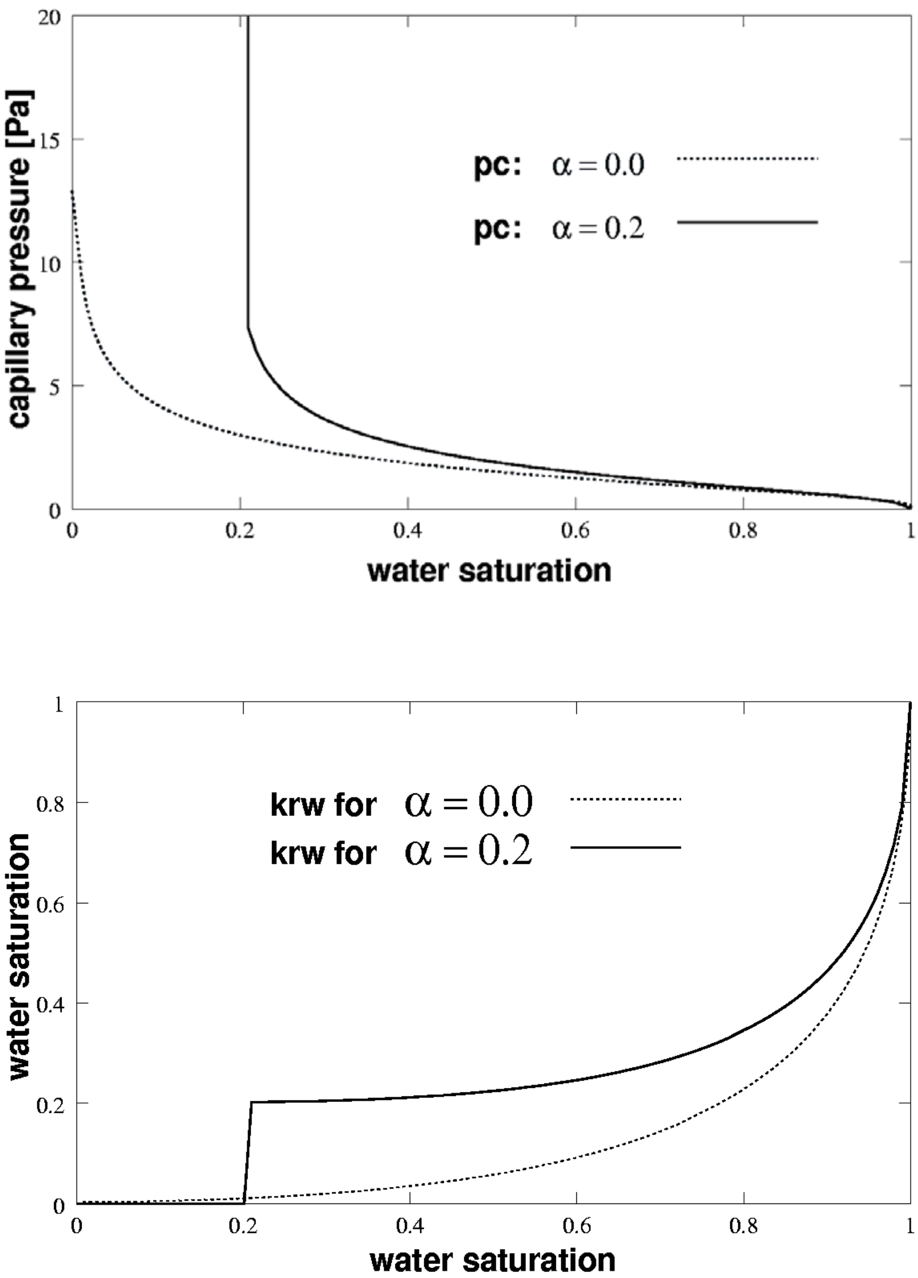

Figure 2.3-19: Comparison of capillary pressure saturation function (upper) and relative permeability saturation function (lower) based on separation assumption (blue) and mixed assumption (red)

Thus different constitutive relationships follow. In /JAR 98/ the best approximation for the mix assumption is given by $\alpha = 0.2$, which results in a residual saturation for the water phase of $S_{wr} = 0.2$. However, the steep gradient remains in these constitutive relationships.

Based on the data published in /JAR 96/, different permeability fields were generated with the geo statistical tool SIMSET (Prof. A. BARDÒSSY, Institute for Hydraulic Engineering, Stuttgart University). SIMSET uses the turning band method as basic approach to generate geo statistical data.

The best approximation with the measured aperture distribution given in /JAR 96/ was accomplished with an exponential variogram superposed with a nugget effect. Assuming the parallel plate model a permeability field was generated using the relationship $k = a^2 / 12$ for a two dimensional area with the length in x- and y-direction of 1 m (Figure 2.3-20).

In following table the input parameters describing the exponential variogram with superposed nugget effect are given. These parameters are estimated based on the pictures published in /JAR 96/.

Table 2.3-1: Input parameters

Average permeability (log representation)		Log (K) = -9.0 [mm]
Variance	Proportion nugget effect	0.01
	Proportion exponential variogram	0.30
Correlation length		0.04 [m]
Isotropic / non isotropic		isotropic

The average permeability $log\ (K) = -9.0$ [mm] corresponds to an average aperture of $\bar{a} = 0.11$ [mm].

This does not match with the parameters used for the computation of the constitutive relationships. Here the best approximation for the measured aperture distribution is an average aperture of $\bar{a} = 0.0087$ [mm]. However, the aim of these computations was to compare the influence of the two different assumptions qualitatively. Quantitative statements are not possible, as experimental results at the moment are lacking.

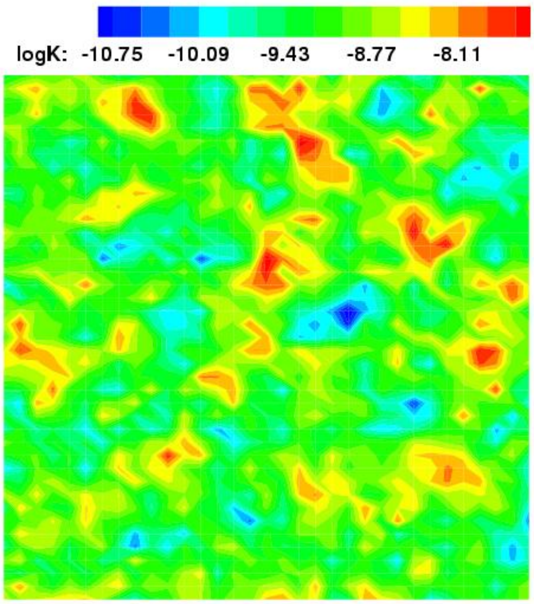

Figure 2.3-20: Permeability field based on stochastically generated aperture distribution

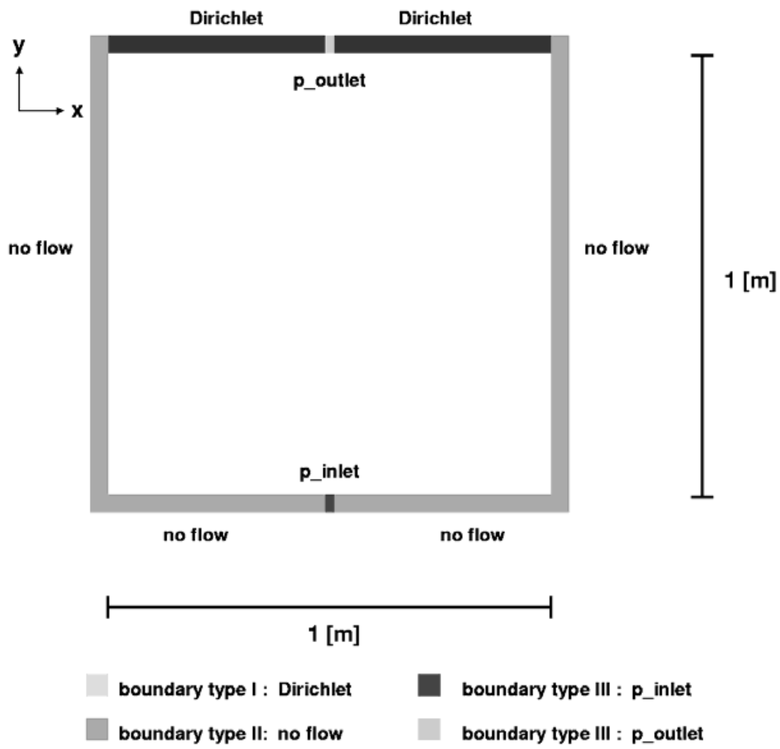

Figure 2.3-21: Boundary conditions for numerical simulation of gas infiltration

Based on the generated permeability field the entering of a gas phase at the bottom of the domain was simulated. The length of the inlet and of the outlet was given by 0.02 m. The boundary conditions can be seen in Figure 2.3-21. The porosity was set to $\phi = 0.4$. Both the boundary conditions and the porosity were chosen arbitrarily. The capillary pressure was upscaled for each plate via the LEVERETT condition /LEV 41/.

$$p_c^{elem} = p_c^{avg} \sqrt{\frac{K^{avg}}{K^{elem}}}) \quad . \qquad \text{eq. 2.3-8}$$

For the relative permeability function no upscaling concept was established.

The following initial values, phase properties and boundary conditions were used for the (p_g, S_w) –formulation:

- Initial values

hydrostatic pressure	$p_g (x,y) = (1 - y) * 9810 ;$ [Pa]	
gas saturation	$S_g (x,y) = 0.9999$	

- Phase properties

	water	gas
	$\rho_w = 1000;$ [kg m^{-3}]	$\rho_g = \rho_g / 841496;$ [kg m^{-3}]
	$\mu_w = 10^{-3};$ [Pa]	$\mu_g = 1.65 * 10^{-5};$ [kg m^{-3}]

- Boundary conditions

	water	gas
No flow	$q_{wa} = 0.0$	$q_{ai} = 0.0$
Dirichlet	$S_w = 0.9999$	$p_g = 10000;$ [Pa]
P inlet	$q_w = 0.0$	$p_g = 30210;$ [Pa]
P outlet	$q_w = 0.0$	$p_g = 200;$ [Pa].

For both assumptions the main flow paths are given by the areas of high permeability which are slightly connected. The gas velocities shown in Figure 2.3-22 do not differ much, as do not the results for the effective permeability (Figure 2.3-25) or the pressure field (Figure 2.3-24). The most relevant differences occur in the saturations (Figure 2.3-23). The simulation using the constitutive relationships based on the mix assumption result in a wider spreading of the gas phase and in higher gradients for the gas phase. In Figure 2.3-26, the influence of the main flow paths is shown. The gas (dark colour) migrates through those regions of higher effective permeability.

Figure 2.3-22: Velocities for relationships based on separation assumption (left) and mix assumption (right) at t = 3.5 [s]

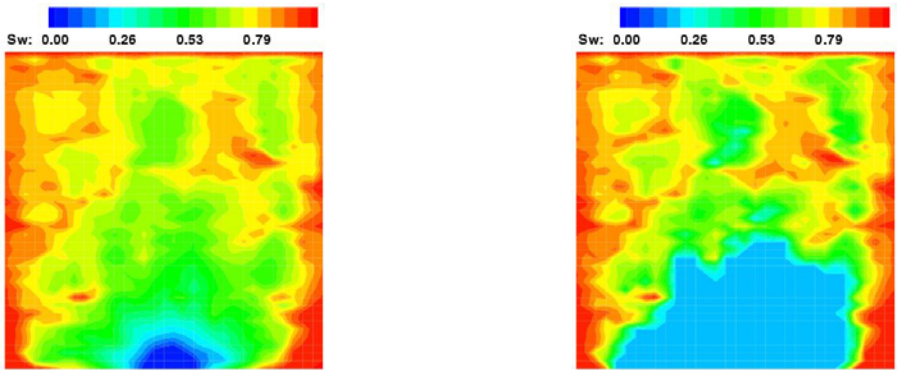

Figure 2.3-23: Water saturation for relationships based on separation assumption (left) and mix assumption (right) at t = 3.5 [s]

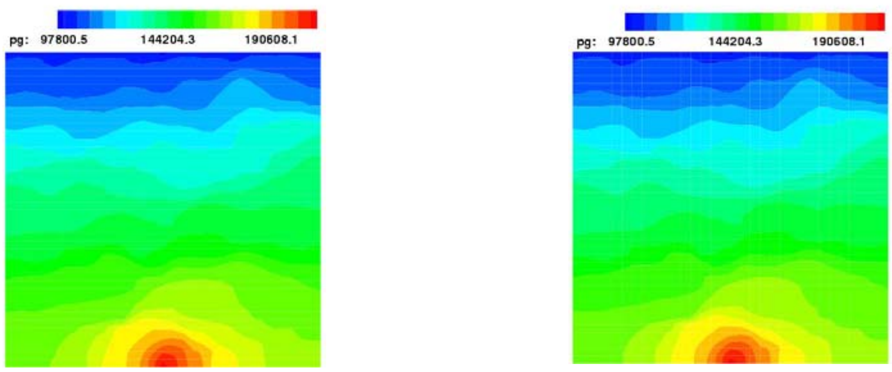

Figure 2.3-24: Gas pressure for relationships based on separation assumption (left) and mix assumption (right) at t = 3.5 [s]

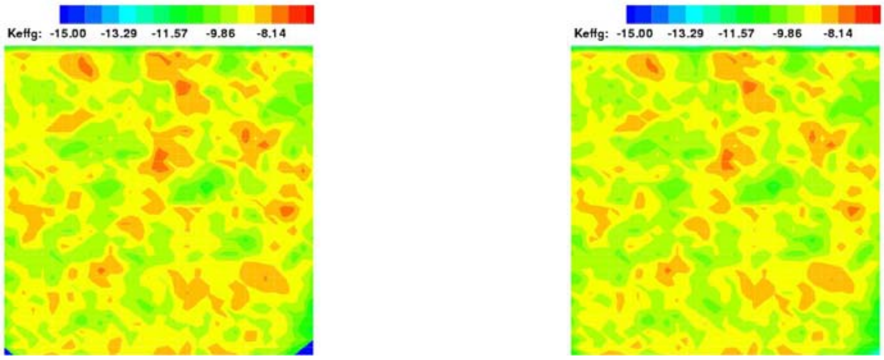

Figure 2.3-25: Effective permeability relationships based on separation assumption (left) and mix assumption (right) at t = 3.5 [s]

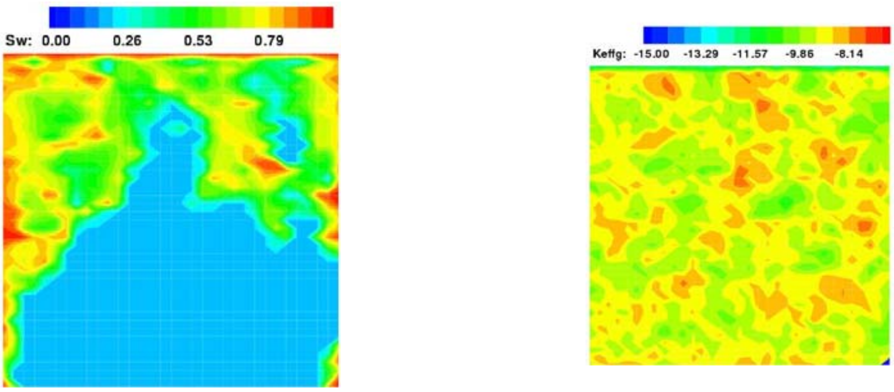

Figure 2.3-26: Water saturation and filtered effective permeability for mix assumption at t = 6.5 [s]

2.3.4 Summary and Remarks on Advanced Modelling

Within section 2.3, a model for two-phase-flow processes for fractured porous media has been presented. The fractures have been implemented as one-dimensional lines for the two-dimensional space or as two-dimensional planes for the three-dimensional space respectively.

It got clear that due to the choice of primary variables ((p_w, S_g), (p_g, S_w, T); respectively) and the implementation of fractures as hyper planes the entering of gas from the fracture into the matrix system had to be considered carefully. Therefore the **P**hase

Pressure **S**aturation **I**nterface **C**ondition (*PPSIC*) has been established for the fracture formulation. On this basis both a two phase model and a two-phase two-component model have been implemented.

Furthermore first approaches have been presented to get effective parameters which are necessary for a reasonable simulation of two-phase-flow processes in fracture matrix systems.

First, the fracture generator developed by Annette Hemminger /HEM 99/ was integrated into MUFTE_UG so that reasonable stochastic or deterministic fracture fields could be included into the simulation process.

Second, in cooperation with Jerker Jarsjö from the **WRE**, KTH Stockholm, first steps for a new upscaling concept for two-phase flow in a single fracture were taken.

As both approaches seem to be very promising it would be highly desirable to do more research work within these fields and even to combine them: The fracture generator should be extended, so that aperture fields for three dimensional fracture systems could be considered. The upscaling approach should consider - besides gas water flow processes - gas water solution processes with regard to fracture matrix systems.

Section 2.3 makes clear that the use of advanced numerical methods on high performance computers has been established for the simulation of gas water flow and transport processes. This approach now allows the implementation of geo statistic data fields in two and three dimensions to identify uncertainties with e.g. Monte Carlo methods.

3 Geoelectric Monitoring for Determining Local and Regional Changes of Water Saturation

Ulrich Zimmer

In the area of the ZEDEX- and the DEMO-Tunnel the applicability of geoelectric monitoring for determining local and regional changes of water saturation in the granite rock were tested. Within geoelectric profile measurements the local characteristics (e.g. tunnel surface, EDZ, backfilled area) were examined. Data from tomographic measurements were used to model the saturation distribution in larger areas. In preparation for the in-situ application the correlation of water saturation and electric resistivity was determined in the laboratory using core samples.

3.1 Correlation between Electric Resistivity and Water Saturation on Granite Samples

The basis for all the geoelectric in-situ measurements is the knowledge of the relation between water content of the rock and its electric resistivity. For a quantitative determination of this relation six samples of Äspö granite from the area of interest were saturated with original formation water. Then the electric resistivity was measured. For a full (100 %) saturation of the granite which implies a water content of app. 0.5 Vol. %, a resistivity of 1000 Ωm was measured. Afterwards, the samples were dried to decrease the saturation. Due to the lower water content the resistivity increased.

The electric resistivity of the samples was measured by applying a known voltage to the planes of the sample and measuring the resulting current. To achieve a good coupling between the metal plates and the sample, the planes of the sample were coated by highly conductive silver paint. The three samples which were measured with silver-coated planes show less scattering of the values compared to the samples without a silver-coating (Figure 3.1-1).

A mathematical description of the resistivity / water content relation is Archie's law (equations eq. 3.1-1 and eq. 3.1-2).

$$\rho = \rho_w \cdot (\phi \cdot S)^{-m} \qquad \text{eq. 3.1-1}$$

$$\rho = \rho_w \cdot \phi^{-m\cdot} \cdot S^{-n} \qquad \text{eq. 3.1-2}$$

In these equations ρ is the total resistivity of the rock, ρ_W the resistivity of the water, ϕ the porosity, S the saturation, m the so called cementation factor, and n the saturation exponent. With this law the determined values can be fitted by an exponential curve. From this curve the constants in Archie's law can be specified.

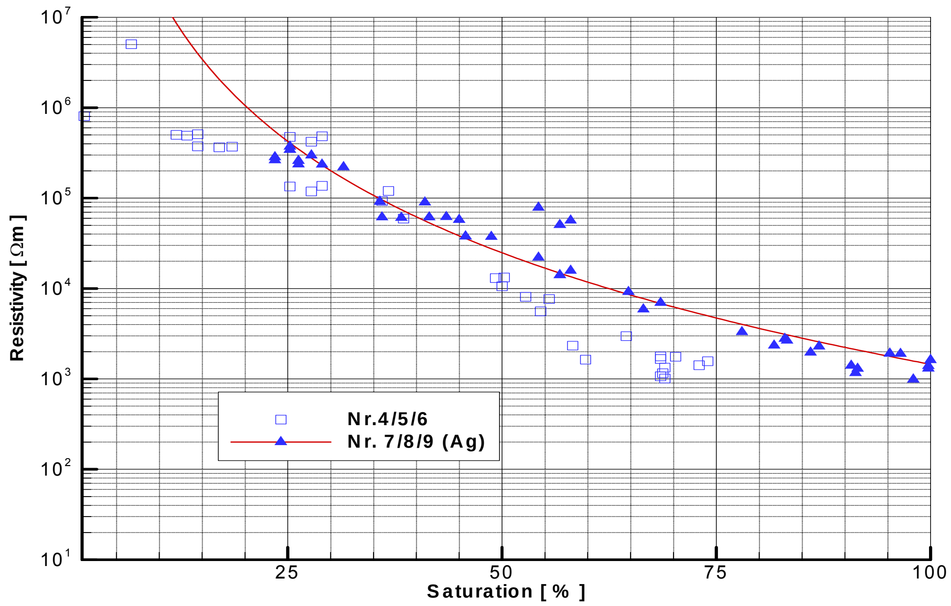

Figure 3.1-1: Correlation between resistivity and saturation on granite samples from HRL Äspö

3.2 Geoelectric Measuring Methods

It was shown on laboratory samples that a close relationship between resistivity and water content exists in the Äspö granite. With this relation the water content in situ can be estimated on basis of measured resistivity. Besides the saturation, the relation contains explicitly the water resistivity and the porosity of the rock. The empiric exponents, the cementation factor and the saturation exponent, depend on the pore distribution and geometry of the pores. During geoelectric monitoring, the geometric rock conditions can be assumed as constant. Nevertheless, the in-situ rock might show different parameter values than the laboratory samples. Especially at Äspö the granite contains many fractures which can easily be observed by water leakages into the tunnel. In contrast to that, the laboratory samples contained no fractures and were assumed to represent the intact matrix material of the in-situ site. The differences between the in-situ rock conditions and the laboratory sample cause quantitative uncertainties for the in-situ interpretation (section 3.3). The two basic geoelectric in-situ resistivity methods applying direct current (DC) are measurements along a profile (mapping) and around an area (tomographic method).

3.2.1 Mapping along Profiles

Probably the most popular code for the inversion of geoelectric resistivity measurements at the moment (Dec. 1999) is the Res2Dinv-algorithm from Loke and Barker, (1995). This code can be applied for the standard 2-dimensional inversion of measurements along an electrode profile. Topographic effects on the profiles can be calculated. The code does not require any additional information of the underground. On the other hand, it is not possible to include any a-priori information, e.g., known water-bearing fractures, into the resistivity model of the underground.

The inversion code is designed to invert large data sets collected with a system controlling a large number of electrodes. The 2D-model used by the inversion code consists of a number of rectangular blocks. The arrangement of the blocks is loosely coupled to the distribution of the data points in the pseudo section. The distribution and size of the blocks is automatically generated by the code so that the number of blocks does not exceed the number of data points. The depth of the bottom row of blocks is set to be approximately equal to the equivalent depth of investigation of the data points with the largest electrode spacing. The data must be collected from electrodes arranged in a line with a constant spacing between adjacent electrodes A finite-difference forward modelling subroutine is used to calculate the apparent resistivity values, and a non-linear least-squares optimisation technique is used for the inversion routine. The code can be used for surveys using the Wenner, pole-pole, dipole-dipole, and pole-dipole arrays.

The inversion routine used by the code is based on the smoothness-constrained least-squares method for 2D apparent resistivity data. For this code, a new implementation of the least-squares method based on a quasi-Newton optimisation technique is used.

This technique is more than 10 times faster than the conventional least-squares method for large data sets and requires much less memory. One advantage of the method is that the algorithm can be adjusted to suit different types of data by choosing a damping factor and flatness filters. The 2D model used by this code divides the subsurface into a number of rectangular blocks. The purpose of the code is to determine the resistivity of the rectangular blocks that will produce an apparent resistivity pseudo section that agrees with the actual measurements. For the Wenner array, the thickness of the first layer of blocks is set to 0.5 times the electrode spacing. The thickness of each subsequent layer is increased by 10 % (or 25 %). The optimisation method basically tries to reduce the difference between the calculated and measured apparent resistivity values by adjusting the resistivity of the model blocks. A measure of this difference is given by the root-mean-squared (RMS) error. However, the model with the lowest possible RMS error can sometimes show large and unrealistic variations in the model resistivity values and might not always be the "best" model from a petrological perspective. In general, the most prudent approach is to choose the model at the iteration after which the RMS error does not change significantly. This usually occurs between the 3rd and the 5th iteration.

It should be noted that a basic limitation of the RES2DINV program is the assumption of a 2D subsurface model. For surveys carried out across the strike of elongated geological structures, this assumption is reasonable accurate. However, if there are significant variations in the subsurface resistivity in a direction perpendicular to the survey line, this could cause distortions in the lower sections of the model obtained. Measurements made with larger electrode spacing are not only affected by the deeper sections of the subsurface, they are also affected by structures at a larger horizontal distance from the survey line. This effect is most pronounced when the survey line is placed underground or near a steep contact with the line parallel to the contact.

3.2.2 Tomographic Inversion

In general tomography is a method for the calculation of cross-sections of an inaccessible structure from measurements on its boundary. The objective of the geoelectrical resistivity tomography is the computation of the resistivity distribution in the inner part of a rock area surrounded by electrodes. By setting a known voltage between two points (A, B) potential fields are induced into the rock. The geometry of these electric fields depends on the resistivity distribution in the rock. By measuring the voltage between two other points (M, N) along an electrode line on the rock surface the potential field is measured. From many of such single measurements with different electrical fields the resistivity distribution in the inner part of the rock can be calculated. Since the electric fields are measured only along the surface of the rock, the calculated result shows uncertainties. They can be minimised by surrounding the area of interest completely with measurement points (electrodes) and by optimising the measurement configurations.

Usually the investigated objects show a 3-dimensional resistivity distribution. In September 1999 the only available commercial software for the calculation of resistivity tomograms was the RESITOMO-software package which allows only a 2-dimensional inversion of the measured apparent resistivity data. Although some 3-dimensional algorithms are under development from different working groups a 3-dimensional software will only available at the end of 1999. The RESITOMO-software applies a **m**ultiplicative **s**imultaneous **i**nversion **r**econstruction **t**echnique (MSIRT) which is slightly modified for the resistivity inversion.

3.3 In-situ Results

The resistivity measurements on samples with known water content proved the applicability of the resistivity method for Äspö granite in situ. A difference between the rock in situ and the laboratory samples are water-bearing fracture systems, which are included in situ. The laboratory samples consist only of a homogeneous porous matrix without any larger fractured areas. For the interpretation, the laboratory samples can be regarded as homogeneous, whereas the in-situ area shows lateral variations of its petrological properties. Since these water-bearing fracture zones show a high resistivity contrast to the intact rock, but are confined to a very small area, this will cause numerical problems during the inversion process, which requires special treatment.

3.3.1 Electrode Array between ZEDEX- and DEMO-Tunnel

For the determination of the resistivity and the water distribution between the ZEDEX- and the Demo-tunnel a total of 299 electrodes were installed (Figure 3.3-1). Most of the electrodes were arranged on four profiles at the walls, the rest of them in a borehole to cover the fourth side of the area, which is very important for the evaluation of the tomographic measurements.

The surface electrodes consist of 5 cm long steel pins which are cemented in a 3 cm deep borehole, 50 cm apart from each other. At least, 111 electrodes were installed in the ZEDEX-drift, 42 and 10 electrodes in the access tunnel, and 100 electrodes in the demo tunnel. Since the diameter of the borehole is only sufficient for a limited number of cables, the spacing for the borehole electrodes is 1 m. All these electrodes were connected to the automatic recording unit in a container at the end of the demo tunnel with a single cable. The recording unit can be controlled by a telephone line from Braunschweig. The data are transferred by this telephone connection, too. This allows a high density of measurements. Although one reading lasts only 15 seconds, up to 8 hours of measuring are necessary to get a complete pseudo section of the ZEDEX- or the Demo-tunnel. After some test measurements the input voltage was set to 50 V for all measurements.

In 1998, another array of 60 electrodes was installed in the deepest part of the ZEDEX-tunnel to investigate the possibility of monitoring the water uptake in the backfill material. After backfilling, the drift was sealed by a plug in November 1999. Following a draining period, the saturation of the backfill was planned to be started in early 2000.

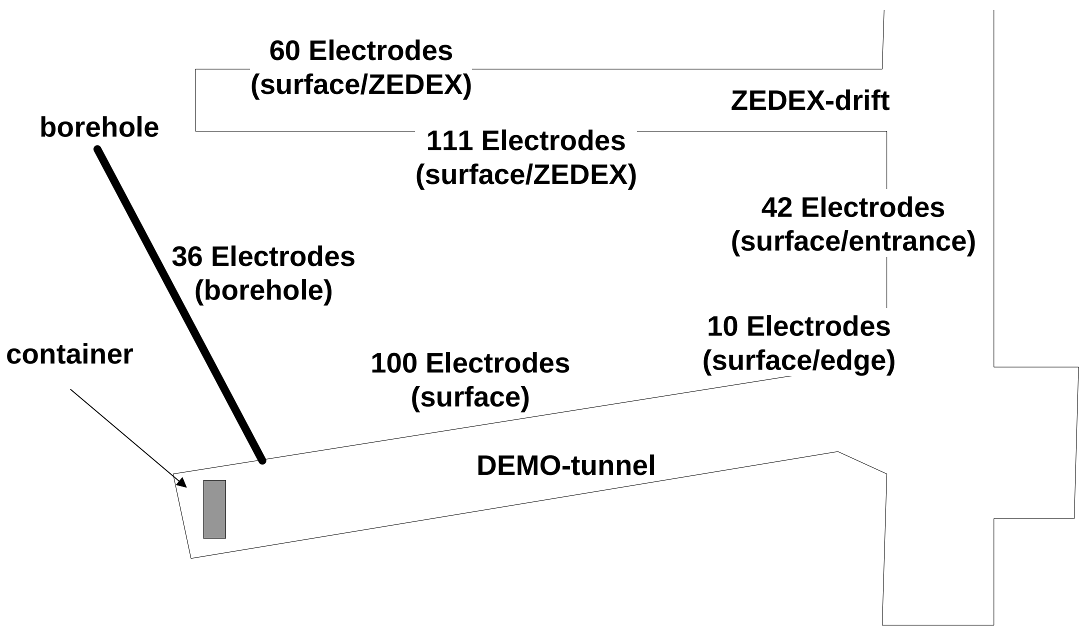

Figure 3.3-1: Distribution of electrodes around the Demo- and the ZEDEX-tunnel

3.3.2 Excavation Disturbed Zone around Tunnels

One of the major objectives of the geoelectric measurements was the determination and monitoring of the excavation disturbed zone around the different tunnels. The electrode spacing of 0.5 m allows a lateral resolution of app. 0.25 m and a depth dependent resolution of app. 0.2 m. With increasing depth of the model the resolution in resistivity decreases. During the measurements no additional excavations were conducted in the area. Nevertheless, the ZEDEX- and the DEMO-tunnel were the focus of numerous activities. In the ZEDEX-tunnel a backfill experiment was prepared. In this experiment nearly the whole tunnel was back filled with gravel or gravel / clay mixtures. In the DEMO-tunnel a demonstration site was prepared to show the deposition of waste canisters in boreholes. During the recording of the electric resistivity the floor in the tunnel was paved and the walls were covered with concrete to prevent water leakages into the tunnel. Also the drilling of boreholes in more distant parts of the mine could change the resistivity distribution in the ZEDEX- and DEMO-tunnel area. The rock at Äspö contains many fractures which can be regarded as hydraulically connected. Water leakages in distant parts of the mine might cause decreases in the pore pressure in the investigated area. Such effects are quite common and well known at Äspö.

3.3.2.1 Topographic Effects

The ZEDEX- and DEMO-tunnel were excavated by the drill and blast technique, which creates rough surfaces. Due to breakouts the undulation along the profiles can be several decimetres. In correlation with the electrode spacing of 0.5 m, the distortion of the electric field caused by the topography along the profile had to be considered. At least in the very near vicinity of the surface, these topographic effects might have an influence on the computed resistivity values.

To consider the topographic effects, the exact positions of the electrodes were required. They were provided by the survey department of the Äspö HRL. A two-dimensional projection of these co-ordinates is shown in Figure 3.3-2. Although the topography is in the magnitude of the electrode spacing, the undulations are small compared to the whole extension of the array.

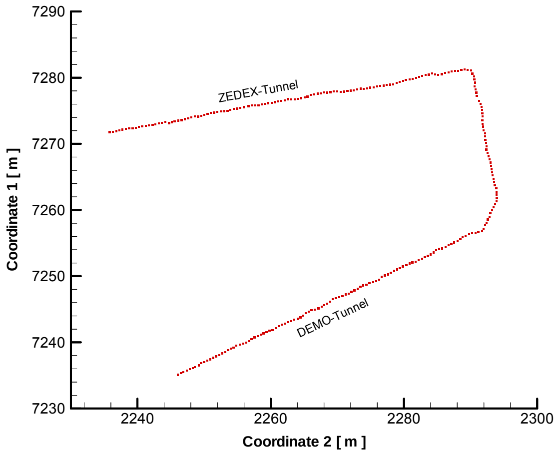

Figure 3.3-2: Two-dimensional projection of (surface) electrode co-ordinates

To check the quantitative influence of the topography on the inverted numerical values, a data set was inverted with and without the topographic correction. The results are shown in Figure 3.3-3. Although the topography is clearly visible, the differences in the resistivity distributions are rather small and do not change the general interpretation of the section. According to these results it appeared not absolutely necessary to consider the topography along the tunnels.

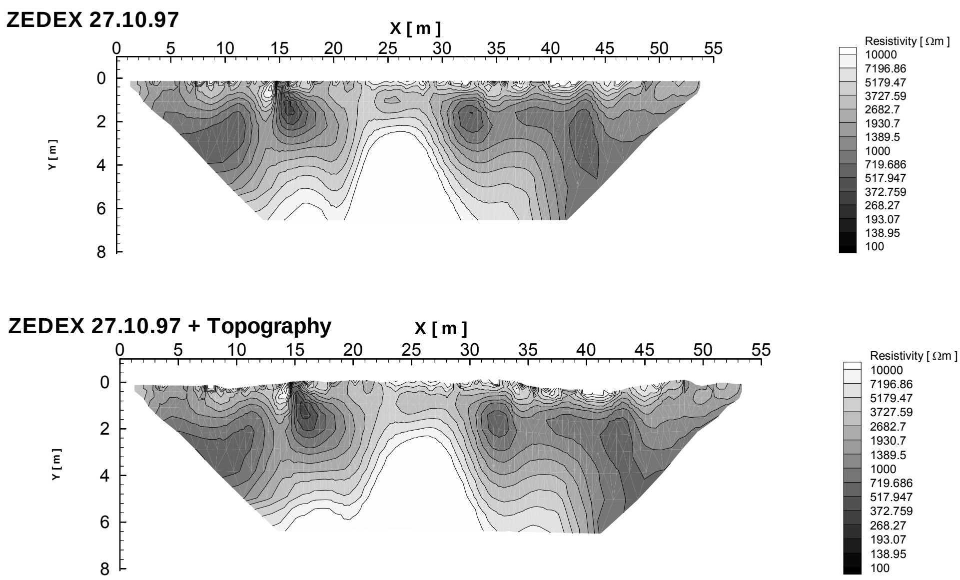

Figure 3.3-3: The influence of the topography along the ZEDEX-tunnel profile on the inverted resistivity distribution

3.3.2.2 ZEDEX-Tunnel

The ZEDEX-tunnel was monitored from mid of 1997 to March 1998 (see appendix A). The initial resistivity distribution shows small anomalies of high resistivity near the surface up to a depth of app. 1 m. These anomalies are interpreted as the effect of the excavation disturbed zone (EDZ). Deeper parts of the rock show resistivities around 1000 Ωm which correlates well with the resistivities obtained on full saturated laboratory samples.

Below profile metre 22 the resistivity shows unusually high values around 10000 Ωm. If this resistivity was interpreted in terms of water content it would imply a saturation of only 50 % or less. Another possibility could be a decrease in porosity, but in this case the resistivity in this part would remain at that high value at all times. From February to March 1998, however, this high resistivity anomaly vanished and the value decreased to a normal level around 1000 Ωm. For this reason it can be assumed that the anomaly is caused by the water distribution in the rock. Since, however, a low saturated zone in a full saturated environment would be hard to explain the anomaly had to have different reasons than water saturation or low porosity.

It is known from the geological mapping in this area that small water-bearing fracture zones exist in the Äspö granite. From model calculations it can be taken that thin highly conductive resistivity anomalies are hard to reconstruct by the inversion software. If the original anomaly is smaller than the resolution of the computed resistivity model, artificial numerical anomalies may be computed by the inversion software. Especially, thin zones with low resistivity as it is assumed for water-bearing fractures in the ZEDEX tunnel can cause high resistivity anomalies in the deeper parts of the model. Therefore, this resistivity distribution indicates that most of the water is concentrated in the fractures.

From February to March 1998, the high resistivity anomalies vanished and the average resistivity decreased to app. 700 Ωm. Low resistivity anomalies up to profile metre 10 and around profile metre 40 indicate positions of water-bearing fractures. This resistivity distribution indicates a homogenisation of the water distribution. In contrast to February 1998, the water is not confined to small areas, but is spread over a larger area. Another indication for the change in the rock’s properties is the resistivity distribution near the surface. The small high-resistivity anomalies diminished nearly completely, which also shows homogenisation of the rock. Since granite does not show any creep behaviour, the excavation disturbed zone still exists, but its moisture content changed.

Since the planned backfill experiment in the tunnel required extensive drilling, the ZEDEX-profile had to be abandoned in March 1998.

3.3.2.3 Demo-Tunnel

In contrast to the ZEDEX-tunnel, the Demo-tunnel was monitored for more than two years. Although many more data sets were recorded for a better overview, only one data set of each month is shown in Appendix B. Until August 1998, the resistivity distribution in the Demo-tunnel remained nearly constant. Small anomalies of high resistivity indicate the effect of the excavation disturbed zone. According to the measurements this zone extends less than 0.5 m into the rock. The average resistivity of the rock is about 600 Ωm which is on log-scale slightly less than the value for full saturated granite obtained on laboratory samples of 1000 Ωm (see section 3.1). In contrast to the ZEDEX-tunnel at the same time, the DEMO-tunnel shows a smooth resistivity distribution. Nevertheless, a high resistivity anomaly in the deeper part of the model around profile metre 25 is visible. This anomaly can also be explained by the artificial effect of a thin water-bearing fracture zone in this area. The anomaly vanished early in 1998, which agrees well with the results obtained on the ZEDEX-tunnel profile. From April 1998 to August 1998, the average resistivity increased slightly, but the overall resistivity distribution remained nearly constant.

From August to September 1998, the resistivity distribution changed completely. The resistivity image became more detailed and many small anomalies of high and low resistivity came up. Near the surface, numerous anomalies of high resistivity indicate the existence of the excavation disturbed zone. It seems that the fractures near the surface were desaturated for some reason. Another explanation might be the human activities in this area. During this time, the walls of the DEMO-tunnel were covered with concrete to prevent water leakages from the rock into the tunnel. This concrete might be the reason for the small anomalies with high resistivities. Since the water cannot escape easily into the tunnels, additional pore space which was desaturated before becomes saturated. This lowers the resistivity of the rock. The inverted resistivity is well below the value of fully saturated intact rock of 1000 Ωm. This could be explained by formation water with a lower resistivity than the water used in the laboratory experiments. Since the fracture system has a direct connection to the overlying Baltic Sea, a change in the water properties seems improbable. From geological mappings it was known that many fractures exist in this area. Before the tunnel wall was grouted with concrete, only the larger fractures were filled with water. After the grouting the pore pressure increased and smaller fractures were also filled with water. Therefore, the geoelectric measurements show the influence of the human activity on the saturation condition in the excavation disturbed zone. A proof for this theory could be provided by direct measurements of the pore pressure.

3.3.3 Regional Resistivity Distribution

During the early time of the project the area was nearly completely surrounded by electrodes. This allowed the computation of resistivity tomograms of the rock pillar between the ZEDEX- and the DEMO-tunnel until March 1998. Then the electrodes in the ZEDEX-tunnel had to be removed, because the installation for the Backfill-experiment started. Without electrodes on the fourth side of the area it was not possible to get a reliable resistivity image of the whole area.

All tomographic resistivity images from this area are included in Appendix C. To describe the most important results from these measurements the resistivity tomogram obtained on February 10, 1998 (Figure 3.3-4) is discussed as an example

The resistivity in this figure ranges from values below 100 Ωm (black) to above 1000 Ωm (white). According to the laboratory results, fully saturated granite in this area shows a resistivity value of app. 1000 Ωm. Assuming that the resistivity of the pore fluid does not change, values below 1000 Ωm indicate higher water content. To achieve higher in-situ water contents than full saturation on the laboratory samples, the porosity in situ has to increase. As a consequence resistivity values below 1000 Ωm indicate areas with higher porosity than the value measured on laboratory samples.

The interpretation of the tomograms is complicated by numerical uncertainties in the computed resistivities. The quality of the computed tomograms depends on the number of measurements and electrodes included in the inversion algorithm. The applied tomographic inversion software RESITOMO was only capable to handle 49 electrodes and up to 600 single measurements in the inversion process.

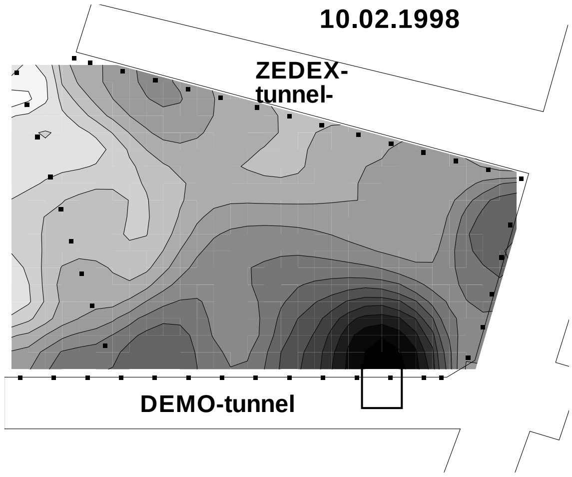

Figure 3.3-4: Tomographic resistivity distribution on February 10, 1998

To cover all sides of the area of interest the 49 electrodes were distributed equally in the tunnels. The spacing between the considered electrodes had to be increased up to 4 m. The resolution of the resistivity model also depends on the electrode spacing. With a spacing of 4 m; a spatial resolution of only 2 m by 2 m could be achieved. The area between the electrodes was divided into rectangular cells with 2 m side length. Each of these cells is attributed with a constant resistivity as described in section 3.2.2. Resistivity anomalies (smaller than this 2 x 2 m resolution) cannot be inverted by this model. Their influence distorts the reconstructed resistivity of cells in the vicinity.

Additionally to this averaging effect, a more serious effect can arise. It was shown on profile measurements that very thin anomalies of low resistivity can provoke numerical instabilities in the inversion algorithm. The very low resistivity of water-bearing fractures influences the measured resistivities, but due to their small extension they can not be reconstructed by the inversion algorithm. In this case the software tends to fill critical cells with unusual high resistivity values. This behaviour is caused by the implemented algorithm and can not be corrected. For this reason very high resistivities in these tomograms cannot be interpreted quantitatively in terms of water content.

Despite all the numerical difficulties from the inversion process, some important results can be obtained from the resistivity tomograms. Large areas of the inner parts of the tomogram show resistivities slightly higher than 1000 Ωm (C) which indicates full saturated granite. Single water-bearing fractures in this area are likely, but the model resolution is not sufficient due to the electrode spacing of 4 m. In the deeper parts of the borehole the inverted resistivity reaches its maximum value far above 1000 Ωm (B). This is a typical effect of a thin water-bearing fracture in this area. From the drilling of the borehole it was known that especially in this area a highly conductive fracture zone exists. A low resistivity anomaly at the surface of the DEMO-tunnel (A) and some smaller anomalies of low resistivity can be correlated with water-bearing fractures visible at the surface.

Although the determination of resistivity tomograms of such a large rock pillar was achieved, it was not possible to determine the exact positions and extensions of water-bearing fractures in this area or to proof their connectivity with these measurements. Software which allows including more than 49 electrodes and more than 600 single measurements would improve the results, but the resolution of the model will still decrease with distance from the electrodes. Nevertheless, with more electrodes, better software, and more single readings this effect can be minimised.

One of the most important results from the tomographic resistivity reconstruction is the monitoring of major resistivity changes with time. Despite of the uncertainties in the quantitative interpretation, general trends in the change of resistivities are monitored well. The resistivity tomograms in Appendix C show some major changes during January 1998. It starts with high resistivities around the borehole electrodes and the inner part of the investigated area. Until end of January the resistivity decreased to moderate values. After that, the resistivity values increased drastically during only a few days to the initial high values. On February 10, they are back at the moderate level and remain nearly constant until the next two months. This development of the resistivity can be explained by some drilling work in other parts of the laboratory. According to the geological and hydraulic conditions at Äspö, the granite contains many highly conductive fracture zones with a high degree of connectivity. A major loss of water through an open borehole in other parts of the mine can cause de saturation effects and pressure drops in the ZEDEX-DEMO-tunnel area. After the outflow is stopped by grouting or sealing the borehole, the hydraulic conditions recover to their initial values.

In summary, the tomographic monitoring of this large area shows the general applicability of such measurements in a granitic environment underground. The numerical uncertainties can be partly dissolved by including more electrodes and single measurements in the inversion algorithm. Nevertheless, a qualitative non-destructive monitoring of the resistivity / water distribution is easily possible.

3.3.4 Backfilled ZEDEX-Tunnel

During 1999 the ZEDEX-tunnel was back filled with different mixtures of clay and crushed rock. Some experiments were installed to monitor the change of petrological properties of the clay with different saturations. In November 1999, the ZEDEX-drift was sealed with a plug. The saturation in the backfill material increased due to natural water inflows from the surrounding rock.

In the deepest part of the ZEDEX-tunnel a tomographic electrode array consisting of three profiles covering three sides of a rectangle were installed to monitor the resistivity distribution in the backfill material. The results obtained are shown in Figure 3.3-5.

The resistivity distribution in the back filled ZEDEX-tunnel shows in general low resistivities on the side walls and a higher resistivity in the centre of the tomogram. This effect is partly caused by a decreasing resolution in this part. But even on the sides where the resolution is constant the resistivity differs between different parts of the walls. In average the right side shows lower resistivity values than the left side. It is obvious that the low resistivity anomalies near the walls are confined to small areas along the electrode profiles. This indicates an inhomogeneous inflow of water into the backfill material and is caused by water-bearing fracture systems in these areas.

Until October 1999, the resistivity distribution remained nearly constant. Before the final sealing of the ZEDEX-tunnel in November 1999, the water from the tunnel was drained, so the saturation of the backfill material could not increase. The resistivity tomogram from November 3, 1999 shows slightly reduced average resistivity values which may be an effect of increasing saturation in the backfill.

From December 14, 1999, filter mats installed in the plug were flooded with salt water. Consequently, a low-resistivity anomaly began to evolve, which can be seen in the lower part of the tomograms of January 11 and January 17, 2000.

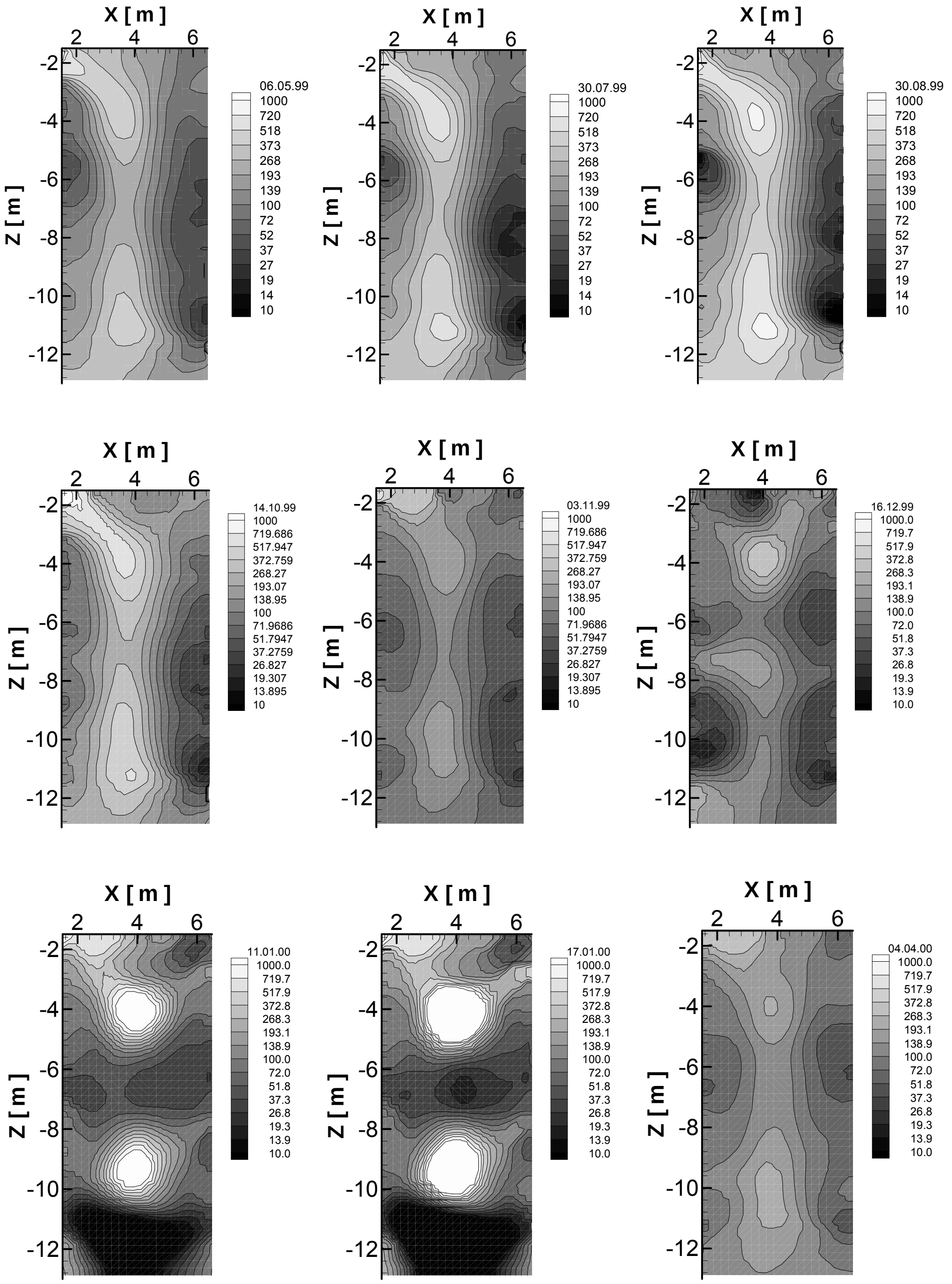

Figure 3.3-5: Resistivity distribution in the back filled ZEDEX-tunnel

As discussed in the previous sections, the thin low-resistivity anomaly at the lower edge of the inversion model leads to high-resistivity "ghosts" in the regions of lower resolution. After the end of this flooding test the anomaly reduced and vanished again. The measurements had to be stopped in April, 2000, when the geoelectric system had to be demobilised and transported back to Braunschweig.

3.4 Summary of geoelectric monitoring at Äspö HRL

The objective of the geoelectric measurements at Äspö was the determination and monitoring of water saturation in the excavation disturbed zone, in the rock between the ZEDEX- and the DEMO-tunnel, and the back filled ZEDEX-tunnel. On laboratory samples a calibration function for the correlation of resistivity and water content in the Äspö granite was determined. This function was applied to the quantitative interpretation of the in-situ measurements.

For the computation of the resistivity distribution from the measured voltage and current values the application of computer-aided inversion algorithms was necessary. From model calculations it was shown that the existence of thin fractures causes numerical anomalies which may mislead in the interpretation of the resistivity distribution. In contrast to this the numerical effect of the topography along the profile is rather negligible.

With the geoelectric measurements along the profiles of the different tunnels it was shown that the excavation disturbed zone usually has an extension of several decimetres in the blasted tunnels. The saturation in the excavation disturbed zone changed due to the grouting of the walls.

The tomographic resistivity image of the whole area between ZEDEX- and DEMO-tunnel was partly distorted from the influence of the thin fracture zones. The applied inversion software (RESITOMO) only allowed a resolution less than the fracture zone. Only an average resistivity distribution was obtained with these measurements, but they clearly show some short time variations which can be related to human activity in the area.

The tomographic resistivity images of the back filled ZEDEX-tunnel showed only minor changes in the observation period, but the results are in reasonable agreement with the test field history.

Generally, it can be stated that - with some limitations - the geoelectric method is applicable in a granitic rock mass to monitor seasonal changes in regional water saturation or distribution, respectively. However, thin water-bearing fractures which cannot be detected because of limited resolution lead to the computation of high resistivity anomalies.

4 Summary

The field tests of the two-phase-flow experiment were performed in the Äspö HRL in the niche 2715 at the 360 m-level from 1997 to 1999. This test site was selected within a pre-investigation programme performed by GRS in 1996.

The basic parameters of the fractured rock were determined by hydro testing and measurements of two-phase-flow parameters, e. g the gas entry pressure. The data from site characterisation were used to set up the models for the simulation of water and gas flow in a single fracture system. The natural gas composition of the formation water and the rock was determined throughout the whole project duration to support the interpretation of the relevance of gas migration. To support interpretation of measured data numerical simulations of single-phase- and two-phase-flow conditions in the test area were performed with the computer programmes ROCKFLOW and MUFTE, respectively. Furthermore, the code MUFTE_UG takes into account advanced numeric and permits explicit modelling of single fractures in porous media. As a separate task, efforts were undertaken to apply the methodology of geoelectric resistivity measurements for monitoring of changes of water and gas saturation of the rock formation on a macroscopic scale.

The fracture system named V2 dominates the flow field in the vicinity of the niche 2715. Hydraulic pressure measurement results and numerical simulations show evidence that the pressure distribution in the test area has become stationary after the excavation of the tunnel and the niche. Simulations also indicate that water flow in the rock matrix is negligible and does not contribute to the water inflow into the niche. But the measured pressure distribution requires the consideration of heterogeneous permeability distribution within the fracture system in the models.

The formation water itself carries considerable amounts of dissolved gas which leads to two-phase-flow conditions when the gas is released after a pressure drop (degassing effect). Gas threshold pressure tests clearly show that the gas entry pressure into the fracture is almost zero, whereas in case of the rock matrix it is obviously higher than 5 MPa. Hence, two-phase-flow is of minor importance in the far field of the fractured rock, but may have a certain importance in the excavation disturbed zone (EDZ) in the vicinity of underground openings.

From modelling the two-phase-flow conditions of a 5-m-dipole test in the V2 – system two major observations should be noted. Firstly, flow at the niche wall should not be significantly influenced by the dipole test. This means that under the model assumptions a full recovery of the injected gas can be expected. Secondly, breakthrough of the injected gas occurs after 250 s in the model, and stationary flow is reached after about 600 s. On basis of these findings the dipole tests were expected to take time on the order of a quarter of an hour.

Comparative calculations with varied input parameters confirmed that even an increase of the capillary pressure by a factor of 15 has no impact on the simulations. The same applies to some extent to the mathematical form of the relative-permeability-saturation relation. Model results with a linear function show essentially the same saturation distribution as the results obtained with the Brooks-Corey function. A dipole test performed with gas only was therefore found to provide not enough information to identify the dependence of the capillary pressure from the saturation conclusively. It has to be mentioned though, that no indications for an appropriate value for the parameter□, α in the Brooks-Corey function was available.

CAB developed a model for two-phase-flow processes in fractured porous media. The fractures have been implemented as one-dimensional lines for the 2D model and as two dimensional planes for the 3D model, respectively. It became evident that due to the choice of primary variables (p_w, S_g and p_g, S_w, T, respectively) and the implementation of fractures as hyper planes the entering of gas from the fracture into the matrix system had to be considered carefully. Therefore, the **P**hase **P**ressure **S**aturation **I**nterface **C**ondition (PPSIC) has been established for the fracture formulation. On this basis, a two phase model and a two-phase, two-component model have been implemented.

Furthermore, first approaches have been presented to get effective parameters which are necessary for a reasonable simulation of two-phase-flow processes in fracture-matrix systems. First, the fracture generator was integrated into MUFTE_UG so that reasonable stochastic or deterministic fracture fields could be included in the simulation process. Second, first steps for a new up-scaling concept for two-phase-flow in a single fracture were made.

The advanced numerical methods on high performance computers which has been established for the simulation of gas-water-flow and transport processes now allows the implementation of geo-statistic data fields in two and three dimensions to identify uncertainties with e.g. Monte Carlo methods.

The objective of the geoelectric measurements at Äspö was the determination and monitoring of water saturation in the excavation disturbed zone, in the rock between the ZEDEX- and the DEMO-tunnel, and the back filled ZEDEX-tunnel. A calibration function for the correlation of resistivity and water content in the Äspö granite was determined on laboratory samples. This function was applied for the quantitative interpretation of the in-situ measurements.

For the computation of the true resistivity distribution from measured apparent resistivity values the inversion software RESITOMO was used. Respective model calculations showed that the existence of thin fractures causes numerical anomalies which may mislead the interpretation of the resistivity distribution. In contrast to this, the numerical effect of the topography along the profile was found to be rather negligible.

With the measurements along the profiles of the different tunnels it was shown that the excavation disturbed zone usually has an extension of several decimetres in the blasted tunnels. The saturation in the excavation disturbed zone changed due to the grouting of the walls.

The tomographic resistivity image of the whole area between ZEDEX- and DEMO-tunnel was partly distorted under the influence of the thin fracture zones. The applied inversion software (RESITOMO) only allowed a resolution less than the fracture zone. Only an average resistivity distribution was obtained from these measurements, but they clearly show some short time variations which can be related to human activity in the area. The tomographic resistivity images of the back filled ZEDEX-tunnel showed only minor changes in the observation period, but the results are in reasonable agreement with the test field history.

Generally, it can be stated that - with some limitations - the geoelectric method is applicable to a granitic rock mass to monitor seasonal changes in regional water saturation or distribution, respectively. However, thin water-bearing fractures which cannot be detected because of limited resolution may lead to the computation of high resistivity anomalies.

References

/BAS 00/ Bastian, P., Chen, Z., Ewing, R.E., Helmig, R., Jakobs, H., and Reichenberger, V.: Numerical Simulation of Multiphase Flow in Fractured Porous Media. Numerical Simulation of Multiphase Flow in Porous Media, Lecture Notes in Physics, Springer Verlag, 2000.

/BAS 96/ Bastian, P., Helmig, R., Huber, R. and Braun, C.: Modelling and efficient solution technique for multiphase flow in porous media. Technical report, SFB 404 Mehrfeldproblem in der Kontinuumsmechanik, 1996.

/BAS 97a/ Bastian, P., Birken, K., Lang, S., Johannsen, K., Neuß, N., Rentz-Reichert, H. and Wieners, C. UG: A flexible software toolbox for solving partial differential equations. Computing and Visualisation in Science, 1:27-40, 1997.

/BAS 97b/ Bastian, P. and Helmig, R: Fully-Coupled Solution Techniques for Two Phase Flow in Porous Media. 1. Multigrid solution and large scale computing, Advances in Water Resources, 1997.

/BOS 98/ Bossart, P., Mazurek and Hermansson, J.: Structural Conceptual Models of Water-Conducting Features at Äspö. In Characterisation and Evaluation of Sites for Deep Geological Disposal of Radioactive Waste in Fractured Rocks. Proc. 3rd Äspö International Seminar, TR-98-10, p. 191- 211, Oskarshamn, 1998.

/FEI 98/ Fein, E.; Graefe, V.; Kull, H.; Helmig, R.; Jakobs, H.: Dependency of Hydraulic Flow Conditions on Rock Saturation around repository Drifts. Proceedings of DisTec 1998. International Conference on Radioactive Waste Disposal, Sep. 9 – 11,1998, Hamburg, 1998.

/FLA 97/ Flach, D.; Jockwer, N.; Komischke, M.; Kull, H.; Rothfuchs, T.: Preliminary Investigations for the Characterisation and Selection of a Test Field for a Two-Phase-Flow Experiment in the Äspö Hard Rock Laboratory.- GRS 145, Köln, 1997.

/GEL 95/ Geller, J.T. & Jarsjö, J.: Groundwater degassing and two-phase flow: Pilot hole test report.- SKB-ICR-95-03, 1995.

/GIL 83/ Gilman, J.A. and Kazemi, H.: Improvements in Simulation of Naturally Fractured Reservoirs. Society of Petroleum Engineers Journal, 8:695 - 707, 1983.

/HEL 00/ Helmig, R., Bastian, P., Jakobs, H., and Reichenberger, V.: Multiphase Multicomponent Processes in Fractured Porous Media. Bericht, Institut für Wasserbau, Universität Stuttgart, Stuttgart, 2000.

/HEL 93/ Helmig, R.: Theorie und Numerik der Mehrphasenströmungen in geklüftet-porösen Medien. Technical report, Institut für Strömungsmechanik und Elektronisches Rechnen im Bauwesen, Universität Hannover, 1993.

/HEL 94/ Helmig, R., Braun, C., and Emmert, M.: MUFTE - A numerical model for simulation of multiphase flow processes in porous and fractured-porous media. Programmdokumentation (HG 208). Technical Report 94/3, Institut für Wasserbau, Universität Stuttgart, 1994.

/HEL 94/ Helmig, R., Braun, C., Emmert, M.: MUFTE - A numerical model for simulation of multiphase flow processes in porous and fractured-porous media. Programmdokumentation (HG 208). Technischer Bericht 94-3, Institut für Wasserbau, Universität Stuttgart, 1994.

/HEL 94/ Helmig, R.; Braun, C.; Emmert, M.: MUFTE – A numerical model for simulation of multiphase flow processes in porous and fractured-porous media. Programmdokumentation (HG 208). Technical Report 94-3. Institut für Wasserbau, Universität Stuttgart, 1994.

/HEL 98/ Helmig, R., Class, H., Huber, R., Sheta, H., Ewing, J., Hinkelmann, R., Jakobs, H., and Bastian, P.: Architecture of the modular program system MUFTE-UG for simulating multiphase flow and transport processes in heterogeneous porous media. Mathematische Geologie, Band 2, 1998.

/HEM 99/ Hemminger, A., Neunhäuserer, L. and Helmig, R.: The Reliability of a Stochastic Fracture Generator. In F. Stauffer, W. Kinzelbach, K. Kovar, and E. Hoehn, editors, IAHS Publication, number 265, Wallingford, Oxfordshire, UK, 1999. IAHS Press.

/JAR 96/ Jarsjö J. and Geller J.T.: Groundwater degassing: Laboratory experiments in rock fracture replicas with radial flow. Skb äspö hrl progress report, Swedish Nuclear Fuel and Waste Management Company, 1996.

/JAR 98/ Jarsjö, J. and Destouni, G.: Hydraulic conductivity relations in soil and fractured rock: Fluid component and phase interaction effects. Skb technical report, Swedish Nuclear Fuel and Waste Management Company, 1998.

/JOC 98/ Jockwer, N.; Kull, H.; Zimmer, U.: Preparatory In-Situ Investigations for a Two-Phase-Flow Experiment in the ÄSPÖ Hard Rock Laboratory.- Proceedings WM 1998 Symposium, March 3rd-6th 1998, Tucson/US.

/KOL 97/ Kolditz, O. (ed): ROCKFLOW – Numerical Modelling of Fluid Flow, Contaminant, and Heat Transport in Subsurface Systems. User's Manual. Version 3.2. Institut für Strömungsmechanik und Elektronisches Rechnen im Bauwesen, Universitnover, 1997.

/LEV 41/ Leverett, M.C.: Capillary Behavior in Porous Solids. Transactions of the AIME, 142:152 - 169, 1941.

/MAR 86/ Marsily, de G.: Quantitative Hydrogeology. Academic, Berkeley, Cal., 1986.

/MAR 99/ Marschall, P., Fein, E., Kull, H., Lanyon, B., Liedtke, L., Müller-Lyda, I., Shao, H.: Grimsel Test Site Investigation Phase V (1997-2002). Conclusions of the Tunnel Near-Field Programme (CTN).- Nagra Technical Report 99-07, Wettingen/Switzerland.

/PER 91/ Persoff, P., Pruess, K., and Myer, L.: Two-Phase Flow Visualisation and Relative Permeability Measurement in Transparent Replicas of Rough-Walled Rock Fractures. Technical report, University of California, 1991.

/PRU 90/ Pruess, K. and Tsang, Y.W.: On Two-Phase Relative Permeabilitiy Capillary Pressure of Rough-Walled Rock Fractures. Water Resources Research, 10, 1990.

/PRU 90/ Pruess, K., Cox, B.L. and Persoff, P.: A Casting and Imaging Technique for Determining Void Geometry and Relative Permeability Behavior of a Single Fracture Specimen. Lawrence Berkeley Laboratoy, 1990.

/RHE 97a/ Rhén I., Gustafsson, G., Wikberg, P. (1997a): Äspö HRL – Geosientific evaluation 1997/4. Results from pre-investigations and detailed site characterisation. Comparison of predictions and observations. Geohydrology, Groundwater chemistry and Transport of solutes. SKB TR 96-05, Stockholm.

/RHE 97b/ Rhen, I., Gustafson, G., Stanfors, R., Wikberg, P.: Äspö HRL - Geoscientific evaluation 1997/5. Models based on site characterisation 1986-1995. SKB Technical Report 97-06, Swedish Nuclear Fuel and Waste Management, Stockholm, 1997.

/RHE 98/ Rhén I., Gustafsson, G., Stanfors, R., Wikberg, P.: Model 96 of the Äspö Site. Results of prediction and outcome based on surface and underground borehole investigations.- Characterisation and evaluation of sites for deep radioactive waste in fractured rock. Proceedings from 3rd Äspö International Seminar, June 10-12, 1998, p. 35-44, SKB TR-98-10, Stockholm, 1998.

/ROC 88/ ROCKFLOW 1988 - 1994: Theorie und Benutzeranleitung zum Programmsystem ROCKFLOW. Teil 1: J. Wollrath / R. Helmig: SM2 - Strömungsmodul für inkompressible Fluide.

/ROM 66/ Romm, E.S.: Fluid Flow in Fractured Rocks. Moscow (translated by W. R. Blake, Bartlesville, OK), 1966.

/SEL 00/ Sellen, U.: Mineralogische und petrographische Untersuchungen an Kluftsystemen im schwedischen Untertagelabor Äspö.- Diplomarbeit, TU-Clausthal, Inst. für Mineralogie u. Mineralische Rohstoffe, 2000.

/THI 06/ Thiem, G.: Hydrogeologische Methoden.- Leipzig, 1906.

/WEL 97/ Weltest 200, 97A: User Guide Schlumberger, Geoquest, 1997.

/WIT 80/ Witherspoon, P.A., Wang, J.S.Y., Iwai, K., Gale, J.E.: Validity of Cubic Law for Fluid Flow in a Deformable Rock Fracture.- Water Resource Research, vol. 16, no6, p.1016-1024, 1980.

List of Figures

List of Tables

Appendix

Appendix A: ZEDEX-Tunnel

ZEDEX 06.11.97

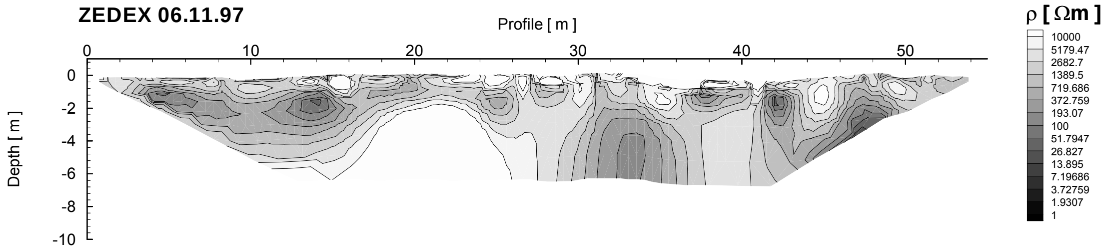

ZEDEX 17.12.97

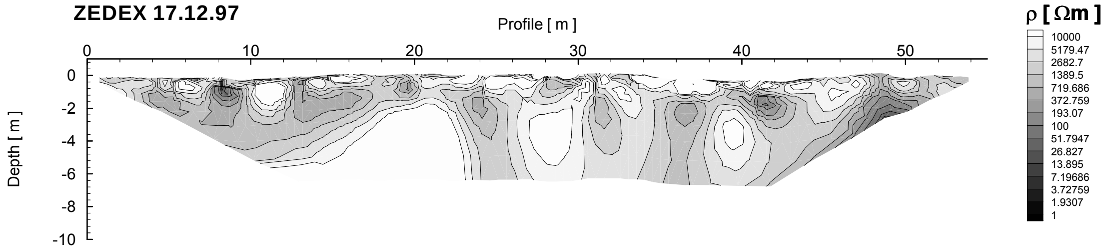

ZEDEX 03.01.98

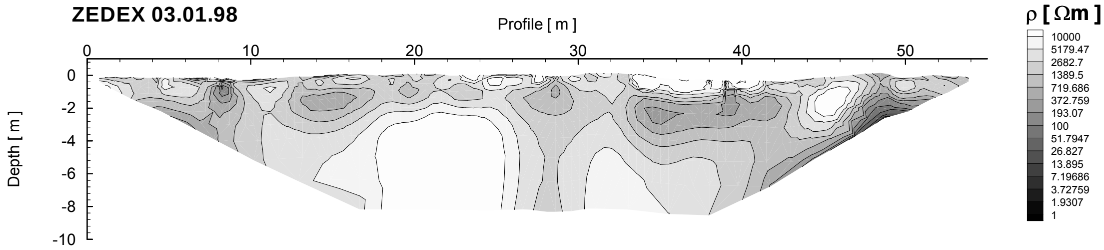

ZEDEX 02.02.98

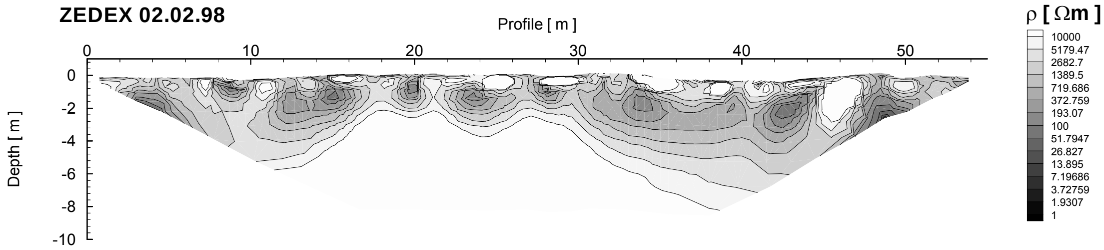

ZEDEX 02.03.98

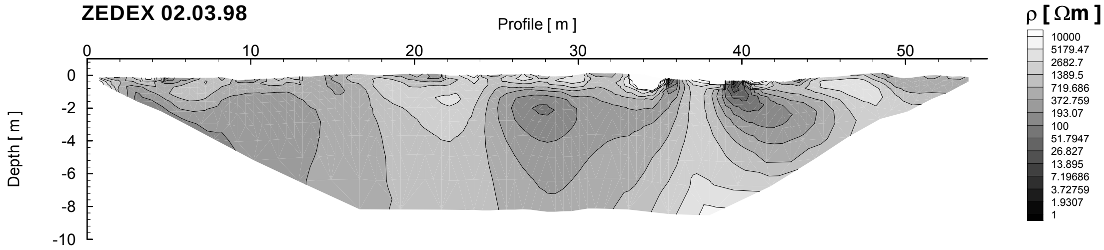

Appendix B: DEMO-Tunnel

DEMO 12.11.97

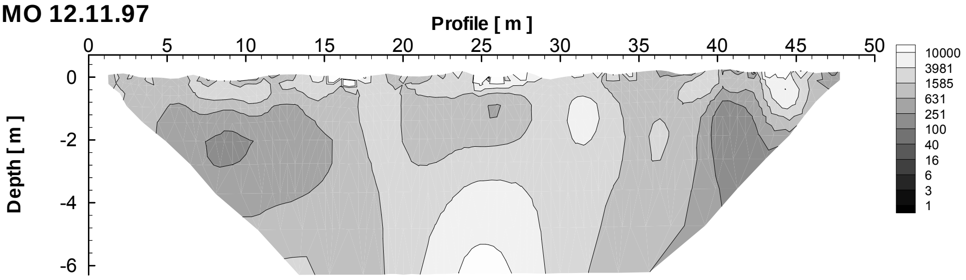

DEMO 13.01.98

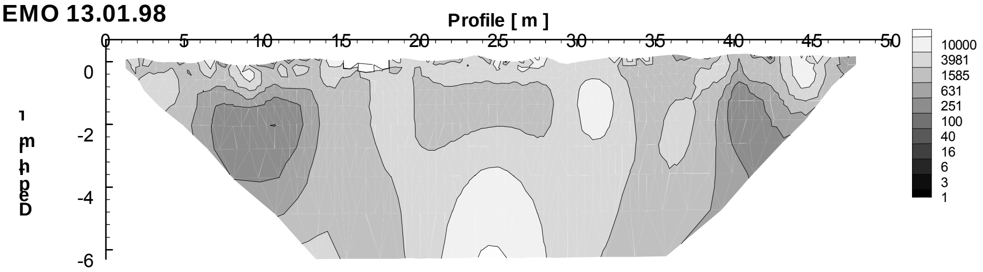

DEMO 01.04.98

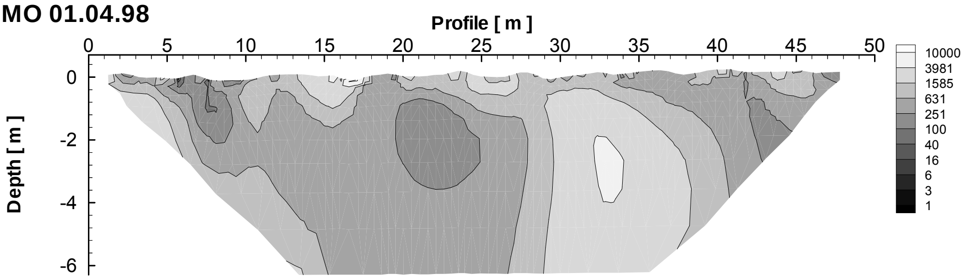

DEMO 04.05.98

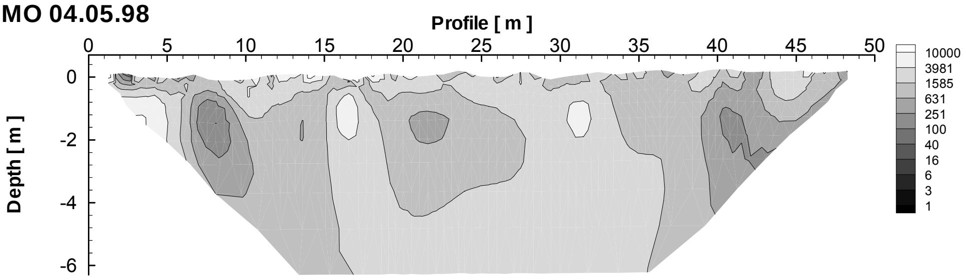

DEMO 10.06.98

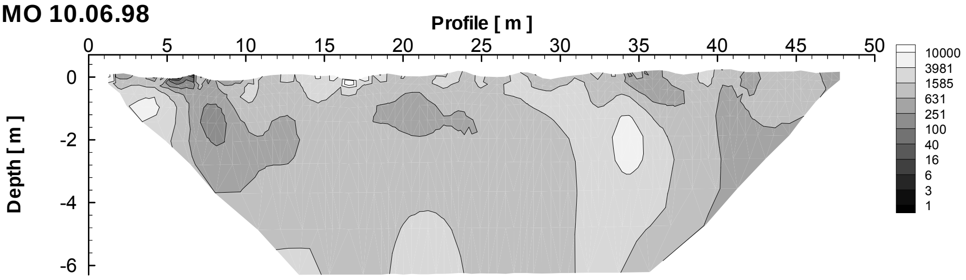

DEMO 01.07.98

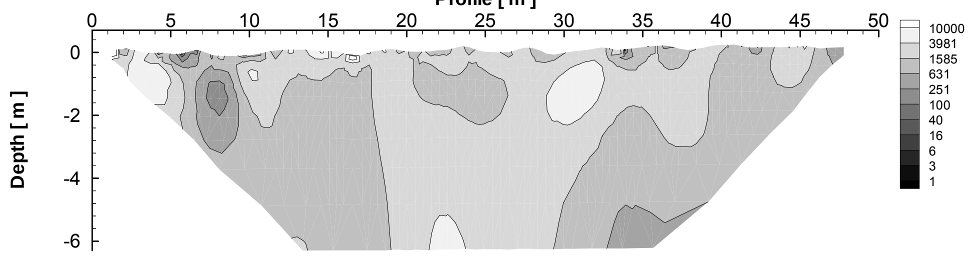

DEMO 06.08.98

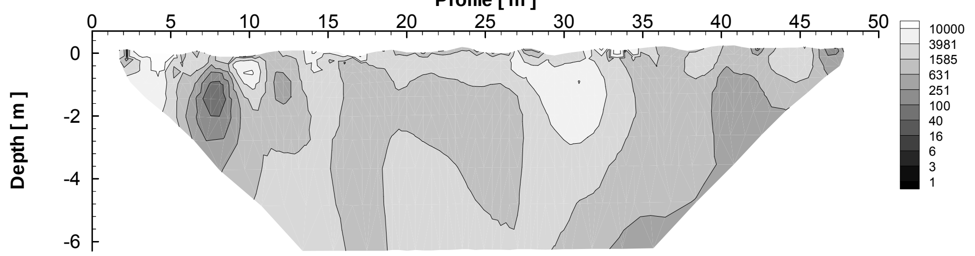

DEMO 10.09.98

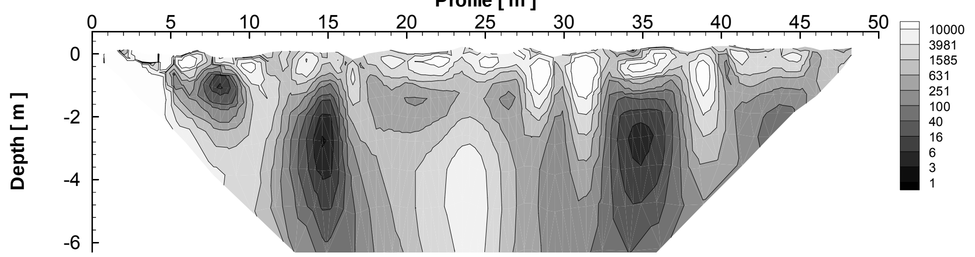

DEMO 28.10.98

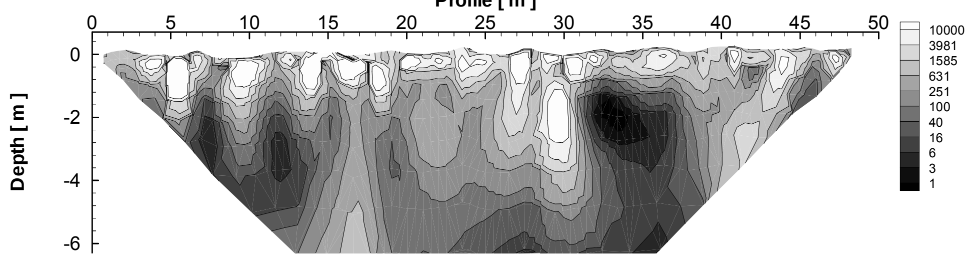

DEMO 02.11.98

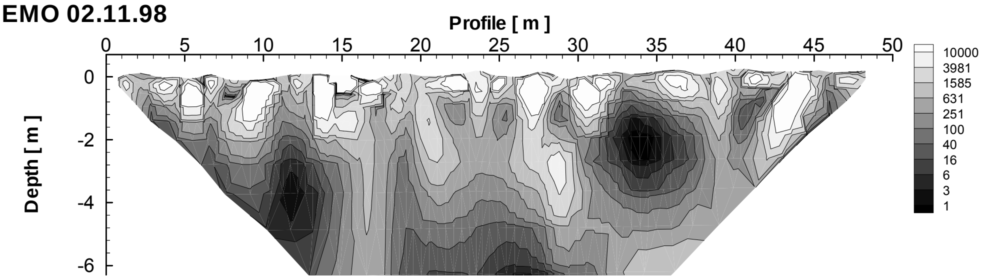

DEMO 08.12.98

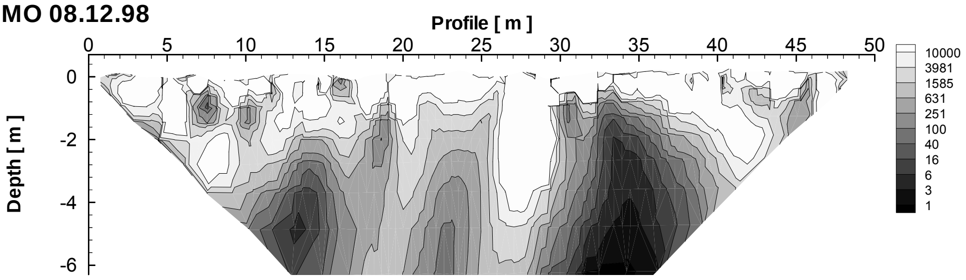

DEMO 01.01.99

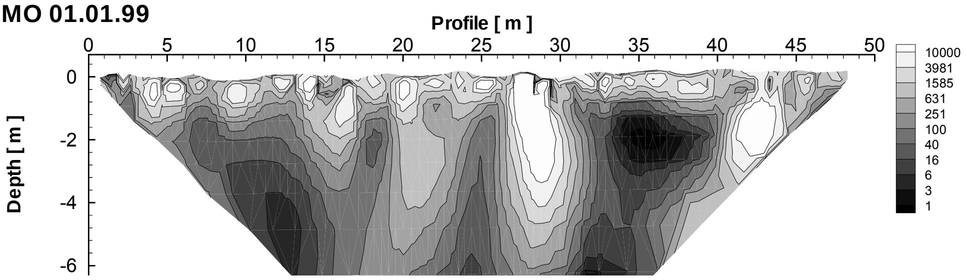

DEMO 05.02.99

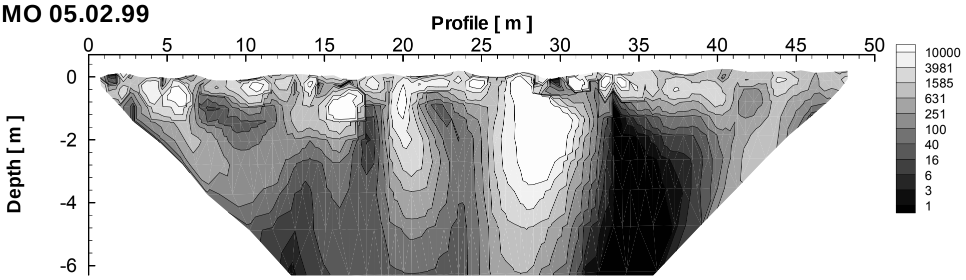

DEMO 03.03.99

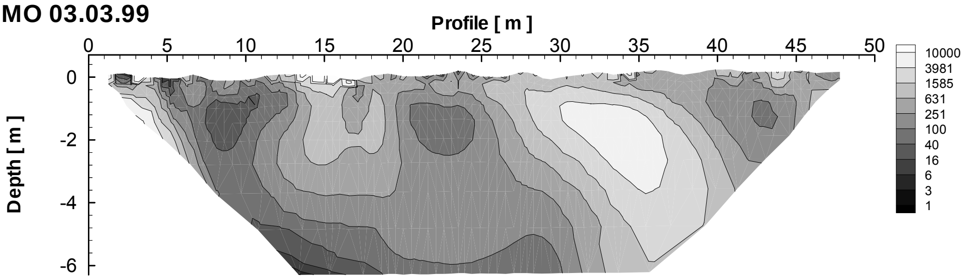

DEMO 27.04.99

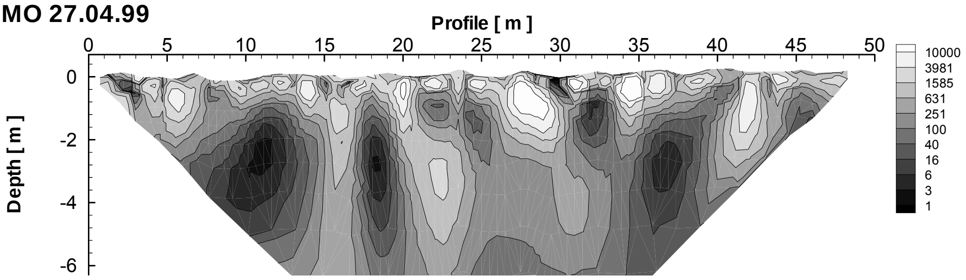

DEMO 05.05.99

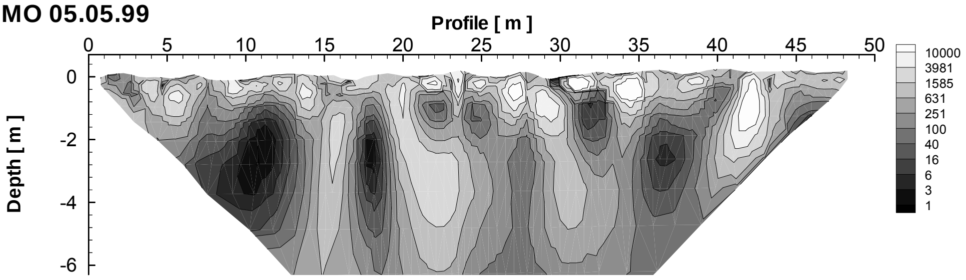

DEMO 05.06.99

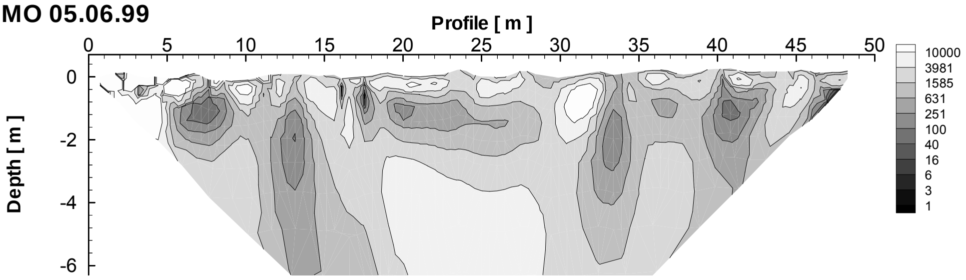

DEMO 02.08.99

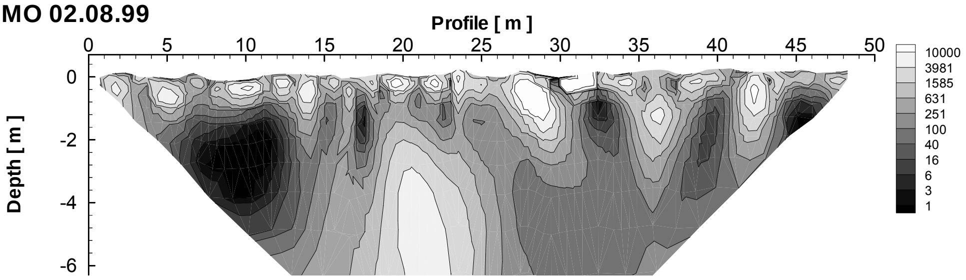

DEMO 26.08.99

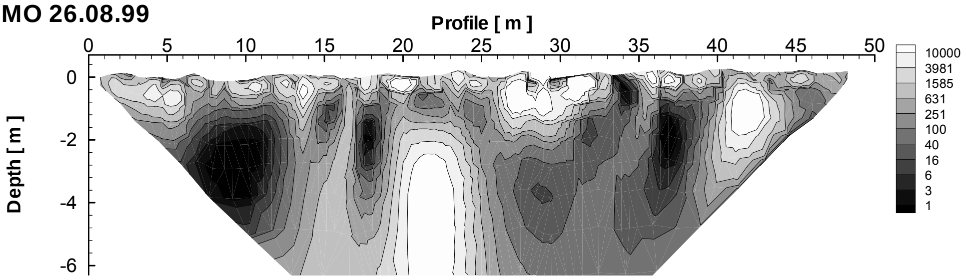

DEMO 12.10.99

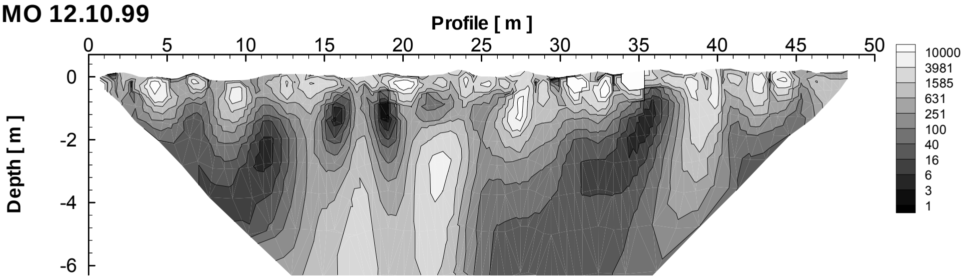

Appendix C: Tomographic Inversions

Dark grey: low resistivities; Light grey: high resistivities

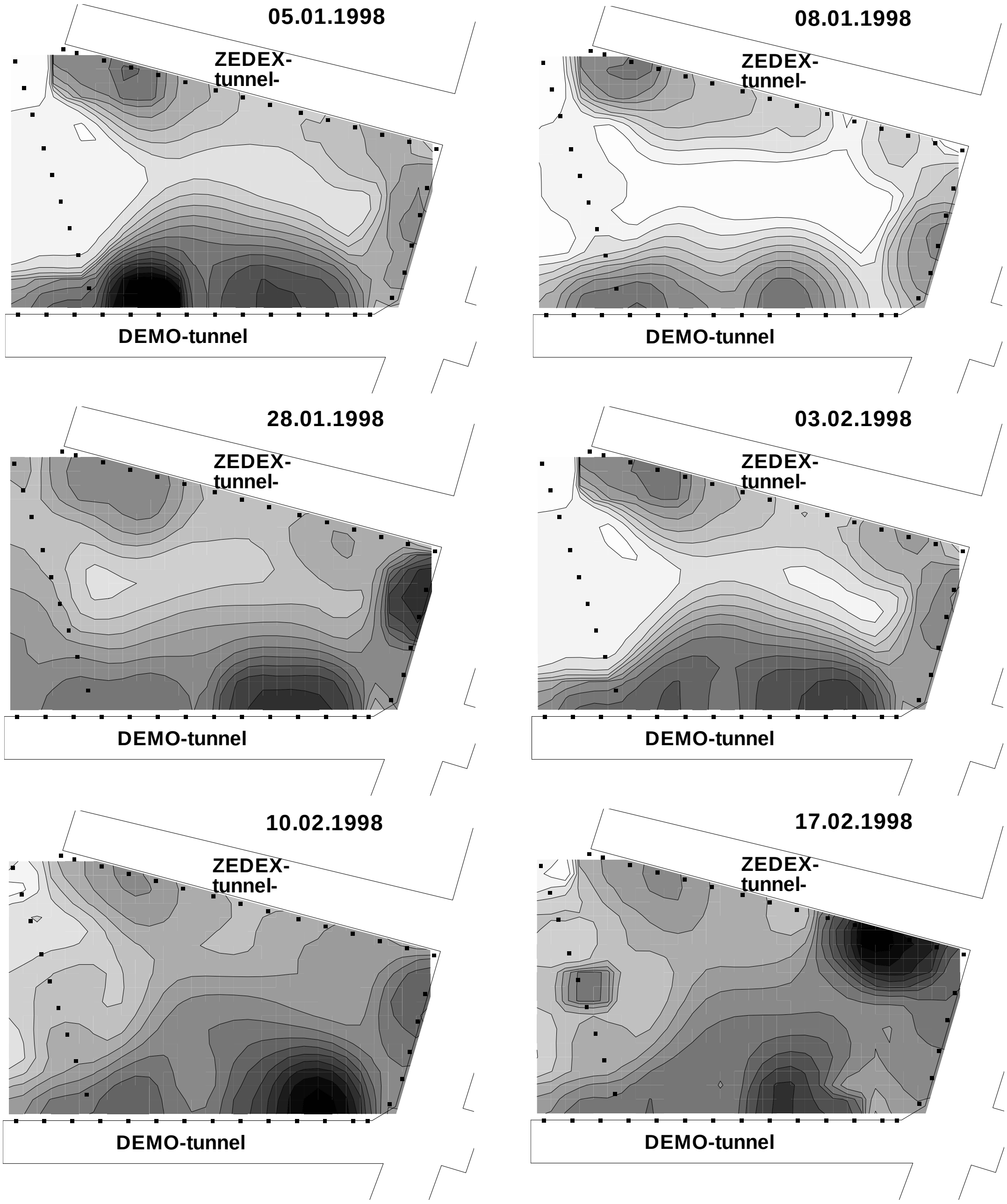

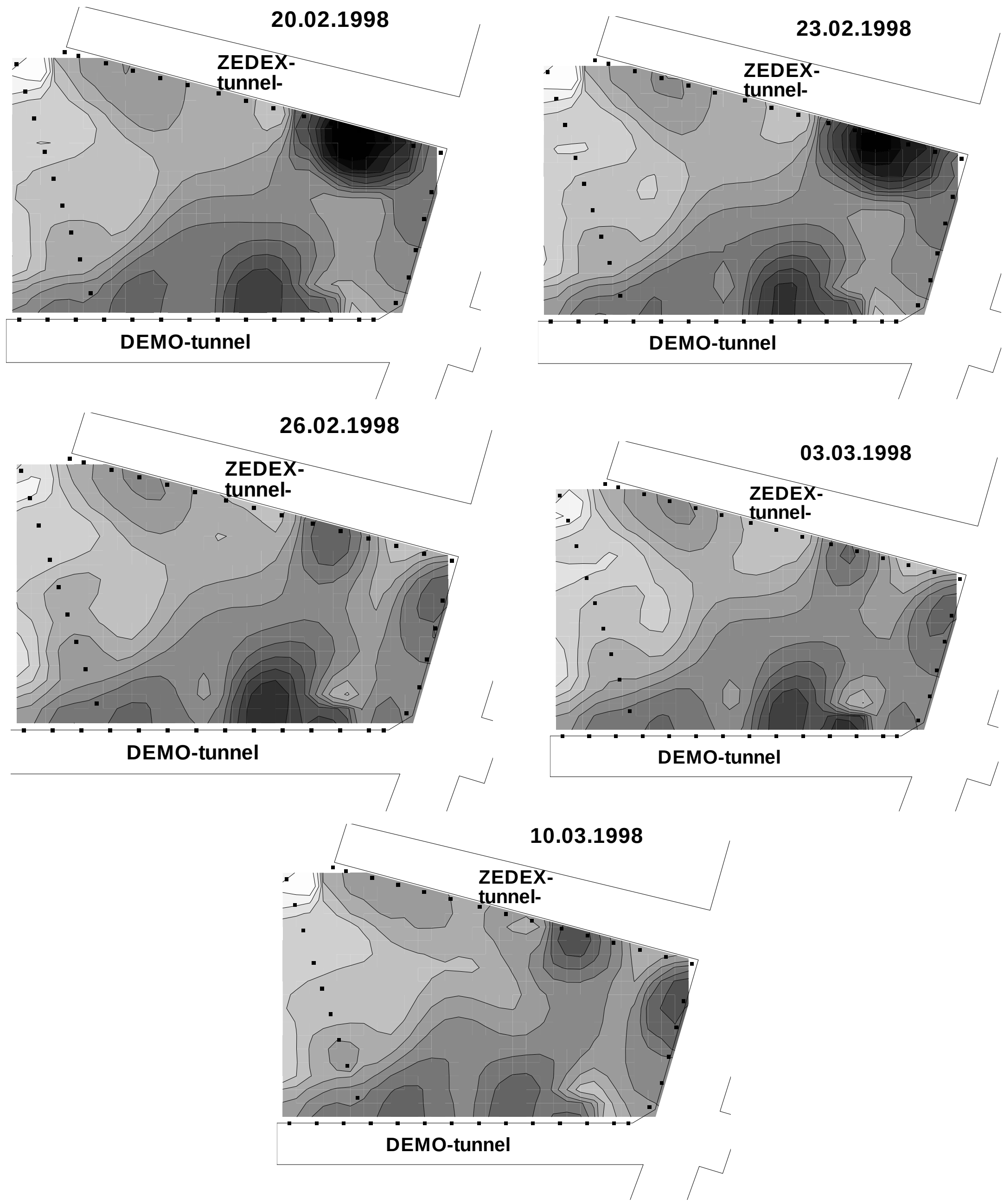
20.02.1998
ZEDEX-
tunnel-
DEMO-tunnel
23.02.1998
ZEDEX-
tunnel-
DEMO-tunnel
26.02.1998
ZEDEX-
tunnel-
DEMO-tunnel
03.03.1998
ZEDEX-
tunnel-
DEMO-tunnel
10.03.1998
ZEDEX-
tunnel-
DEMO-tunnel

Appendix D: Backfilled ZEDEX-Tunnel

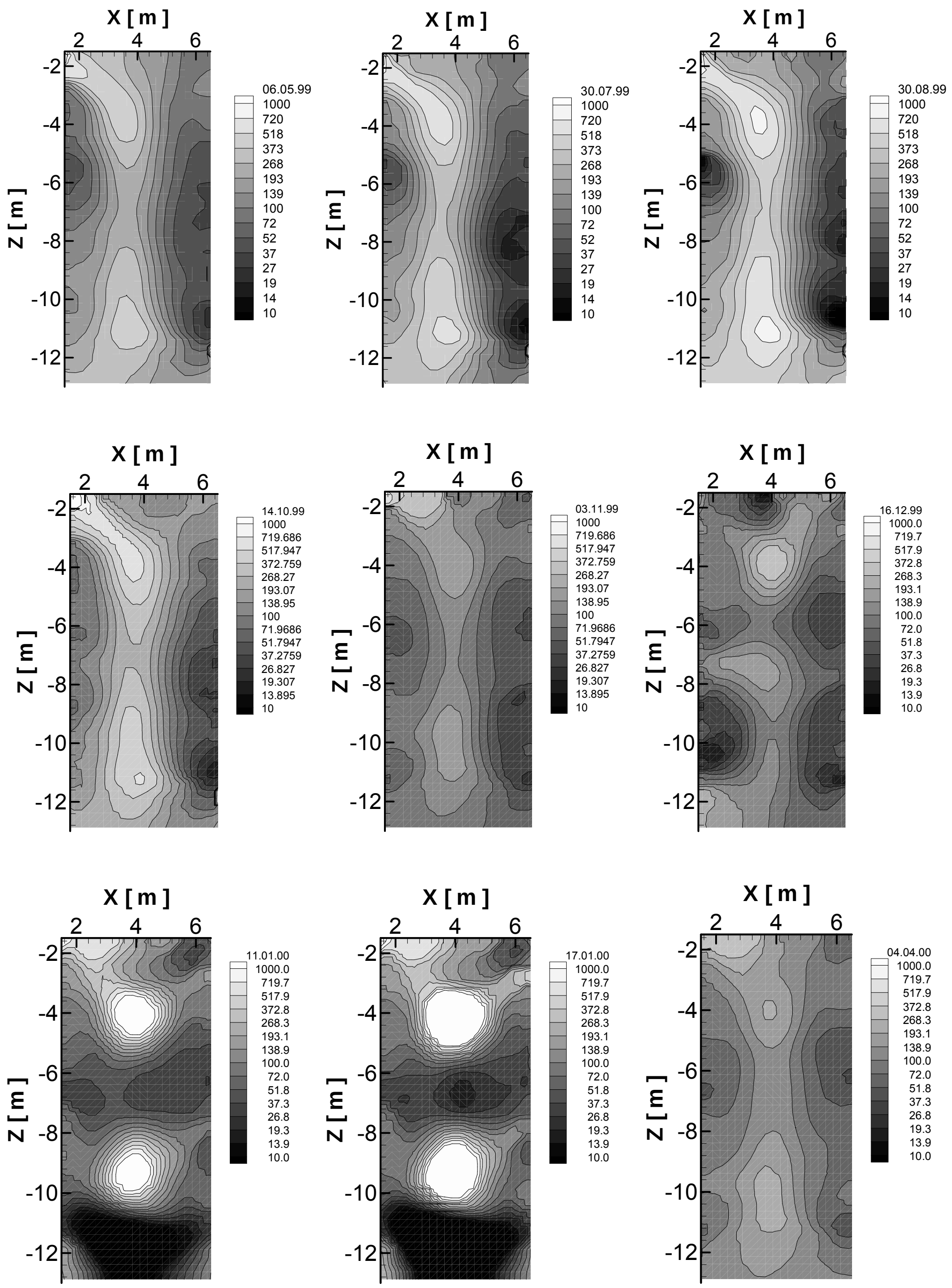

Gesellschaft für Anlagen- und Reaktorsicherheit (GRS) mbH

Schwertnergasse 1
50667 Köln
Telefon +49 221 2068-0
Telefax +49 221 2068-888

Forschungsinstitute
85748 Garching b. München
Telefon +49 89 32004-0
Telefax +49 89 32004-300

Kurfürstendamm 200
10719 Berlin
Telefon +49 30 88589-0
Telefax +49 30 88589-111

Theodor-Heuss-Straße 4
38122 Braunschweig
Telefon +49 531 8012-0
Telefax +49 531 8012-200

www.grs.de

ISBN 3-931995-51-8